Shell Model Study on Mixed-Symmetry States in N=30 Isotones

（N=30同中性子核における混合対称状態の殻模型による研究）

中田　仁

Shell Model Study on Mixed-Symmetry States in $N = 30$ Isotones

March 8, 1991

Hitoshi Nakada

Ph. D. Thesis
(University of Tokyo)

Address: Physics Laboratory, School of Medicine, Juntendo University
Hiraga-gakuendai 1-1, Inba-mura, Inba-gun, Chiba 270-16, Japan

Acknowledgement

I wish to express my gratitude to Prof. A. Arima for guiding me to the world of the nuclear physics. I express my special thanks to Prof. T. Otsuka for suggesting this subject and for enlightening discussion during performing this work. I also acknowledge the goodwill of Prof. T. Sebe, because he allowed me to use and refer the shell model computer code which he has developed, as well as because he gave me some pieces of precious advice in creating some computer programs.

I am grateful to Dr. H. Sagawa especially for useful discussion in the calculation of the form factors, and to Dr. K. Ogawa for his guidance of the current status of the shell model calculation in the pf-shell. I thank Drs. M. Fujiwara and J. Takamatsu for informing of the $(\vec{p}, p')$ results.

I am thankful to Prof. K. Yazaki and other members of Nuclear Theory Group, University of Tokyo, as well as to all the members of Physics Laboratory, Juntendo University, for their continuous encouragement.

For the numerical calculation, I used HITAC-S820/80 in Computer Center, University of Tokyo, and HITAC-S820/80 in Kanagawa Factory, Hitachi Corporation. This work is financially supported by Research Center of Nuclear Physics, Osaka University, in part.

Contents

1 Introduction

Atomic nuclei are systems consisting of many strongly interacting nucleons. Though the interaction between nucleons is originated from mesons, most of low energy phenomena has been described only by the degrees of freedom of nucleons. In fact, the shell model has succeeded in describing low-lying states in light-mass nuclei by a small number of valence nucleons around a doubly-magic inert core. On the other hand, as the number of nucleons increases, it becomes prohibitively difficult to apply the shell model directly, since the number of states is enormous. In those nuclei, however, a characteristic order grows up, which arises from the collective motion of a large number of nucleons. Especially the quadrupole collective character is seen in low-lying energy spectra in most of medium- and heavy-mass nuclei.

Bohr and Mottelson formulated the nuclear quadrupole collective motion[1], based on the liquid-drop picture. They assumed an equilibrium shape of a nucleus, and described a rotational band appearing in deformed nuclei. They also discussed elementary excitations around the equilibrium shapes as phonons. The vibrational spectra of spherical nuclei, as well as the β- and γ-bands of nuclei with axially-symmetric deformation, are described in terms of the phonons. The interacting boson model (IBM) has also been successful in describing the quadrupole collective motion of medium-heavy and heavy nuclei[2]. It is stimulating that the IBM can describe transitional nuclei[3], as well as spherical and well-deformed nuclei[4]. The nuclear quadrupole collective modes, however, should be composed of nucleons. There have been many attempts to give a foundation to the boson descriptions from nucleonic degrees of freedom. In the justification of the IBM, the bosons basically

correspond to like-nucleon pairs with the same spin-parity.

In early researches on the nuclear collective motion, the coherence with respect to protons and neutrons has been assumed. Also in the IBM, the original version[4] does not distinguish the proton and neutron degrees of freedom. On the other hand, in the process of justifying the IBM, the proton-neutron IBM, which is often called IBM-2 for the abbreviation, was proposed[5]. The original version of the IBM, which is sometimes called IBM-1, is obtained as the totally symmetric subspace of the IBM-2. In the IBM-2 description, lowest collective states are symmetric with respect to proton and neutron bosons, consistently with the success of the IBM-1. On the other hand, because of the distinction of proton bosons and neutron bosons, the IBM-2 has mixed-symmetry states with respect to the proton and neutron degrees of freedom.

The mixed-symmetry states have been predicted in higher energy region since the IBM-2 was proposed[6]. The most familiar example is the scissors mode in a deformed nucleus. In the geometrical picture, the ground-state band is generated from an intrinsic wavefunction which has a quadrupole deformation coherent between protons and neutrons. The $K = 0$ quantum number is assigned to this band, corresponding to the axial symmetry of the intrinsic wavefunction. In the scissors mode, the proton part of the intrinsic wavefunction oscillates relative to the neutron part, with $K = 1$. The scissors 1^+ state was predicted within the IBM-2[7, 8] as well as other models[9], and was discovered later[10, 11].

In a vibrational nucleus, the ground state has a spherical shape. In the IBM description, this state consists only of so-called s-bosons. The lowest 2^+ state is considered the quadrupole surface oscillation mode in phase between

protons and neutrons. The quadrupole surface oscillation is described by a d-boson around some s-bosons in the IBM. Both of the two states are totally symmetric in the IBM-2, since the proton wavefunction always maintains the coherence with the neutron one. On the other hand, there could be a 2^+ state in which protons oscillates out of phase with neutrons. This state is described as a mixed-symmetry state in the IBM-2, since the wavefunction is antisymmetric in the d-boson part. It is noted that this 2^+ state is naturally expected to be the lowest mixed-symmetry state in a vibrational nucleus.

The mixed-symmetry 2^+ state has been predicted since the IBM-2 was proposed, and has been discussed for several nuclei[12, 13]. The excitation energy of the state is conjectured to be 2$\sim$4MeV, although there remains some ambiguity in the phenomenological estimates. There has also been several researches on this mode based on other models. In earlier geometrical approaches this mode was predicted with very high energy ($\sim$15MeV)[14], and hence did not attract experimental interest. Recently Faessler and Nojarov modified the evaluation[15], by taking into account the density dependence on the symmetry energy. They showed that the out-of-phase oscillation mode is expected in relatively low energy region, consistently with the IBM-2. Similar expectation is acquired by a particle-core coupling model[16].

Some candidates of the mixed-symmetry 2^+ states are reported recently, in mass regions of $50 < A < 60$[17, 18, 19], $A \sim 110$[20] and $A \sim 140$[21], based on such probes as $M1$ transition rates and proton scattering cross sections. The mixed-symmetry 2^+ states, however, have not been confirmed so far. Probably high level density in the relevant energy region makes it difficult to observe the mixed-symmetry 2^+ state. Even in lighter nuclei there can exist some states without any counterparts in the IBM space, in

the energy region of the mixed-symmetry states. Moreover, we do not know properties of the mixed-symmetry 2^+ states fully well. Thus some careful theoretical studies from a microscopic standpoint are required.

The recent development of computers enables us to execute shell model calculations in a sufficiently large configuration space of the pf-shell. We apply, in this work, the shell model with an effective interaction derived from a nucleon-nucleon interaction to the nuclei in $50 < A < 60$ region, and investigate the mixed-symmetry problem in the $N = 30$ isotones. Nuclei in this mass region provide us with a meeting point of the shell model calculation and the quadrupole collectivity. Low-lying states of ^{56}Fe, for instance, manifest the quadrupole collectivity, while the collectivity seems not to evolve sufficiently in $A < 40$ nuclei. On the other hand, shell model calculations are not applicable in heavier nuclei without any drastic truncation of the model space. Thus the nuclei in this region give a precious testing ground to understand the mixed-symmetry states. We mainly discuss the mixed-symmetry 2^+ states in this paper. The nuclei in this region, however, do not seem entirely spherical. Hence the mixed-symmetry 1^+ state might appear in rather low energy region. We also search for this kind of states.

The mixed-symmetry states absorb a large fraction of the isovector transition probabilities from the lowest-lying states as the 0_1^+ and 2_1^+ states. Zamick and his collaborators have discussed the mixed-symmetry 1^+ state in $40 < A < 50$ region, by using the shell model results[22, 23]. Their discussion is based on $M1$ transition strengths from the ground state, since quadrupole collective degrees of freedom contribute to the isovector $M1$ transition. When active orbits for protons are different from those for neutrons, the mixed-symmetry states have the same isospin as the symmetric states.

Hence the states which has large isovector transition rates to the lowest-lying states as well as has the same isospin as those states are candidates of the mixed-symmetry states We, however, investigate the mixed-symmetry states more carefully, keeping correspondence to the IBM in mind. We first discuss the ^{56}Fe nucleus in detail, and also investigate ^{54}Cr and ^{52}Ti by applying the knowledge obtained in ^{56}Fe.

The definition of the mixed-symmetry states is presented, and some properties of those states are discussed within the framework of the IBM-2, in Section 2. Some experimental reports of the mixed-symmetry 2^+ states so far are summarized in Section 3. In Section 4, the shell model calculation employed in this study is explained. The calculated energy levels, electromagnetic properties, (e, e') form factors and $(\vec{p}, p')$ differential cross sections are compared with the experimental data. The mixed-symmetry states in ^{56}Fe are searched in Section 5, by inspecting the shell model wavefunctions. In Section 6, we shall propose renormalization methods of incorporating some effects of the states outside the truncated space, and apply them to ^{56}Fe in order to realize the correspondence between the IBM picture and the shell model results. The mixed-symmetry states in ^{54}Cr and ^{52}Ti are looked for in Section 7. Some general features of the mixed-symmetry states are also discussed in Section 7. This thesis is summarized in Section 8.

2 Mixed-Symmetry States in the IBM-2

2.1 Proton-Neutron Symmetry in the IBM

The IBM-1 is constructed by the building blocks of s- and d-bosons, which carry $J^P = 0^+$ and $J^P = 2^+$, respectively. The creation and annihilation operators of those bosons satisfy the commutation relations,

$$[s, s^\dagger] = 1, \quad [d_m, d^\dagger_{m'}] = \delta_{m,m'},$$
$$[s, d^\dagger_{m'}] = [s, s] = [d_m, d_{m'}] = 0. \tag{2.1}$$

From the group theoretical point of view, the IBM-1 states constitute totally symmetric subspace in the representation space of the group $U(6)$. Note that the boson number conservation is demanded in the model. The rotational invariance is also assumed. It is known that the IBM-1 has the following three group theoretical limit;

$$U(6) \supset U(5), \quad U(6) \supset SU(3), \quad U(6) \supset O(6). \tag{2.2}$$

From the geometrical point of view, the $U(5)$-limit describes the spherical nucleus, the $SU(3)$-limit does the well-deformed nucleus with the axial symmetry, and the $O(6)$-limit does the γ-unstable nucleus.

The IBM-2 consists of s_π-, d_π-, s_ν- and d_ν-bosons. As in the IBM-1, the s_ρ-bosons $(\rho = \pi, \nu)$ bear $J^P = 0^+$, while the d_ρ-bosons $J^P = 2^+$. The commutation relations among these boson are the usual ones,

$$[s_\rho, s^\dagger_{\rho'}] = \delta_{\rho,\rho'}, \quad [d_{\rho,m}, d^\dagger_{\rho',m'}] = \delta_{\rho,\rho'}\delta_{m,m'},$$
$$[s_\rho, d^\dagger_{\rho',m'}] = [s_\rho, s_{\rho'}] = [d_{\rho,m}, d_{\rho',m'}] = 0. \tag{2.3}$$

These bosons correspond basically to collective like-nucleon pairs with the

same spin-parity. Hereafter the pairs corresponding to the s_ρ- and d_ρ-bosons are denoted by S_ρ and D_ρ, respectively.

These bosons constitutes totally symmetric subspace of the group $U(12)$, since the total boson number conservation is assumed in the model. Actually we further demand the proton and neutron boson number conservation separately, corresponding to the proton and neutron number conservation in the original nucleon system. In this sense, the boson space to be considered is represented by the direct product of the subgroup $U(6)$ of proton bosons and that of neutron bosons,

$$U(12) \supset U(6)_\pi \otimes U(6)_\nu. \tag{2.4}$$

Note that the rotational invariance is assumed in the whole system.

It is convenient, however, to consider another subgroup structure when we handle the proton-neutron symmetry. For this purpose, we have the subgroup

$$U(12) \supset U(6)_{\pi+\nu} \otimes SU(2)_F, \tag{2.5}$$

where the $SU(2)_F$ group is realized by the F-spin, similar to the isospin of nucleons. Then IBM-1 space is composed of the totally symmetric states with respect to the $U(6)_{\pi+\nu}$ sector (hence also to the $SU(2)_F$ sector). Corresponding to Eq.(2.2), we have the group chains as

$$\begin{aligned} U(6)_{\pi+\nu} \otimes SU(2)_F &\supset U(5)_{\pi+\nu} \otimes SU(2)_F, \\ U(6)_{\pi+\nu} \otimes SU(2)_F &\supset SU(3)_{\pi+\nu} \otimes SU(2)_F, \\ U(6)_{\pi+\nu} \otimes SU(2)_F &\supset O(6)_{\pi+\nu} \otimes SU(2)_F, \end{aligned} \tag{2.6}$$

by decomposing the $U(6)_{\pi+\nu}$ sector.

The $U(6)_{\pi+\nu}$ group is constituted by the following 36 generators,

$$\begin{aligned} &[(s_\pi^\dagger + s_\nu^\dagger)(s_\pi + s_\nu)]^{(0)}, \quad [(d_\pi^\dagger + d_\nu^\dagger)(s_\pi + s_\nu)]^{(2)}, \quad [(s_\pi^\dagger + s_\nu^\dagger)(\tilde{d}_\pi + \tilde{d}_\nu)]^{(2)}, \\ &[(d_\pi^\dagger + d_\nu^\dagger)(\tilde{d}_\pi + \tilde{d}_\nu)]^{(J)}, \quad (J = 0, 1, 2, 3, 4) \end{aligned} \tag{2.7}$$

where the modified annihilation operator of d-boson is defined as $\tilde{d}_{\rho,m} = (-)^m d_{\rho,-m}$. These generators resemble those of the IBM-1, as is realized by the correspondence of $(s_\pi^\dagger + s_\nu^\dagger)$ to $s^\dagger$, that of $(d_\pi^\dagger + d_\nu^\dagger)$ to $d^\dagger$, and so on, although the IBM-2 states are not required to belong to the totally symmetric representations of the $U(6)_{\pi+\nu}$ group.

The generators of the F-spin group are

$$\begin{aligned} &\hat{F}_+ = s_\pi^\dagger s_\nu + d_\pi^\dagger \cdot \tilde{d}_\nu, \quad \hat{F}_- = (\hat{F}_+)^\dagger, \\ &\hat{F}_0 = \frac{1}{2}(\hat{N}_\pi - \hat{N}_\nu), \end{aligned} \tag{2.8}$$

where $\hat{N}_\pi$ ($\hat{N}_\nu$) denotes proton (neutron) boson number operator. The labels of the F-spin group are F and F_0, obtained from the eigenvalues of the operators $\hat{F}^2$ and $\hat{F}_0$, where

$$\hat{F}^2 = \frac{1}{2}(\hat{F}_+\hat{F}_- + \hat{F}_-\hat{F}_+) + \hat{F}_0^2. \tag{2.9}$$

The F_0 is a fixed number for each nucleus, whose value is given as

$$F_0 = \frac{1}{2}(N_\pi - N_\nu), \tag{2.10}$$

where N_π (N_ν) expresses the eigenvalue of $\hat{N}_\pi$ ($\hat{N}_\nu$). The label F, defined so as for the eigenvalue of $\hat{F}^2$ to be $F(F+1)$, can take the following values in a single nucleus,

$$F = F_{max},\ F_{max} - 1,\ \cdots,\ |F_0|. \tag{2.11}$$

The F_{max} is defined as

$$F_{max} = \frac{1}{2}(N_\pi + N_\nu) = \frac{1}{2}N_B, \tag{2.12}$$

where N_B denotes the total boson number. The totally symmetric states, namely the IBM-1 states, have $F = F_{max}$. The success of the IBM-1 in the description of lowest-lying states suggests that the F-spin is an approximately good quantum number and that states with larger F are energetically favored in general.

In the IBM-2, we have extra states with $F < F_{max}$. Among them $F = F_{max} - 1$ states are expected to be lowest. The $F = F_{max} - 1$ states are partially anti-symmetric with respect to the proton and neutron degrees of freedom, and called mixed-symmetry states. The scissors mode in deformed nuclei is a typical example, as already mentioned in Section 1. This mode is the lowest mixed-symmetry mode in the vicinity of the $SU(3)$-limit.

The d-boson number N_d becomes a good quantum number in the $U(5)$-limit, which describes the quadrupole vibrational motion of spherical nuclei. The ground state in the $U(5)$-limit should be

$$|0_S^+(s^{N_B})\rangle = |s_\pi^{N_\pi} s_\nu^{N_\nu}\rangle, \tag{2.13}$$

which is trivially totally symmetric, because

$$|0_S^+(s^{N_B})\rangle \propto (F_-)^{N_\nu}|s_\pi^{N_B}\rangle. \tag{2.14}$$

We have two $N_d = 1$ states,

$$|s_\pi^{N_\pi - 1} d_\pi s_\nu^{N_\nu}\rangle, \quad |s_\pi^{N_\pi} s_\nu^{N_\nu - 1} d_\nu\rangle. \tag{2.15}$$

Though these states are not eigenstates of $\hat{F}^2$, we obtain states with good F-spin by linear combinations of the above states as

$$|2_S^+(s^{N_B-1}d)\rangle = \frac{1}{\sqrt{N_B}}(\sqrt{N_\pi}|s_\pi^{N_\pi-1}d_\pi s_\nu^{N_\nu})\rangle + \sqrt{N_\nu}|s_\pi^{N_\pi} s_\nu^{N_\nu-1} d_\nu\rangle, \tag{2.16}$$

$$|2_M^+(s^{N_B-1}d)\rangle = \frac{1}{\sqrt{N_B}}(\sqrt{N_\nu}|s_\pi^{N_\pi-1}d_\pi s_\nu^{N_\nu}) - \sqrt{N_\pi}|s_\pi^{N_\pi} s_\nu^{N_\nu-1} d_\nu\rangle). \tag{2.17}$$

The former state has $F = F_{max}$, as represented by the subscript S, while the latter has $F = F_{max} - 1$, as represented by the subscript M. If the F-spin is conserved, the former is the 2_1^+ state, and the latter becomes the lowest mixed-symmetry state, which is interpreted as the quadrupole surface oscillation out of phase between protons and neutrons. Even when the system leaves from the $U(5)$-limit slightly, a 2^+ state like Eq.(2.17) is expected to be the lowest mixed-symmetry state.

In the actual usage of the IBM-2, the following hamiltonian is often adopted,

$$H^B = \sum_{\rho=\pi,\nu} \epsilon_{d_\rho} \hat{N}_{d_\rho} - \kappa Q_\pi^B \cdot Q_\nu^B, \tag{2.18}$$

where $\hat{N}_{d_\rho}$ is the number operator of d_ρ-bosons, and

$$Q_\rho^B = [s_\rho^\dagger \tilde{d}_\rho + d_\rho^\dagger s_\rho]^{(2)} + \chi_\rho [d_\rho^\dagger \tilde{d}_\rho]^{(2)}. \quad (\rho = \pi, \nu) \tag{2.19}$$

Since the main part of the correlation between identical nucleons is already included in the bosons, only $Q_\pi^B \cdot Q_\nu^B$ interaction is taken into account as the two-body interaction. It is remarked that the $Q_\pi^B \cdot Q_\nu^B$ interaction is derived from the $Q_\pi \cdot Q_\nu$ interaction in the nucleon system by the boson mapping. Here we assume the relation $\epsilon_{d_\pi} = \epsilon_{d_\nu}$ for the sake of simplicity, as is often

adopted in phenomenological studies. Then the first term on the right-hand side of Eq.(2.18) is scalar with respect to the F-spin. In the vicinity of the $U(5)$-limit, the first term in Eq.(2.18) dominates the global structure of the energy spectrum. If $\kappa = 0$, the two states of Eq.(2.15) are degenerate in energy. Once the κ is switched on, the symmetric state of Eq.(2.16) becomes lower, while the mixed-symmetry state of Eq.(2.17) goes up. This mechanism is explained in Appendix A. As far as the χ_π and χ_ν are not so different from each other as in most IBM-2 phenomenological calculations, the F-spin symmetry is approximately conserved.

The above situation is schematically illustrated in Fig.1, in the case of $N_\pi = N_\nu = 1$. If we have no proton-neutron interaction, the two states of Eq.(2.15) are degenerate as shown in the left column of Fig.1. When a proton-neutron interaction, for instance the second term of Eq.(2.18), is turned on, the linear combination with $F = F_{max}$, Eq.(2.16), is energetically favored, while the other linear combination of Eq.(2.17) is unfavored. Thus the states split according to the F-spin, as in the middle column of Fig.1. In actual cases there might be several non-collective states around the mixed-symmetry state. Therefore the state of Eq.(2.17) would further split into a few states by coupling to the non-collective degrees of freedom. The right column of Fig.1 displays this situation. Actually the energy levels shown in the right column are obtained from the shell model calculation in ^{56}Fe explained in Sections 4 and 5.

2.2 Expected Properties of Mixed-Symmetry 2^+ State

We discuss some properties of mixed-symmetry states predicted within the IBM-2. Excitation energies of mixed-symmetry states are somewhat ambiguous, on account of the following reason. The so-called Majorana interaction is usually introduced, in order to reproduce low-lying energy levels. This interaction causes large split of states with different F-spin. We, however, cannot precisely determine the strength of the Majorana interaction from the energies of lowest-lying states. Moreover, microscopic basis of the interaction is not clear yet. Only our knowledge is obtained from the experiments of the scissors mode, which says that energy split between $F = F_{max}$ states and $F = F_{max} - 1$ states is roughly 3MeV in $A \sim 160$ region[24].

On the other hand, γ-decay probabilities from some mixed-symmetry states to totally symmetric states have been discussed rather well[12, 13]. We first consider $E2$ transition from the state of Eq.(2.17) to the ground state in the $U(5)$-limit, Eq.(2.13). If we express the boson $E2$ operator as

$$T^B(E2) = \sum_{\rho=\pi,\nu} e^B_\rho Q^B_\rho, \tag{2.20}$$

where Q^B_ρ is defined in Eq.(2.19), we obtain

$$\langle 0^+_S(s^{N_B}) \| T^B(E2) \| 2^+_M(s^{N_B-1}d) \rangle = \sqrt{\frac{5N_\pi N_\nu}{N_B}}(e^B_\pi - e^B_\nu). \tag{2.21}$$

It should be compared with the transition from the symmetric state Eq.(2.16) to the ground state,

$$\langle 0^+_S(s^{N_B}) \| T^B(E2) \| 2^+_S(s^{N_B-1}d) \rangle = \sqrt{\frac{5}{N_B}}(e^B_\pi N_\pi + e^B_\nu N_\nu). \tag{2.22}$$

Though the transition of Eq.(2.21) is smaller than that of Eq.(2.22), it seems still larger than fully non-collective transitions.

For a rough estimation of $B(E2)$ values in practice, we apply the OAI mapping[5] to ^{56}Fe, assuming the ^{56}Ni core to be inert. In this case we have

$N_\pi = N_\nu = 1$. The valence protons occupy the single-j shell of the $0f_{7/2}$ orbit and the two valence neutrons are in the degenerate orbits of $(0f_{5/2}1p_{3/2}1p_{1/2})$. Then the creation operator of the S_ν-pair is

$$S^\dagger_\nu = \sum_{j=0f_{5/2},1p_{3/2},1p_{1/2}} \sqrt{\frac{\Omega_j}{2}}[a^\dagger_j a^\dagger_j]^{(0)}, \tag{2.23}$$

where

$$\Omega_j = j + \frac{1}{2}. \tag{2.24}$$

We assume the creation operator of the D_ν-pair to be

$$D^\dagger_\nu \propto [Q_\nu, S^\dagger_\nu], \tag{2.25}$$

where Q_ν represents the $E2$ transition operator for neutrons,

$$Q_\nu = [r^2 Y^{(2)}]_\nu. \tag{2.26}$$

If we adopt the effective charges for valence nucleons of

$$e^{eff}_\pi = 2.0e, \quad e^{eff}_\nu = 1.0e, \tag{2.27}$$

which are adopted values in the shell model in Ref.[25], we have

$$e^B_\pi = 9.5[efm^2], \quad e^B_\nu = 6.8[efm^2]. \tag{2.28}$$

We note that the χ parameters are obtained from this mapping as

$$\chi_\pi = -0.93, \quad \chi_\nu = -1.19. \tag{2.29}$$

Then we obtain

$$\begin{aligned} B(E2; 2^+_S(s^{N_B-1}d) \to 0^+_S(s^{N_B})) &= \frac{1}{5}|\langle 0^+_S(s^{N_B})\|T^B(E2)\|2^+_S(s^{N_B-1}d)\rangle|^2 \\ &= 133[e^2fm^4], \end{aligned} \tag{2.30}$$

$$\begin{aligned} B(E2; 2^+_M(s^{N_B-1}d) \to 0^+_S(s^{N_B})) &= \frac{1}{5}|\langle 0^+_S(s^{N_B})\|T^B(E2)\|2^+_M(s^{N_B-1}d)\rangle|^2 \\ &= 3.6[e^2fm^4]. \end{aligned} \tag{2.31}$$

In more realistic cases when the nucleus is deformed to some extent, the $B(E2)$ values would be larger due to deformation. Eq.(2.30) is compared with the experimental data

$$B(E2; 2^+_1 \to 0^+_1) = 211[e^2fm^4] \tag{2.32}$$

in ^{56}Fe[26]. It should be noted that the $B(E2)$ value in Eq.(2.31) is comparable with the Weisskopf unit of $12.7[e^2fm^4]$ at $A = 56$.

When we ignore the radial dependence of the core polarization effect, the proton contribution seems to be located with a little larger radius than the neutron contribution in the collective 2^+ transition densities, due to the Coulomb force. It is remarked that this is not true in the actual case, as will be discussed in Section 5, since the neutron contribution purely comes from the polarization effect. If the positions of the proton and neutron peaks are sufficiently displaced compared with their widths, a distinct node emerges in the total transition density from the ground state to the mixed-symmetry 2^+ state, since the signs of the proton and neutron contributions are opposite. Fig.2 shows this situation schematically. The existence of the node will be seen as an enhancement of high q (momentum transfer) component in the inelastic form factor. We should remark, however, that only overall quenching due to the cancellation takes place in the total transition density, if the peaks in the proton and neutron transition densities are broader than their displacement.

In the IBM-2, $M1$ transition reflects the proton-neutron symmetry. In the usual IBM-2 description, $M1$ transition operator has the one-body form as

$$T^B(M1) = \sqrt{\frac{3}{4\pi}} \sum_{\rho=\pi,\nu} g^B_\rho J^B_\rho = \sqrt{\frac{3}{4\pi}}(g^B_\pi J^B_\pi + g^B_\nu J^B_\nu), \tag{2.33}$$

where J^B_π (J^B_ν) denotes the proton (neutron) angular momentum operator,

$$J^B_\rho = \sqrt{10}[d^\dagger_\rho \tilde{d}_\rho]^{(1)}. \tag{2.34}$$

This operator can be rewritten as

$$T^B(M1) = \frac{1}{2}\sqrt{\frac{3}{4\pi}}[(g^B_\pi + g^B_\nu)(J^B_\pi + J^B_\nu) + (g^B_\pi - g^B_\nu)(J^B_\pi - J^B_\nu)]. \tag{2.35}$$

The first term never produces transitions, since it is proportional to the total angular momentum. At first sight the operator $(J^B_\pi - J^B_\nu)$ vary only the proton-neutron symmetry, since it rotates proton part of wavefunction relative to neutron part. In fact, the $M1$ transition between two of the $F = F_{max}$ states is forbidden, as proved in Appendix B. On the other hand, $M1$ transition from a mixed-symmetry state to a totally symmetric state may become so large. In practice, the scissors 1^+ state has quite large $M1$ excitation strength from the ground state ($B(M1) \sim 3\mu_N^2$).

We expect relatively strong $M1$ transition from the state of Eq.(2.17) to the state of Eq.(2.16). Matrix element of this transition is

$$\langle 2^+_S(s^{N_B-1}d)\|T^B(M1)\|2^+_M(s^{N_B-1}d)\rangle = \sqrt{\frac{3}{4\pi}} \cdot \frac{\sqrt{30N_\pi N_\nu}}{N_B}(g^B_\pi - g^B_\nu). \tag{2.36}$$

Thus we obtain

$$B(M1; 2^+_M(s^{N_B-1}d) \to 2^+_S(s^{N_B-1}d)) = \frac{9}{2\pi}\frac{N_\pi N_\nu}{N_B^2}(g_\pi - g_\nu)^2. \tag{2.37}$$

Note that the mixed-symmetry 2^+ state exhausts the $M1$ transition strength from the 2^+_1 state in the IBM-2 space, namely,

$$|2^+_M(s^{N_B-1}d)\rangle \propto P_{\mathcal{O}\{2^+_S(s^{N_B-1}d)\}}(J^B_\pi - J^B_\nu)|2^+_S(s^{N_B-1}d)\rangle, \tag{2.38}$$

where the operator $P_{\mathcal{O}}$ expresses the Schmidt orthogonalization to the state assigned by the curly bracket. When $N_\pi \simeq N_\nu \simeq \frac{N_B}{2}$, Eq.(2.37) becomes

$$B(M1; 2^+_M(s^{N_B-1}d) \to 2^+_S(s^{N_B-1}d)) \simeq \frac{9}{8\pi}(g_\pi - g_\nu)^2. \tag{2.39}$$

Note that this value does not depend on the total boson number.

From a microscopic standpoint, the boson g-factors are considered as[27]

$$g^B_\pi \simeq 1.0[\mu_N], \quad g^B_\nu \simeq 0.0[\mu_N], \tag{2.40}$$

since the spin contents of the S- and D-pairs are expected to be negligibly small. The Elliott's $SU(3)$ model[28] gives an example of vanishing spin in collective S- and D-pairs. Provided that $g^B_\pi - g^B_\nu \simeq 1.0\mu_N$, we can estimate the above $M1$ transition rate as

$$B(M1; 2^+_M(s^{N_B-1}d) \to 2^+_S(s^{N_B-1}d)) \simeq 0.36[\mu_N^2]. \tag{2.41}$$

This $B(M1)$ value is not so extremely large as in the case of the scissors mode, since the system is spherical. While deformed nucleus contain some components with large values of proton and neutron angular momenta, the states of Eqs.(2.16) and (2.17) have at most $\langle J_\pi \rangle = 2$ or $\langle J_\nu \rangle = 2$ component.

As a reference, we consider the $B(M1)$ value from the 0^+_1 state to the 1^+_1 state in the $SU(3)$-limit. This 1^+_1 state is the scissors state. The $B(M1)$ is estimated as[8, 29, 30],

$$\begin{aligned} B(M1; 0^+_1 \to 1^+_1) &= \frac{3}{4\pi}\frac{8N_\pi N_\nu}{2N_B - 1}(g_\pi - g_\nu)^2 \\ &\sim \frac{3}{4\pi} \cdot 4\frac{N_\pi N_\nu}{N_B}(g_\pi - g_\nu)^2. \end{aligned} \tag{2.42}$$

If we assume $N_\pi \simeq N_\nu \simeq \frac{N_B}{2}$ again, it becomes

$$B(M1; 0^+_1 \to 1^+_1) \sim \frac{3}{4\pi}N_B(g_\pi - g_\nu)^2, \tag{2.43}$$

which is very large in general, since N_B is large in deformed nuclei.

There could be some fragmentation of the mixed-symmetry 2^+ state, as in the case of the scissors mode. Then $B(M1)$ values in each observed state will be smaller than the value in Eq.(2.41), and could sometimes be comparable to non-collective $M1$ transitions like the spin mode. Hence we should be careful in experimental search for the mixed-symmetry 2^+ mode in nearly spherical nuclei, since some non-collective states might be present in the energy region of the mixed-symmetry state.

The 0_2^+ state in the $U(5)$-limit of the IBM-2 should be[30]

$$\begin{aligned} |0_S^+(s^{N_B-2}d^2)\rangle &= \frac{1}{\sqrt{N_B(N_B-1)}}(\sqrt{N_\pi(N_\pi-1)}|s_\pi^{N_\pi-2}d_\pi^2 s_\nu^{N_\nu};0^+\rangle \\ &\quad +\sqrt{2N_\pi N_\nu}|s_\pi^{N_\pi-1}d_\pi s_\nu^{N_\nu-1}d_\nu;0^+\rangle \\ &\quad +\sqrt{N_\nu(N_\nu-1)}|s_\pi^{N_\pi}s_\nu^{N_\nu-2}d_\nu^2;0^+\rangle). \end{aligned} \tag{2.44}$$

In realistic cases there occurs an admixture of this state into the ground state. This mixing is related to a deformation of the nucleus. The state of Eq.(2.44) has a large $B(M1)$ from a mixed-symmetry 1^+ state,

$$\begin{aligned} |1_M^+(s^{N_B-2}d^2)\rangle &= |s_\pi^{N_\pi-1}d_\pi s_\nu^{N_\nu-1}d_\nu;1^+\rangle \\ &\propto (J_\pi^B - J_\nu^B)|0_S^+(s^{N_B-2}d^2)\rangle. \end{aligned} \tag{2.45}$$

It is pointed out that any 1^+ state in the IBM-space is never totally symmetric. Thus the admixture of the $|0_S^+(s^{N_B-2}d^2)\rangle$ component in the ground state would enable us to search for the mixed-symmetry 1^+ state, based on the $B(M1)$ measurement.

3 Experimental Studies of Mixed-Symmetry 2^+ States

3.1 $50 < A < 60$ Region

As discussed in Section 1, there have recently been some reports of the mixed-symmetry 2^+ states in $50 < A < 60$ region, based on the experiments[17, 18, 31, 32].

We first see ^{56}Fe. In the usual IBM-2 description, we have the boson numbers of $N_\pi = N_\nu = 1$ in this nucleus, and consequently $F_0 = 0$ and $F_{max} = 1$. One might notice that in this nucleus the $F = F_{max} - 1$ states are totally anti-symmetric states within the IBM-2. We, however, call the states mixed-symmetry states in this thesis, since the $F = F_{max} - 1$ states constitute a class of the lowest mixed-symmetry states, which we are interested in. Eid *et al.* reported that the 2_2^+ and 2_3^+ states of ^{56}Fe have relatively large $B(M1)$ values to the 2_1^+ state[17],

$$B(M1;2_2^+ \to 2_1^+) = 0.23[\mu_N^2], \quad B(M1;2_3^+ \to 2_1^+) = 0.15[\mu_N^2]. \tag{3.1}$$

It is noted that the sum of the above $B(M1)$ value is almost the same as the estimated value of Eq.(2.41). They tried to describe these three lowest-lying 2^+ states by identifying them as IBM-2 states. They assume the 0_1^+ to be purely the state of Eq.(2.13) and the 2_1^+ to be the state of Eq.(2.16);

$$|0_1^+\rangle = |0_S^+(s^2)\rangle = |s_\pi s_\nu\rangle, \tag{3.2}$$

$$|2_1^+\rangle = |2_S^+(sd)\rangle = \frac{1}{\sqrt{2}}(|d_\pi s_\nu\rangle + |s_\pi d_\nu\rangle). \tag{3.3}$$

Then they claim that the 2_2^+ and 2_3^+ states share the mixed-symmetry component $|2_M^+(sd)\rangle = \frac{1}{\sqrt{2}}(|d_\pi s_\nu\rangle - |s_\pi d_\nu\rangle)$ and the other symmetric component

$|2^+_S(d^2)\rangle = |d_\pi d_\nu; 2^+\rangle$,

$$|2^+_2\rangle = 0.775|2^+_M(sd)\rangle + 0.632|2^+_S(d^2)\rangle, \quad (3.4)$$

$$|2^+_3\rangle = -0.632|2^+_M(sd)\rangle + 0.775|2^+_S(d^2)\rangle, \quad (3.5)$$

The mixing amplitudes are determined from the ratio of the $B(M1)$ values of Eq.(3.1). Hartung *et al.* insisted[31] that the (e, e') form factors of the excitations to these three 2^+ states are consistent with the above interpretation to a certain extent. In that analysis it was assumed that the proton bosons are constructed by the $(0f_{7/2})^{-2}$ proton pairs, while the neutron bosons by the $(1p_{3/2})^2$ neutron pairs.

These assumptions on wavefunctions, both the IBM wavefunctions of Eqs.(3.2∼3.5) and the nucleonic structure of bosons, seem to be too simple. Moreover, in Ref.[31] they introduced normalization factors, in order to reproduce the absolute values of the (e, e') form factors. The factors range from 0.2 to 2.0, significantly dependent on the states[33]. On the other hand, the 2^+_4 state is beyond the scope of their description. The $B(M1; 2^+_4 \to 2^+_1)$ value is, however, as large as $B(M1; 2^+_3 \to 2^+_1)$[18];

$$B(M1; 2^+_4 \to 2^+_1) = 0.13 \begin{matrix}+0.08 \\ -0.04\end{matrix} [\mu_N^2]. \quad (3.6)$$

It follows that there is some ambiguity to judge from the $B(M1)$ values which states have the mixed-symmetry component. We have only three 2^+ states in the IBM-2 space. A larger model space is necessary to account for the $M1$ transitions. Although Collins *et al.* suggest that the g-boson degrees of freedom should be included[18], they gave no concrete description. We will discuss this point later, in Section 5.

There is a report based on $B(M1)$ values also in ^{54}Cr and ^{52}Ti[18, 19]. In ^{54}Cr, it is pointed out that the 2^+_3 state has relatively large $B(M1)$ to the

2^+_1[19],

$$B(M1; 2^+_3 \to 2^+_1) = 0.39 \pm 0.06 [\mu_N^2]. \quad (3.7)$$

The lower limit of $B(M1; 2^+_4 \to 2^+_1)$ is also reported as[18]

$$B(M1; 2^+_4 \to 2^+_1) > 0.2 [\mu_N^2]. \quad (3.8)$$

In ^{52}Ti, the 2^+_2 and 2^+_3 states have a large $B(M1)$ value to the 2^+_1[19],

$$B(M1; 2^+_2 \to 2^+_1) = 0.55 \begin{matrix}+0.24 \\ -0.47\end{matrix} [\mu_N^2], \quad B(M1; 2^+_3 \to 2^+_1) > 0.17 [\mu_N^2]. \quad (3.9)$$

The $M1$ probability from the 2^+_2 state seems already larger than the value of Eq.(2.41). However, we should remark that the measurement is not so accurate in ^{52}Ti.

3.2 Other Mass Region

There were some reports of the mixed-symmetry 2^+ states in other mass region. Hamilton *et al.* studied $N = 84$ isotones, ^{140}Ba, ^{142}Ce and ^{144}Nd[21, 34]. It is suggested that the 2^+_3 states of these nuclei are the mixed-symmetry states, based on the $E2/M1$ mixing ratio of the γ transition to the 2^+_1 state as well as the branching ratio to the 2^+_1 and 0^+_1 states. The 2^+_3 states has $Ex \simeq 2$MeV, commonly for all of these nuclei. The 2^+_3 state in ^{200}Hg ($Ex = 1.6$MeV)[35] and the 2^+_4 in ^{124}Te ($Ex = 2.1$MeV)[36] are also reported as candidates of the mixed-symmetry states, based on the remarkably smaller $E2/M1$ mixing ratios than those of some other low-lying 2^+ states.

The mixed-symmetry 2^+ states are studied in $A \sim 110$ regions, by comparing the proton scattering with the deuteron scattering[20]. They deduced the isoscalar and the isovector contributions to the 2^+ transitions from the (p, p') and (d, d') cross sections. It is noted that the transitions between the

symmetric states and the mixed-symmetry ones should predominantly be isovector transitions in the description by nucleonic degrees of freedom. In ^{104}Pd, ^{110}Pd and ^{112}Cd, though there seems to be some enhancement of the isovector contribution in some states in $2 < Ex < 3$MeV, the existence of the mixed-symmetry states is not so evident. The 2^+ state with $Ex = 3.07$MeV in ^{106}Pd is reported to have remarkably large isovector transition strength to the ground state than isoscalar one. This state is one of the candidates of the mixed-symmetry 2^+ state at present. The absolute value of the isovector matrix element, however, is not so large. Since the mixed-symmetry state is one of the collective state, there still remains an obscurity.

Although there are some reports of candidates of the mixed-symmetry 2^+ state, decisive evidence is lacked. It is assumed in most of the reports that all the low-lying states can be described in the IBM-2. In spherical nuclei, however, it is not so apparent. We are treating the energy region of $Ex = 2 \sim 3$MeV, and there could be non-collective states in this energy region. Furthermore, we do not know the properties of the mixed-symmetry 2^+ state fully well, especially when the mixed-symmetry 2^+ component is somewhat split. There is even a possibility that the component is too much fragmented to be identified. Therefore a theoretical study from a microscopic standpoint is highly desired.

4 Shell Model Calculation

4.1 Survey of Previous Shell Model Calculations in pf-shell

Shell model calculations in the pf-shell have been attempted for many years. In most earlier calculations, excitation across N or $Z = 28$ was assumed to be prohibited, as well as N or $Z = 20$ and 40. Especially for nuclei around the middle of the pf-shell, this truncation of configuration space makes it very easy to carry out shell model calculation. In most of those calculations, effective interactions are determined from phenomenological viewpoints. Comprehensive studies have been performed in the $N, Z \leq 28$ region, by a phenomenological interaction[37]. In the region of $20 < Z \leq 28$ and $28 \leq N < 40$, semi-magic nuclei with N or $Z = 28$ were investigated as first steps[38, 39]. After the earlier works of Refs.[38, 40], Horie and Ogawa tried a shell model calculation with a phenomenological interaction for $N = 29$ and 30 nuclei[41], maintaining the inertness of $N = Z = 28$. They succeeded to reproduce lowest-lying energy levels systematically. Typical example is ^{56}Fe[25]. γ-transition rates are also reproduced well, up to the second state with each spin. We, however, cannot reproduce higher states by their apparatus. For instance, the excitation energy of the 2^+_3 state of ^{56}Fe is overestimated by 0.4MeV, and that of the 2^+_4 state by 0.5MeV. Since these states may be relevant to the mixed-symmetry problem as mentioned in Section 3, this discrepancy is serious in the present study.

There has been several attempts to take into account the excitation from the $0f_{7/2}$ to the $1p_{3/2}$ orbit by one particle[42]. There have been some shell model calculations including the excitation from the $0f_{7/2}$ to any of the $0f_{5/2}$,

$1p_{3/2}$ and $1p_{1/2}$ orbits by one particle[43]. However, the situation does not seem to be improved. It is probable that the pairing correlation relaxes the ^{56}Ni core by exciting two nucleons from the $0f_{7/2}$ to the higher orbits.

In contrast to the empirical interactions discussed so far, Kuo and Brown proposed a realistic interaction, namely an effective interaction derived from a nucleon-nucleon interaction, on the top of the ^{40}Ca core[44]. Though originally they derived the interaction for calculations including the $0g_{9/2}$ orbit, such calculations are still impossible in most nuclei because of too large dimensions. Nevertheless it is worth testing the Kuo-Brown interaction in the pf-shell in the region where the $0g_{9/2}$ orbit scarcely influences low-lying states. The Kuo-Brown interaction has been applied to shell model calculations in the full pf-shell, for $40 < A \leq 44$ nuclei[45]. Though qualitative agreement with the experimental data is found in those calculations, there still remains recognizable discrepancies. A few ways of modification of interaction are proposed[46, 47]. We, however, should take notice that some excitation from the sd-shell might be significantly present in this mass region. Therefore it is desired to test the Kuo-Brown interaction in a sufficiently large model space around the middle of the pf-shell.

Oberlechner and Richert executed a shell model calculation around ^{56}Ni[48], by using another realistic interaction. They, however, could not succeed in reproducing the experimental energy levels so well, presumably because of insufficiency of the model space.

4.2 Model space and Effective Hamiltonian

We shall study the mixed-symmetry problem in $50 < A < 60$ region, based on a shell model calculation with a realistic interaction. Assuming ^{40}Ca to

be a doubly magic inert core, we consider configurations as

$$(0f_{7/2})^{n_1-k}(0f_{5/2}1p_{3/2}1p_{1/2})^{n_2+k}, \tag{4.1}$$

where n_1 and n_2 are defined so that $k = 0$ should give the lowest configurations in which excitation across N or $Z = 28$ is absent. For instance, $n_1 = 14$ and $n_2 = 2$ for ^{56}Fe, since this nucleus has 6 protons and 10 neutrons in the pf-shell. Similarly, $n_1 = 12$ and $n_2 = 2$ for ^{54}Cr, $n_1 = 10$ and $n_2 = 2$ for ^{52}Ti. The present model space contains all configurations of $k = 0, 1$ and 2. We would like to emphasize that such a large configuration space has never been taken. The $k = 2$ configurations evidently plays an essential role in the description of the smear of the inertness of $N = Z = 28$ due to the pairing correlation.

As for an effective hamiltonian, we adopt the Kuo-Brown hamiltonian on the top of the ^{40}Ca core[44]. In this Kuo-Brown hamiltonian, single particle energies are determined from the experiments in one particle states on the ^{40}Ca core; $\epsilon_{0f_{7/2}} = 0.0$MeV, $\epsilon_{0f_{5/2}} = 6.5$MeV, $\epsilon_{1p_{3/2}} = 2.1$MeV and $\epsilon_{1p_{1/2}} = 3.9$MeV. Two-body interaction matrix elements are obtained from the G-matrix derived from the Hamada-Johnston potential, assuming the single particle wavefunction in the harmonic oscillator approximation. We include the $3p$-$1h$ correction. Thus there are no adjustable parameters in the calculation of energy levels. It is noted that there has been little report of such a realistic shell model calculation so far, as mentioned in Subsection4.1. Around the middle of the pf-shell, both the influence of the sd-shell and the sdg-shell is expected to be minimal. The Kuo-Brown interaction may be valid in this region, if the configuration space is sufficiently large. Indeed, the success of the Kuo-Brown interaction in the $k \leq 2$ configuration space is

reported for ^{48}Sc in Ref.[46].

The isospin is conserved, and hereafter we restrict ourselves to the states with the lowest isospin in each nucleus; $T = 2$ states in ^{56}Fe, $T = 3$ in ^{54}Cr and $T = 4$ in ^{52}Ti.

In the numerical calculation, we use an M-scheme shell model code. The present model space is one of the largest one available at present. In the M-scheme, the $M = 0$ space has the largest dimension in even mass nuclei, while the $M = \pm\frac{1}{2}$ space in odd mass nuclei. The dimension is displayed for each nucleus in Table 1, as well as the largest dimension in the JT-scheme.

4.3 Energy Levels

At first we show calculated energy levels of ^{57}Ni, ^{54}Fe and ^{58}Ni, in comparison with the experimental data taken from Refs[50, 51, 52], in Figs.3, 4 and 5. At the same time we mention that the spin-parity of the ground state is correctly reproduced in ^{55}Co. In the $k = 0$ configuration space, we have only one state with $J^P = \frac{7}{2}^-$ in ^{55}Co, three states with $J^P = \frac{3}{2}^-, \frac{5}{2}^-, \frac{1}{2}^-$ in ^{57}Ni and four states with $J^P = 0^+, 2^+, 4^+, 6^+$ in ^{54}Fe. We can see that the corresponding levels are reproduced very well, within the accuracy of 0.2MeV. The content of the wavefunctions in terms of k is displayed in Table 2, where the $k = 0$ configurations are found to be dominant in these states in practice. Table 2 also shows that the ground state of ^{56}Ni already differs from the simple closed core state by 37%. In ^{57}Ni and ^{54}Fe, much larger level density is observed than that obtained in the present calculation in the energy region dominated by the $k > 0$ configurations. The same holds for ^{56}Ni and ^{55}Co. This fact suggests that larger k configurations are necessary in order to reproduce those higher levels. We can say that the *magic* nature of $N = Z = 28$,

which means the large energy gap between the $0f_{7/2}$ and the other pf-shell orbits, is maintained in the present apparatus. We simultaneously find the importance of the $k = 2$ configurations from Table 2.

In ^{58}Ni, there are three 0^+, two 1^+, five 2^+, one 3^+ and two 4^+ states in the $k = 0$ configuration space. The calculated energy levels are in good agreement with the experimental ones, except for the 0^+ states. The calculated 0_2^+ state is much lower than the experimental one. However, the calculated 0_2^+ is highly dominated by the $k = 2$ configurations, as shown in Table 2. It is possible that this remarkable difference of the wavefunction from the ground state makes it difficult to observe the state. If we consider the calculated 0_3^+ state to correspond to the observed 0_2^+, the agreement becomes satisfactory. Then a 0^+ state, which has not observed yet, seems to exist with $Ex \leq 2.2$MeV. We note that the calculated energy would be less accurate than other states, because the wavefunction mainly consists of the largest k in the calculation. Admixture of $k > 2$ configurations in this state would not be small if one carries out a calculation in larger configuration space. The 2_3^+ state is also dominated by the $k = 2$ configurations. The $B(E2; 2_3^+ \rightarrow 0_2^+)$ value is fairly large ($250[e^2fm^4]$) in the present calculation, suggesting a quasi-band structure. Although the 2_3^+ state is connected with an observed state by energy in Fig.5, this correspondence is not so evident. The calculated 2_3^+ state might not have been observed as the 0_2^+ state, because of the difference in configuration. Even if it is true, the agreement between calculation and experiment is not disturbed so much.

The experimental and calculated energy levels of ^{56}Fe are shown in Fig.6. It is demonstrated that the spectrum seen in experiments is excellently reproduced for $Ex < 4$MeV, apart from the 3^- state of $Ex = 3.07$MeV, which

is outside the present configuration space. Discrepancies in the excitation energies are less than 0.2MeV again. In $Ex > 4$MeV, we obtain lower level density than the experimental data. This fact suggests the necessity of larger k configurations in order to reproduce the levels in this region. We show the calculated excitation energies of the yrast states up to $J^P = 8^+$ in Table 3, which also agree with the experimental energies. Most of the states under consideration mainly consists of the $k = 0$ configurations by $48 \sim 56\%$, as is shown in Table 2. In the 2_4^+ state the $k = 1$ configurations is dominant. The wavefunction of this state, however, seems as good as those of other states, since the probability of the $k = 2$ configurations is similar to other states. This can be checked by some transition properties, such as γ-transition rate, (e, e') form factor and $(\vec{p}, p')$ differential cross section.

The energy levels of ^{54}Cr and ^{52}Ti are displayed in Figs.7 and 8, respectively. Agreement between calculated one and experimental one is sufficiently good, within the accuracy of 0.2MeV. Most of the states under consideration are dominated by the $k = 0$ configurations again, as shown in Table 2.

4.4 Electromagnetic properties

Next we turn to $E2$ and $M1$ transition probabilities. We use the $E2$ operator

$$T(E2) = \sum_{\rho=\pi,\nu} e_\rho^{eff} Q_\rho, \tag{4.2}$$

where

$$Q_\rho = [r^2 Y^{(2)}]_\rho, \tag{4.3}$$

and the single particle wavefunctions in the harmonic oscillator potential, with the oscillator length of $b = A^{1/6}[fm]$. The effective charges of

$$e_\pi^{eff} = 1.4e, \; e_\nu^{eff} = 0.9e \tag{4.4}$$

are adopted, by adjusting to the data in ^{56}Fe. These effective charges are rewritten in terms of isoscalar (IS) and isovector (IV) polarization charges as

$$\delta e_{IS} = 0.65e, \; \delta e_{IV} = -0.25e. \tag{4.5}$$

The calculated and measured $B(E2)$ values in ^{56}Fe, ^{54}Cr and ^{52}Ti are exhibited in Tables 4, 5 and 6, denoted by 'Cal.(A)', as well as the $E2$ static moments of the 2_1^+ state. An overall agreement is found for these nuclei by the above effective charges. Tables 4, 5 and 6, also show the $B(E2)$ values and $E2$ moments calculated by the j-dependent effective charges obtained microscopically, as will be explained in Subsection 4.5. These values are denoted by 'Cal.(B)'. At present we point out good agreement of the 'Cal.(B)' values with the 'Cal.(A)' values. Here we do not discuss the properties of the individual states of these nuclei. We will do that in Sections 5 and 7.

It is known that larger effective charges than those in systematics are needed in order to adjust $B(E2; 2_1^+ \to 0_1^+)$ in the semi-magic nuclei ^{54}Fe and ^{58}Ni[38, 39]. Shimizu and Arima described the $B(E2; 2_1^+ \to 0_1^+)$ value in ^{58}Ni by taking into account the $k = 1$ and 2 configurations, based on the pseudo-$SU(3)$ picture[54]. Though the present calculation includes the $k = 1$ and 2 configurations, anomalously larger effective charges are still necessary to adjust the $B(E2)$ values in ^{54}Fe and ^{58}Ni, as is seen from Tables 7 and 8. If we determine the effective charges from the $B(E2; 2_1^+ \to 0_1^+)$ values in ^{54}Fe and ^{58}Ni, we obtain

$$e_\pi^{eff} = 1.75e, \; e_\nu^{eff} = 1.20e, \tag{4.6}$$

namely,

$$\delta e_{IS} = 0.975e, \; \delta e_{IV} = -0.225e. \tag{4.7}$$

Comparing these values with the values in Eq.(4.5), δe_{IS} seems to be enhanced considerably in ^{54}Fe and ^{58}Ni, while δe_{IV} is not different so much. Therefore, provided that the abnormal $B(E2)$ in those two nuclei are caused by the same reason, it should be deduced to an enhancement of δe_{IS}.

The $B(M1)$ values in ^{56}Fe, ^{54}Cr and ^{52}Ti are also displayed in Tables 9, 10 and 11 respectively, as well as the $M1$ static moments of the 2_1^+ state. The experimental values are taken from Refs.[26, 51, 53], which are compilations of some data and slightly different from the values shown in Section 3. The $M1$ quantities are described by the following one-body operator,

$$T(M1) = \sqrt{\frac{3}{4\pi}} \sum_{\rho=\pi,\nu} (g_{l,\rho}^{eff} L_\rho + g_{s,\rho}^{eff} S_\rho + g_{p,\rho}^{eff} \{[Y^{(2)} S]^{(1)}\}_\rho), \tag{4.8}$$

Here L_ρ and S_ρ denote orbital and spin angular momentum operators, respectively. The $\{[Y^{(2)}S]^{(1)}\}_\rho$ is a symbolic expression defined as

$$\{[Y^{(2)}S]^{(1)}\}_\rho = \sum_{i\in\rho} [Y^{(2)}(\hat{\mathbf{r}}_i) s_i]^{(1)}, \tag{4.9}$$

where i runs over each valence protons or neutrons, and s_i denotes spin operator of the i-th particle. Though the single particle parameters $g_{l,\rho}^{eff}$, $g_{s,\rho}^{eff}$ and $g_{p,\rho}^{eff}$ generally depend on l, the orbital angular momentum of the single particle orbit, we neglect the dependence, as is often assumed. Furthermore, we set $g_{p,\rho}^{eff} = 0$. Namely, the employed $M1$ operator is

$$T(M1) = \sqrt{\frac{3}{4\pi}} \sum_{\rho=\pi,\nu} (g_{l,\rho}^{eff} L_\rho + g_{s,\rho}^{eff} S_\rho). \tag{4.10}$$

We adopt single particle g-factors of

$$g_{l,\pi}^{eff} = 1.0\mu_N,\ g_{l,\nu}^{eff} = 0.0\mu_N,\ g_{s,\pi}^{eff} = 0.5 g_{s,\pi}^{free},\ g_{s,\nu}^{eff} = 0.5 g_{s,\nu}^{free}, \tag{4.11}$$

where $g_{s,\rho}^{free}$ denotes the g-factor of free nucleon. The quenching factor for $g_{s,\rho}$ is the same as that adopted in Ref.[41], though microscopic calculations predict the factor much closer to the unity[56, 57]. Good agreement is obtained, except for $B(M1; 2_3^+ \to 2_1^+)$ in ^{56}Fe, which is a non-collective transition as will be discussed later. The above form of the $M1$ operator might be insufficient for non-collective transitions. Generally non-collective transitions are sensitive to details of wavefunctions, and therefore the transition operator should be chosen more precisely in order to reproduce the data, than for collective transitions.

The $M1$ quantities in ^{55}Co and ^{57}Ni are exhibited in Tables 12 and 13. The sign of the experimental magnetic moment of the $(\frac{3}{2})_1^-$ state in ^{57}Ni, which has not been specified[55], is conjectured from the calculated value. The adopted sign is consistent with the Schmidt value. They are reproduced quite well by the above operator and parameters, except for $B(M1; (\frac{5}{2})_1^- \to (\frac{3}{2})_1^-)$ in ^{57}Ni. This $M1$ transition is fairly large and therefore it cannot be adjusted by the $M1$ operator of Eq.(4.10), since the single particle transition from the $0f_{5/2}$ orbit to the $1p_{3/2}$ plays an essential role in this transition. The necessity of the additional $\{[Y^{(2)}S]^{(1)}\}_\nu$ term is suggested. If we determine $g_{p,\nu}$, coefficient of the $\{[Y^{(2)}S]^{(1)}\}_\nu$, from $B(M1; (\frac{5}{2})_1^- \to (\frac{3}{2})_1^-)$ in ^{57}Ni, we have $|g_{p,\nu}^{eff}| \sim 3\mu_N$. This value is much larger than the Towner's microscopic value[56], which is obtained by taking into account the effects of the core polarization and the meson exchange current. This additional term does not influence collective transition probabilities so much, since the spin content is almost saturated in collective states. Though $B(M1; 2_3^+ \to 2_1^+)$ in ^{56}Fe is affected by this additional term, we must further increase the $|g_{p,\nu}^{eff}|$ value ($\sim 10\mu_N$) in order to reproduce the experimental data.

Here we also show the $M1$ moments and transition probabilities in ^{55}Co and ^{57}Ni calculated from Towner's microscopic parameters[56], which contain dependence on the orbits for the g-parameters. For the magnetic moment of the ground state in ^{55}Co, we obtain

$$\mu((\tfrac{7}{2})^-_1) \;=\; 4.97[\mu_N]. \tag{4.12}$$

In ^{57}Ni, we obtain

$$\mu((\tfrac{3}{2})^-_1) \;=\; -1.11[\mu_N], \tag{4.13}$$

and

$$\begin{aligned} B(M1;(\tfrac{5}{2})^-_1 \to (\tfrac{3}{2})^-_1) &= 7\times 10^{-6}[\mu_N^2], \\ B(M1;(\tfrac{1}{2})^-_1 \to (\tfrac{3}{2})^-_1) &= 0.67[\mu_N^2]. \end{aligned} \tag{4.14}$$

We get a remarkable agreement for the magnetic moment of the ground state of ^{55}Co, while further quenching for $g_{s,\nu}$ and some enhancement of $g_{p,\nu}$ seems to be required in ^{57}Ni. We mention that the experimental data are not reproduced in other nuclei discussed above, if we use Towner's parameters[56].

We summarize this subsection. The $E2$ transition probabilities and moments are systematically reproduced by the shell model density matrices with the j-independent effective charges of Eq.(4.4), apart from the anomalously large $B(E2)$ in ^{54}Fe and ^{58}Ni. We also acquire an overall reproduction of the $M1$ transition rates and moments, by adopting the single particle g-factors of Eq.(4.11). There remain some discrepancies in non-collective $M1$ transitions, suggesting the necessity of additional operators.

4.5 Form Factors

We calculate longitudinal form factors of electron inelastic scattering with the two units of the angular momentum transfer ($C2$), from the ground state to several 2^+ states. We acquire more precise information from the form factors than from the γ-transition probabilities. The method of Sagawa-Brown[59], which was shown to work very well around doubly magic core for longitudinal form factors with collectivity, is used for this calculation. Though the Kuo-Brown interaction is calculated by assuming the harmonic oscillator single particle wavefunctions, here we obtain the radial part of the single particle wavefunctions by the Hartree-Fock (HF) calculation. We give up the consistency between them. There has been no successful calculation keeping the consistency so far, and this problem is beyond the scope of this work.

To be in more detail for the prescription of Sagawa-Brown, single particle wavefunctions are obtained by the HF calculation with the SGII Skyrme interaction[60] at the ^{56}Ni core, assuming the closure of the $0f_{7/2}$ orbit. Transition densities from the HF state to isoscalar (IS) and isovector (IV) giant quadrupole resonance (GQR) states are calculated by the random phase approximation (RPA)[61]. We search GQR states in the range of $10 < Ex < 70$MeV, and obtain one isolated IS-GQR state at $Ex \simeq 17$MeV and twenty-four IV-GQR states fragmented over $Ex = 20 \sim 35$MeV. In Fig.9 we show the response functions defined by

$$S(E) = \sum_n |\langle \omega_n^{(\lambda)}|T^{(\lambda)}|0\rangle|^2 \delta(E-E_n), \tag{4.15}$$

where the state $|0\rangle$ is the HF state, $|\omega_n^{(\lambda)}\rangle$ an excited state with the angular momentum λ. In this case $\lambda = 2$, and $T^{(\lambda)}$ stands for the operator $r^2Y^{(2)}$ or

$r^2Y^{(2)}\tau_z$. The spreading width is not included in Fig.9. By classifying the transition densities at the peak energies through their shapes, we select nine typical IV-GQR peaks as well as the IS-GQR peak. The transition strengths are assumed to concentrated in the selected GQR peaks, in order to estimate core polarization effect. The adopted peaks and the corresponding transition strengths are listed in Table 14. The core polarization effect caused by these GQR states is incorporated into the HF single particle wavefunctions with the mixing amplitudes evaluated by the perturbation. Then we can calculate the single particle transition densities by renormalizing the radial part of the single particle wavefunctions, as discussed in Appendix C. In the RPA calculation and the evaluation of the mixing amplitudes, residual particle-hole interaction is derived from the SGII Skyrme interaction, consistently with the HF calculation. All steps of this renormalization are carried out at the ^{56}Ni core.

With the renormalized single particle transition densities, the $C2$ form factors are calculated from the shell model density matrices. In spite of the presence of the 2^+ transition in the $0\hbar\omega$ space from the ^{56}Ni core, the high energy considered in dealing with the GQR states will ensure the orthogonality between the RPA space and the shell model space. The nucleon finite-size effect is incorporated in the dipole approximation[62], and contribution of center-of-mass motion is subtracted in the harmonic oscillator approximation[63]. The plane wave Born approximation (PWBA) is employed, taking into account the Coulomb distortion effect in terms of the effective momentum transfer q_{eff}. This calculation includes no adjustable parameter.

The results for ^{56}Fe are shown in Fig.10, compared with experimental

data taken from Refs.[31, 64, 65]. In the experiments, transverse mode was not separated, though most of the reaction is known to be dominated by the $C2$ mode[66]. The form factors calculated without the core polarization effects are displayed in Fig.10 by dotted lines. They reflect only the proton wavefunctions, since the bare electric charges are employed. The form factors of the excitations to the 2_1^+ and 2_2^+ states is excellently reproduced by the present calculation with the core polarization effect. Though there are little experimental data of the form factor to the 2_4^+, it should be noticed that the first peak is higher than that of the 2_2^+ and 2_3^+ state, and its order of magnitude is reproduced by the present calculation. This property are not explained by the wavefunction of Ref.[31] nor [58]. The form factor to the 2_3^+ state is not reproduced so well. This must be caused by the fact that this state does not have the collectivity, as will be discussed in Section 5.

In Fig.11, the transition densities are shown. These transition densities are defined as

$$\rho^{tr}(r) = \frac{1}{\sqrt{5}}\langle f \| \sum_i e_i \frac{\delta(r-r_i)}{r^2} Y^{(2)}(\hat{\mathbf{r}}_i) \| i \rangle. \tag{4.16}$$

The typical single particle transition densities are displayed in Fig.12. We will discuss them in Section 5.

The $C2$ form factors in ^{54}Cr are shown in Fig.13. The experimental data are reproduced quite well with respect to the 2_1^+ state. As for the 2_2^+ state, the shape is reproduced though the absolute value is overall underestimated by the factor of 2. It is remarked that this transition is not collective, as will be discussed in Section 7. There are no reported data with respect to the 2_3^+ and 2_4^+ states. There are no data of transition form factors in ^{52}Ti, since this nucleus is unstable.

In Fig.14 and Fig.15, the inelastic form factors from the 0_1^+ to the 2_1^+ states in ^{54}Fe and ^{58}Ni are displayed. The absolute value is underestimated, consistent with the $B(E2)$ values discussed in Subsection 4.4. Nevertheless, the shape of the form factors, especially the position of the peaks and the dips are reproduced very well.

We can see the effect of the GQR state through the $E2$ effective charge for each single particle transition, as discussed in Appendix C. These j-dependent effective charges are shown in Table 15. It is seen that the j-dependent effective charges are actually insensitive to j. Moreover, comparing with the j-independent effective charges in Eq.(4.4) obtained by adjusting the $E2$ transition probabilities in ^{56}Fe, we have an excellent agreement for proton charges and a slight suppression for neutron charges. This implies that the core polarization effect is underestimated only slightly in both IS and IV modes. The influence of the $k > 2$ configurations within the pf-shell might be present. Note that the single particle matrix elements of r^2 obtained by the HF calculation is very similar to those in the harmonic oscillator approximation employed in Subsection 4.4. In practice, the ratio of the HF matrix elements to the harmonic oscillator ones are 0.93$\sim$1.05. The $B(E2)$ values by using the j-dependent effective charges are also shown in Tables 4$\sim$8 with the label 'Cal.(B)'. We confirm the overall agreement between the results calculated from the j-independent charges and those from the j-dependent charges. This fact justifies the usual j-independent effective charges for $E2$ transition.

The reproduction of the (e, e') data convinces us the validity of the shell model wavefunctions.

4.6 Proton Scattering Cross Sections

Recently $(\vec{p}, p')$ experiments are performed for ^{56}Fe and ^{54}Cr[32, 73], with the incident proton energy of $E_p = 65$MeV. The differential cross sections and the analyzing powers are measured. The data are analyzed in the distorted wave Born approximation (DWBA), by using the present shell model density matrices. This calculation is carried out by Takamatsu and his collaborators[32, 73]. We discuss their results in this subsection.

The Bonn-Jülich effective interaction[70] is employed as the interaction between the incident or scattered proton and the nucleons in the target nucleus. Although the M3Y interaction[71] and the Paris-Hamburg interaction[72] are also tried, the results were essentially the same. In order to reproduce the experimental data, an overall normalization factor is used for each transition. This factor would correspond to the core polarization effect. In fact, the adjusted values are compatible with the ones expected from the effective charges employed in the reproduction of the $B(E2)$ values, listed in Eq.(4.4).

As shown in Fig.16, the differential cross sections in ^{56}Fe are reproduced for the excitations to the 2_1^+, 2_2^+ and 2_4^+ states, with much better agreement than those calculated from the wavefunctions of Ref.[31]. The normalization factor with respect to the 2_1^+ state is understood as the core polarization effect by the following semi-quantitative estimation. The excitation from the 0_1^+ to the 2_1^+ state has isoscalar character. Indeed the transition matrix element of Q_π is almost the same as that of Q_ν in the present calculation, as shown in Table 4. Therefore the normalization factor is estimated by using Eq.(4.5),

$$\left|\frac{e_{IS} + \delta e_{IS}}{e_{IS}}\right|^2 = \left|\frac{0.5 + 0.65}{0.5}\right|^2 \sim 5.3. \tag{4.17}$$

This value is not so different from the adjusted value 4.3. The normalization factors with respect to the other 2^+ states are nearly equal to that for the 2_1^+ state.

The absolute value of the cross section in the excitation to the 2_3^+ state is smaller by an order of magnitude even than the 2_2^+ or the 2_4^+ states, in the experimental data. This is consistent with the present calculation, since the adjusted normalization factor is similar to the values adopted in the other 2^+ states. In addition, the excitation to the 2_3^+ state shows strikingly anomalous angular distribution. The present shell model wavefunctions reproduce this anomaly remarkably well, while the wavefunctions in Ref.[31] cannot[32].

The experimental differential cross sections[73] are also reproduced remarkably well in ^{54}Cr, by using slightly smaller normalization factors than in the case of ^{56}Fe. The results are shown in Fig.17.

These analyses of $(\vec{p},p')$ data also confirm further the validity of the present shell model wavefunctions.

5 Mixed-Symmetry States in ^{56}Fe

5.1 Decomposition into Extended SD-States

We shall search for a mixed-symmetry 2^+ state in ^{56}Fe by inspecting the shell model wavefunctions. ^{56}Fe is expected to be one of the simplest systems in order to study mixed-symmetry states, because both the proton and the neutron boson numbers are unity when we take $N = Z = 28$ to be magic number. This fact makes it easier to study the mixed-symmetry states even in the case that the ^{56}Ni core is relaxed. We recall the claim by Eid *et al.* that the 2_2^+ and 2_3^+ states share the mixed-symmetry 2^+ component based on the $B(M1)$ values to the 2_1^+ state, as mentioned in Section 3.

First we consider S- and D-pairs, which correspond to the s- and d-bosons in the IBM[5]. When we assume the ^{56}Ni inert core, which has $N = Z = 28$, ^{56}Fe has a pair of proton holes and a pair of valence neutrons. In the $k = 0$ configurations in Eq.(4.1), S- and D-pairs of protons are defined as the 0^+ and 2^+ states of the $(0f_{7/2})^{-2}$ configuration, while those of neutrons are collective 0^+ and 2^+ states of the $(0f_{5/2}1p_{3/2}1p_{1/2})^2$ configurations. If these three single particle orbits are degenerate, S_ν-pair is defined by Eq.(2.23), and D_ν-pair is typically given by Eq.(2.25). The complete set of states constructed by one proton pair and one neutron pair in the SD-subspace is spanned by

$$
\begin{aligned}
|0_S^+(S^2)\rangle &= |S_\pi\rangle \otimes |S_\nu\rangle, \\
|0_S^+(D^2)\rangle &= [|D_\pi\rangle \otimes |D_\nu\rangle]^{(0)}, \\
|1_M^+(D^2)\rangle &= [|D_\pi\rangle \otimes |D_\nu\rangle]^{(1)}, \\
|2_S^+(SD)\rangle &= \frac{1}{\sqrt{2}}(|D_\pi\rangle \otimes |S_\nu\rangle + |S_\pi\rangle \otimes |D_\nu\rangle), \\
|2_S^+(D^2)\rangle &= [|D_\pi\rangle \otimes |D_\nu\rangle]^{(2)},
\end{aligned}
$$

$$
\begin{aligned}
|2^+_M(SD)\rangle &= \frac{1}{\sqrt{2}}(|D_\pi\rangle\otimes|S_\nu\rangle - |S_\pi\rangle\otimes|D_\nu\rangle),\\
|3^+_M(D^2)\rangle &= [|D_\pi\rangle\otimes|D_\nu\rangle]^{(3)},\\
|4^+_S(D^2)\rangle &= [|D_\pi\rangle\otimes|D_\nu\rangle]^{(4)}. \qquad (5.1)
\end{aligned}
$$

The states with the subscript S correspond to the totally symmetric states in the IBM-2 after the boson mapping, whereas those with the subscript M to the mixed-symmetry state with $F = F_{max} - 1$. Obviously all the states have $T = 2$ in this $k = 0$ configuration space.

Recently Halse investigated the wavefunctions of Horie-Ogawa, determining the structure of the S_ν- and D_ν-pairs from the 0^+_1 and 2^+_1 states of ^{58}Ni[58]. Then it was found that the 0^+_1 and 2^+_1 states of ^{56}Fe are totally symmetric states in a good approximation. According to his investigation, the 0^+_1 state consists of $|0^+_S(S^2)\rangle$ by 72% and $|0^+_S(D^2)\rangle$ by 24%, while the 2^+_1 state of $|2^+_S(SD)\rangle$ by 75% and $|2^+_S(D^2)\rangle$ by 13%. It is also pointed out that the 2^+_2 has quite a large fraction ($\sim$ 80%) of the mixed-symmetry 2^+ component. However, the realistic wavefunctions obtained in the present calculation contain $k > 0$ configurations considerably. In order to take this effect into account, we introduce extended SD-pair states as explained below.

The wavefunctions of ^{56}Fe are expanded in terms of products of proton and neutron wavefunctions as

$$
|\Psi(\sigma)\rangle = \sum_{\sigma',\sigma''} c^{\sigma}_{\sigma',\sigma''}|\varphi_\pi(\sigma')\rangle\otimes|\varphi_\nu(\sigma'')\rangle, \qquad (5.2)
$$

where $c^{\sigma}_{\sigma',\sigma''}$ denotes expansion coefficients. The proton (neutron) basis $|\varphi_\pi(\sigma)\rangle$ ($|\varphi_\nu(\sigma)\rangle$) is taken from eigenstates of the Kuo-Brown hamiltonian in the corresponding single-closed nucleus on the ^{40}Ca core, in the $k \le 2$ configuration space for each system. By using the $|\varphi_\rho(\sigma)\rangle$ bases, we define the extended

SD-bases,

$$
|\tilde{S}_\rho\rangle = \sum_i x^{(0)}_{i,\rho}|\varphi_\rho(0^+_i)\rangle, \qquad (5.3)
$$

and

$$
|\tilde{D}_\rho\rangle = \sum_i x^{(2)}_{i,\rho}|\varphi_\rho(2^+_i)\rangle. \qquad (5.4)
$$

by an optimization described below. The coefficient $x^{(0)}_{i,\rho}$ is determined so that overlap between $|\tilde{S}_\pi\rangle\otimes|\tilde{S}_\nu\rangle$ and the ground state of ^{56}Fe should be maximum. After this procedure, $x^{(2)}_{i,\pi}$ is determined by maximizing overlap between $|\tilde{D}_\pi\rangle\otimes|\tilde{S}_\nu\rangle$ and the 2^+_1 state of ^{56}Fe. Likewise, $x^{(2)}_{i,\nu}$ is determined by overlap of $|\tilde{S}_\pi\rangle\otimes|\tilde{D}_\nu\rangle$. In these optimizations we used about twenty $|\varphi_\rho(J^+_i)\rangle$ bases for each $\rho(=\pi,\nu)$ and J, in order to confirm the convergence. The resultant $|\tilde{S}_\rho\rangle$ is established to be an almost pure $v = 0$ state; more than 95% both for $|\tilde{S}_\pi\rangle$ and for $|\tilde{S}_\nu\rangle$, where the seniority v is defined as the sum of the number of unpaired particles in each orbit. The importance of the pairing correlation in the smear of the ^{56}Ni core is clearly realized from this fact.

The direct products of the $\tilde{S}\tilde{D}$-bases do not necessarily stay in the $k \le 2$ configuration space nor conserve the isospin. Therefore we define the following extended SD-states,

$$
\begin{aligned}
|0^+_S(\tilde{S}^2)\rangle &= P_{T=2}P_{k\le2}|\tilde{S}_\pi\rangle\otimes|\tilde{S}_\nu\rangle,\\
|0^+_S(\tilde{D}^2)\rangle &= \mathcal{N}P_{\mathcal{O}\{0^+_S(\tilde{S}^2)\}}P_{T=2}P_{k\le2}[|\tilde{D}_\pi\rangle\otimes|\tilde{D}_\nu\rangle]^{(0)},\\
|1^+_M(\tilde{D}^2)\rangle &= \mathcal{N}P_{T=2}P_{k\le2}[|\tilde{D}_\pi\rangle\otimes|\tilde{D}_\nu\rangle]^{(1)},\\
|2^+_S(\tilde{S}\tilde{D})\rangle &= \mathcal{N}P_{T=2}P_{k\le2}\frac{1}{\sqrt{2}}(|\tilde{S}_\pi\rangle\otimes|\tilde{D}_\nu\rangle + |\tilde{D}_\pi\rangle\otimes|\tilde{S}_\nu\rangle),\\
|2^+_S(\tilde{D}^2)\rangle &= \mathcal{N}P_{\mathcal{O}\{2^+_S(\tilde{S}\tilde{D})\}}P_{T=2}P_{k\le2}[|\tilde{D}_\pi\rangle\otimes|\tilde{D}_\nu\rangle]^{(2)},\\
|2^+_M(\tilde{S}\tilde{D})\rangle &= \mathcal{N}P_{\mathcal{O}\{2^+_S(\tilde{S}\tilde{D}),2^+_S(\tilde{D}^2)\}}P_{T=2}P_{k\le2}\frac{1}{\sqrt{2}}(|\tilde{S}_\pi\rangle\otimes|\tilde{D}_\nu\rangle - |\tilde{D}_\pi\rangle\otimes|\tilde{S}_\nu\rangle),
\end{aligned}
$$

$$|3^+_M(\tilde{D}^2)\rangle = \mathcal{N} P_{T=2} P_{k\leq 2}[|\tilde{D}_\pi\rangle \otimes |\tilde{D}_\nu\rangle]^{(3)},$$
$$|4^+_S(\tilde{D}^2)\rangle = \mathcal{N} P_{T=2} P_{k\leq 2}[|\tilde{D}_\pi\rangle \otimes |\tilde{D}_\nu\rangle]^{(4)}. \quad (5.5)$$

Here $P_{k\leq 2}$ denotes the projection operator onto the $k \leq 2$ configuration space, P_T does the isospin projection operator and $P_{\mathcal{O}}$ represents the Schmidt orthogonalization to the states assigned by the curly bracket. This orthogonalization is similar to the seniority projection in the OAI mapping in concept[5]. The symbol $\mathcal{N}$ stands for an appropriate normalization constant for each state. This normalization is needed due to the influence of the projections. Though the projection $P_{\mathcal{O}} P_T P_k$ seems to break naive $\tilde{S}\tilde{D}$ picture, it changes the wavefunctions only by 6% at most. Thus the present procedures lead to a generalization of the OAI mapping[5], when we proceed to the correspondence between $\tilde{S}\tilde{D}$-states and *sd*-boson states. Although the shell model wavefunctions contain non-negligible $k > 0$ configurations. there is no result contradictory to $N_\pi = N_\nu = 1$, as is shown in the following discussions.

Table 16 shows overlaps between the $\tilde{S}\tilde{D}$-states defined in Eq.(5.5) and low-lying eigenstates of ^{56}Fe. The 0^+_1 is an almost pure $\tilde{S}\tilde{D}$-state. The 2^+_1 is primarily in the $\tilde{S}\tilde{D}$-subspace, and is totally symmetric distinctly. On the other hand, the 2^+_2 state has large amplitude of the $|2^+_M(\tilde{S}\tilde{D})\rangle$ component, while the overlaps with $|2^+_S(\tilde{S}\tilde{D})\rangle$ and $|2^+_S(\tilde{D}^2)\rangle$ are negligible. The situation is the same for the 2^+_4 state. On the other hand, the 2^+_3 state has very little $\tilde{S}\tilde{D}$ probability. About half of the mixed-symmetry 2^+ component is shared by the 2^+_2 and 2^+_4 states in ^{56}Fe, contrary to the previous report in Ref.[17]. The remaining half of the mixed-symmetry component seems to be highly fragmented over wide energy region or to go to much higher energy. The distribution of $|2^+_M(\tilde{S}\tilde{D})\rangle$ component up to 7MeV is displayed in the upper box

of Fig.18. There are twenty-five 2^+ states in $Ex < 7$MeV in the present calculation. The total probability of the $|2^+_M(\tilde{S}\tilde{D})\rangle$ component in $Ex < 7$MeV is 71%. Both of the 2^+_2 and the 2^+_4 states have $Ex \simeq 3$MeV. We can see that about 28% of the component is highly fragmented in $3.5 < Ex < 7$MeV, while 29% goes beyond 7MeV and should be treated by a renormalization procedure as will be discussed in Section 6. It is remarkable that, as far as the low-lying states are concerned, the present realistic interaction hardly mix the symmetric $\tilde{S}\tilde{D}$-components with the mixed-symmetry one, against the assumption in Ref.[17]. Judging from the lowest four 2^+ states, at least 44% of the mixed-symmetry 2^+ component is confirmed to be in existence separately from the symmetric components even through the realistic interaction. Investigation of this point in other nuclei is of interest.

The 2^+_3 is an entirely non-collective state. It is confirmed that about half of this state is represented as a product of $|\tilde{S}_\pi\rangle$ and a neutron non-collective 2^+ state orthogonal to $|\tilde{D}_\nu\rangle$.

The proton or neutron bases with $J^P = 4^+$, which would correspond to the *g*-boson degrees of freedom, are contained only by 10% in the 2^+_1 state as well as in the 2^+_3 state. This result seems to exclude the suggestion by Collins *et al.*[18] that the *g*-bosons is important to describe the $B(M1)$ values concerning the low-lying 2^+ states.

Next we turn to 1^+ states. As exhibited in Table 16, the ground state of ^{56}Fe contains considerable amount of the $|0^+_S(\tilde{D}^2)\rangle$ component. This implies that ^{56}Fe is somewhat deformed. Hence we can expect that the mixed-symmetry 1^+ state, $|1^+_M(\tilde{D}^2)\rangle$, exists in relatively low energy region. The overlaps between this component and the low-lying eigenstates of ^{56}Fe in the shell model are shown in Table 16. The distribution of this compo-

nent in the shell model space is displayed in the upper box of Fig.19, up to $Ex = 7$MeV. This $|1^+_M(\tilde{D}^2)\rangle$ component has 78% probability in $Ex < 7$MeV. We find that the 1^+_2 and 1^+_3 states, which are located very closely to each other with $Ex \simeq 3.5$MeV, share the main part of the mixed-symmetry component. The 1^+_2 state is experimentally established in a very good agreement with the present calculation with respect to the excitation energy as well as the $B(M1)$ to the 0^+_1 state, as shown in Fig.6 and Table 9. On the other hand, the 1^+_3 state has not observed in experiments yet, though the 1^+_3 has somewhat larger $B(M1)$ than the 1^+_2 in the present calculation. It is desirable to check our prediction of the 1^+_3 state.

5.2 $E2$ Transition Properties

Here we look into the $E2$ matrix elements shown in Table 4. The matrix element of Q_π from the 2^+_1 to the 0^+_1 is quite large and almost equal to that of Q_ν. In addition, the expectation values of Q_π and Q_ν in the 2^+_1 state are close to each other. These facts are consistent with the result of the $\tilde{S}\tilde{D}$-decomposition, which reveals that both the 0^+_1 and 2^+_1 states are symmetric collective states.

A notable feature of the split of the mixed-symmetry 2^+ component is the cancellation between the mixed-symmetry component and non-collective degrees of freedom in the $E2$ matrix elements. The 2^+_2 state has small matrix element of Q_π with the ground state, while matrix element of Q_ν is large. As for the transition from the 2^+_4 to the 0^+_1 state, matrix element of Q_π is large while that of Q_ν is small. The coupling to non-collective degrees of freedom, which describe the states orthogonal to all the $\tilde{S}\tilde{D}$-states, causes the remarkable decrease of Q_π matrix element in the 2^+_2 state as well as that of

Q_ν in the 2^+_4. The collectivity defined from the 2^+_1 state does not necessarily exhaust the $E2$ transition probability even in the $0\hbar\omega$ space, because of the shell structure of the system. As a result of the large Q_π matrix element, $B(E2; 2^+_4 \to 0^+_1)$ is fairly large.

From the experimental data as well as from the calculated results in Fig.10, we see that the excitation to the 2^+_4 state has quite a high peak in the form factor. Such a high peak has not been observed in neither the 2^+_2 nor 2^+_3 state, consistently with the $B(E2)$ values. On the other hand, in the $(\vec{p}, \vec{p}')$ differential cross sections displayed in Fig.16, the absolute values in the 2^+_2 and 2^+_4 states are not so different from each other, and much higher than that in the 2^+_3 state. These experimental facts clarifies the character of the states; the large proton contribution with respect to the 2^+_4 state, the large neutron contribution with respect to the 2^+_2 state, and the non-collectivity of the 2^+_3 state. This consequence is thoroughly consistent with the preceding discussions based on the shell model calculation. The anomalous angular distribution in the $(\vec{p}, \vec{p}')$ cross section of the excitation to the 2^+_3 state must arise from the non-collectivity of this state. The discrepancy in the $C2$ form factor in this state between the calculation and the experiments would also be caused by the non-collectivity. This form factor results from cancellation among various single particle contributions.

The contribution of proton and neutron degrees of freedom is also realized in the comparison between the solid and dotted lines in Fig.10. The dotted lines are obtained only from the proton wavefunctions without the core polarization effect. The core polarization effect increases the transition strength, and moves the positions of peaks and dips to the direction of smaller q, in general. According to the estimation from the effective charge

of Eq.(4.4), the form factor will overall increase by about factor of 5 for the isoscalar transition, due to the core polarization. The calculated form factors of the excitation to the 2_1^+ state is consistent with this estimation. For an excitation dominated by protons like the one to the 2_4^+ state, the increase in the form factor will be smaller, about factor of 2. On the other hand, the neutron wavefunctions in the shell model space are reflected only through the core polarization effect. The form factor with respect to the 2_2^+ state is extremely affected by the core polarization; notable shape change occurs in the form factor.

Fig.11 displays the transition density from the 0_1^+ to some 2^+ states, the equivalent information to the form factor shown in Fig.10 besides the corrections of the center of mass motion and the nucleon finite size effect. The proton and neutron contributions are displayed as well as the total transition density for the 2_1^+ state. The difference in the height of the peak between proton and neutron transition densities is related to the difference in the effective charge. The displacement between proton peak and neutron one in the transition density is too small for a node to appear. Even if the sign of the neutron density becomes opposite, which is expected for the pure mixed-symmetry 2^+ state, only the quenching of the peak will come out. Therefore the form factor cannot be a decisive probe for the mixed-symmetry 2^+ state, because not only of the coupling to non-collective degrees of freedom, but also of the absence of characteristic r-dependence. Although there appear some nodes in the transition densities with respect to the 2_2^+ and 2_4^+ states, single particle structure gives rise to the nodes. The three typical single particle transition densities are exhibited in Fig.12. A node can appear if the transition is predominantly contributed by the single particle transition from

an f-orbit to a p-orbit, or includes both the transition within the f-orbits and that within the p-orbits but with the opposite sign.

5.3 Investigation by $(J_\pi - J_\nu)$ Operator

The J_π and J_ν operators, where

$$J_\rho = L_\rho + S_\rho, \quad (\rho = \pi, \nu) \tag{5.6}$$

are alternative devices to discuss the proton-neutron symmetry, since J_π and J_ν vary neither proton part nor neutron part of wavefunctions. We easily obtain for the SD-states in Eq.(5.1),

$$\begin{aligned}&\langle 2_S^+(SD)\|J_\pi\|2_S^+(SD)\rangle = \langle 2_S^+(SD)\|J_\nu\|2_S^+(SD)\rangle \\ &= \langle 2_S^+(SD)\|J_\pi\|2_M^+(SD)\rangle = -\langle 2_S^+(SD)\|J_\nu\|2_M^+(SD)\rangle = \frac{\sqrt{30}}{2} \simeq 2.74,\end{aligned} \tag{5.7}$$

$$\begin{aligned}&\langle 2_S^+(SD)\|J_\pi\|2_S^+(D^2)\rangle = \langle 2_S^+(SD)\|J_\nu\|2_S^+(D^2)\rangle \\ &= \langle 2_M^+(SD)\|J_\nu\|2_S^+(D^2)\rangle = \langle 2_M^+(SD)\|J_\nu\|2_S^+(D^2)\rangle = 0.\end{aligned} \tag{5.8}$$

The replacement of the SD-states by the $\tilde{S}\tilde{D}$-ones defined in Eq.(5.5) does not affect the results, apart from the slight change resulting from the projections in Eq.(5.5). Therefore the mixed-symmetry 2^+ state should have large matrix element of J_π and J_ν to the 2_1^+ state, as far as the 2_1^+ is totally symmetric.

Table 9 displays reduced matrix elements of L_π, S_π, L_ν and S_ν. We see that expectation values of J_π and J_ν in the 2_1^+ state are almost the same, consistent with the symmetric nature of the state. Table 9 shows that the 2_2^+ and 2_4^+ states have matrix elements to the 2_1^+ comparable to the value

of Eq.(5.7), whereas the 2_3^+ has negligibly small one. This consequence is consistent with the conclusion by the $\tilde{S}\tilde{D}$-decomposition. Remark that all the matrix elements of S_π and S_ν are quite small. The dominance of L_π and L_ν between the collective states, the 2_1^+, 2_2^+ and 2_4^+ states in this case, agrees with our expectation mentioned in Section 2.

The above consideration leads us to the idea of the investigation of the mixed-symmetry 2^+ component based on the $(J_\pi - J_\nu)$ operator. The $(J_\pi - J_\nu)$ can be regarded as collective $M1$ transition operator, in analogy to the IBM-2 (see Eq.(2.35)). Let us consider the state which exhaust the sum rule of the collective $M1$ transition in the $J = 2, T = 2$ space,

$$|2^+_{MSR}\rangle = \mathcal{N} P_{\mathcal{O}\{2_1^+\}} P_{T=2} P_{J=2} (J_\pi - J_\nu)|2_1^+\rangle. \tag{5.9}$$

Here P_J and P_T are angular momentum and isospin projection operators, respectively, while $P_\mathcal{O}$ orthogonalize the state to the 2_1^+. $\mathcal{N}$ stands for an appropriate normalization constant. The subscript MSR expresses that the state corresponds to the mixed-symmetry 2^+ state which exhausts the sum rule of the collective $M1$ transition probabilities from the 2_1^+ state. It has been pointed out that a collective $M1$ transition is possible to split due to the isospin, when active orbits are common between protons and neutrons[23]. Nevertheless the P_T varies the wavefunction only by 10% in the present case, on account of the difference in the occupation of the $0f_{7/2}$ orbit between valence protons and neutrons. The distribution of the $|2^+_{MSR}\rangle$ component in the eigenstates of ^{56}Fe is shown in Table 17 and the lower box of Fig.18. About 50% of the $|2^+_{MSR}\rangle$ component is shared by the 2_2^+ and 2_4^+ states. It is found out from Fig.18 that the distribution of the $|2^+_{MSR}\rangle$ component resembles that of $|2^+_M(\tilde{S}\tilde{D})\rangle$ in $Ex < 5$MeV, while both of them are highly

fragmented in $5 < Ex < 7$MeV with some difference from each other. This difference occurs due to the effect of J_π (J_ν) which enhance the component with higher values of proton (neutron) angular momentum. The overlap between the $|2^+_{MSR}\rangle$ and $|2^+_M(\tilde{S}\tilde{D})\rangle$ states is about 40%. However, it should be emphasized that the distribution shown in the lower box of Fig.18 is in qualitative agreement with that shown in the upper box. This fact suggests that the difference mainly appears in $Ex > 7$MeV, beyond the energy region that we are interested in. Therefore we can discuss the mixed-symmetry by using the $|2^+_{MSR}\rangle$ state, which is much easier to construct than the $|2^+_M(\tilde{S}\tilde{D})\rangle$ state.

We can carry out a similar investigation for the mixed-symmetry 1^+ state, since the ground state contain a certain amount of the $|0^+_S(\tilde{D}^2)\rangle$ component. In this case, we use the following state

$$|1^+_{MSR}\rangle = \mathcal{N} P_{T=2} (J_\pi - J_\nu)|0_1^+\rangle. \tag{5.10}$$

From another point of view, this $|1^+_{MSR}\rangle$ state is a general definition of the scissors state[74]. The distribution of the $|1^+_{MSR}\rangle$ state is shown in Table 17 and Fig.19. A good qualitative agreement is established between the distribution of $|1^+_M(\tilde{D}^2)\rangle$ and that of $|1^+_{MSR}\rangle$.

6 Renormalization of Extended SD-States

In this section we consider the correspondence between the shell model states and the collective states to be described in the IBM, in more detail. For this purpose we introduce two renormalization methods. One is a perturbative method discussed in Subsection 6.1. Though this method works well in ^{56}Fe, a part of the success is owing to an accidental cancellation. The other method, which is called diagonalized-block renormalization (DBR) in this thesis, is free from this problem. It is introduced in Subsection 6.2 and applied to ^{56}Fe in Subsection 6.3. We derive the IBM hamiltonian from the DBR results in ^{56}Fe.

6.1 Perturbative Renormalization

Feshbach's projection method[75], reviewed in Appendix D, is well-known as a method of renormalizing truncation effects. We define the P-space as the $\tilde{S}\tilde{D}$-space of ^{56}Fe, which is given in Eq.(5.5). The total space corresponds to the shell model space with $k \leq 2$ configurations, while the original hamiltonian is the Kuo-Brown hamiltonian. The eigenstates of the H_{PP} is computed by the diagonalization, where the H_{PP} is defined in Eq.(D.7). The 1^+, 3^+ and 4^+ states are unique, whereas the amplitudes of the 0^+ and 2^+ states are determined by the diagonalization. The resultant energy levels are displayed in the left column of Fig.20, with the label 'unren.', compared with the eigenenergies in the shell model calculation displayed in the right column. In Fig.20, the origin of the energy levels is set to the shell model ground state. Though large amounts of the wavefunction of the 0_1^+ and 2_1^+ states stay in the $\tilde{S}\tilde{D}$-space as shown in Section 5, the energies of the 0_1^+ and 2_1^+ states in

the $\tilde{S}\tilde{D}$-space are too high. This fact indicates that H_{PP} is insufficient to reproduce physical quantities like energies, and that the influence of states outside the $\tilde{S}\tilde{D}$-space should not be ignored. We shall take into account the effects of the Q-space.

In the Feshbach's projection method, the renormalized hamiltonian is given by Eq.(D.9). Though Eq.(D.9) gives an exact way to incorporate the influence of the Q-space into the hamiltonian, it is difficult and not advantageous to handle without any approximation in most cases. Concretely, if one would like to know exact eigenenergies, he must treat H_{QQ} exactly which is often a matrix with enormous dimension. Moreover, he must solve a non-linear coupled equation, since the eigenenergy is also contained in the denominator of the second term. However, Eq.(D.9) has similar form to the perturbative expansion up to the second order. In fact, as far as the P-space is chosen appropriately, the second term on the right-hand side of Eq.(D.9) is sufficiently smaller than the first term. In this subsection the Feshbach's method is utilized in a perturbative sense.

An eigenstate of the H_{PP} is expressed by $|p_a\rangle$, where the subscript a is the index to distinguish the eigenstates. Remember that, in the following, when we use the subscript a or a' as an index, we handle the state in the representation so as for H_{PP} to be diagonal. The energy expectation value of the state $|\varphi\rangle$ is represented as $E(\varphi)$, namely,

$$E(\varphi) = \langle\varphi|H|\varphi\rangle. \tag{6.1}$$

The $|p_a\rangle$ satisfies the relation,

$$H_{PP}|p_a\rangle = E(p_a)|p_a\rangle, \quad P|p_a\rangle = |p_a\rangle. \tag{6.2}$$

Next we consider the state

$$|q_a\rangle = \mathcal{N}\hat{Q}H|p_a\rangle, \tag{6.3}$$

where the normalization constant $\mathcal{N}$ is given as

$$\mathcal{N}^2\langle p_a|H\hat{Q}H|p_a\rangle = 1. \tag{6.4}$$

The energy denominator $(E - H_{QQ})$ in Eq.(D.9) is approximated by a c-number $[E(p_a) - E(q_a)]$. Note that the $E(q_a)$ is rewritten as

$$\begin{aligned} E(q_a) &= \langle q_a|H|q_a\rangle \\ &= \frac{\langle p_a|H\hat{Q}H\hat{Q}H|p_a\rangle}{\langle p_a|H\hat{Q}H|p_a\rangle}. \end{aligned} \tag{6.5}$$

For the off-diagonal elements with the initial state $|p_a\rangle$ and the final state $|p_{a'}\rangle$, the energy denominator is approximated by the arithmetic average

$$\frac{1}{2}\{[E(p_a) - E(q_a)] + [E(p_{a'}) - E(q_{a'})]\}, \tag{6.6}$$

in order to maintain the hermiticity of the hamiltonian. Consequently the matrix element of $\tilde{H}_{PP}$ is approximated by

$$\begin{aligned} & \langle p_{a'}|\tilde{H}_{PP}|p_a\rangle \\ \simeq\ & \langle p_{a'}|H'_c|p_a\rangle \\ \equiv\ & \langle p_{a'}|H|p_a\rangle + \langle p_{a'}|H|q_{a'}\rangle \frac{\langle q_{a'}|q_a\rangle}{\frac{1}{2}\{[E(p_a) - E(q_a)] + [E(p_{a'}) - E(q_{a'})]\}} \langle q_a|H|p_a\rangle. \end{aligned} \tag{6.7}$$

This is a kind of closure approximation, since it is attained by the replacement of the energy denominator by an appropriate c-number. The off-diagonal

elements are negligible because the overlaps $\langle q_{a'}|q_a\rangle$ are small. The $|\langle q_{a'}|q_a\rangle|^2$ is at most 2% in the present case. It is noticed that $\langle p_{a'}|H|p_a\rangle = 0$ for $a \neq a'$.

The eigenenergies of the renormalized hamiltonian H'_c is shown in the second left column of Fig.20. The energy of the lowest 0^+ and 2^+ states are in remarkable agreement with the corresponding shell model states.

We take an energy average of the 4^+ shell model states in $Ex < 6$MeV, with the weights proportional to the squares of the overlaps of the $|4^+_S(\tilde{D}^2)\rangle$ component. Since we have only a single 4^+ state in the $\tilde{S}\tilde{D}$-space, this $\tilde{S}\tilde{D}$-weighted average directly corresponds to the energy of the collective 4^+ state. It is remarked that, as for the 0^+ states, the amplitudes in the $\tilde{S}\tilde{D}$-space have to be considered if one would like to compare an $\tilde{S}\tilde{D}$-weighted average of the shell model states with the collective states, since there are two 0^+ states in the $\tilde{S}\tilde{D}$-space. The averaged energies with respect to the $|2^+_M(\tilde{S}\tilde{D})\rangle$ and $|1^+_M(\tilde{D}^2)\rangle$ components are calculated in a similar way. Because of the same reason as the case of the 4^+ states, the $\tilde{S}\tilde{D}$-weighted average of the 1^+ states is to be compared with the collective 1^+ state. The $|2^+_M(\tilde{S}\tilde{D})\rangle$ state hardly mixes with the other states in the $\tilde{S}\tilde{D}$-space, as will be shown later. Therefore the $\tilde{S}\tilde{D}$-weighted average with respect to the $|2^+_M(\tilde{S}\tilde{D})\rangle$ component also corresponds to the second 2^+ state in the collective levels. Those $\tilde{S}\tilde{D}$-weighted averages are displayed in the second right column of Fig.20. The enlargement of the energy range to $Ex < 7$MeV is confirmed to influence very little for the $|2^+_M(\tilde{S}\tilde{D})\rangle$ and $|1^+_M(\tilde{D}^2)\rangle$ components. The increase of the averaged energy is 0.04MeV for the $|2^+_M(\tilde{S}\tilde{D})\rangle$ component, and is 0.01MeV for the $|1^+_M(\tilde{D}^2)\rangle$ component. In the right column, the shell model states are exhibited. Some of the shell model states, which contain $\tilde{S}\tilde{D}$-space probability by more than 10%, are connected by the short-dashed

lines in the figure.

Though the perturbative renormalization works well within the closure approximation, this success partly owes to an accidental situation. Hereafter we restrict ourselves to the diagonal elements, since the wavefunctions in the $\tilde{S}\tilde{D}$-space scarcely change by the renormalization. The renormalization adopted above includes two kinds of approximations. One is the replacement of the exact eigenenergy E by $E(p_a)$, which leads to an underestimate of the energy denominator for low-lying states. The other approximation is the replacement of H_{QQ} by a single number $E(q_a)$. This leads to a tendency of an overestimate of the second term of Eq.(D.9), as discussed later.

The error caused by the former approximation is evaluated by the factor

$$\frac{E(p_a) - E(q_a)}{E - E(q_a)}. \tag{6.8}$$

This factor is usually less than unity, as far as the resultant energy becomes lower by the perturbation. This is true in the present case, since the $\tilde{S}\tilde{D}$-states are energetically favored in comparison with the states in the Q-space.

Next we see how the distribution of $|q_a\rangle$ over the eigenstates of H_{QQ} affects the renormalized energy. For the exact treatment of H_{QQ}, the eigenenergy of H_{QQ} should be calculated. Let an eigenstate of H_{QQ} be denoted by $|\bar{q}_i\rangle$. Then the second term on the right-hand side of Eq.(D.9) is rewritten as

$$\sum_i H_{PQ}|\bar{q}_i\rangle \frac{1}{E - E(\bar{q}_i)} \langle \bar{q}_i | H_{QP}. \tag{6.9}$$

The state $|q_a\rangle$ is expanded by the eigenstates,

$$|q_a\rangle = \sum_i x_{i,a}|\bar{q}_i\rangle, \tag{6.10}$$

where

$$x_{i,a} = \frac{\langle \bar{q}_i|H|p_a\rangle}{\sqrt{\sum_{i'}|\langle \bar{q}_{i'}|H|p_a\rangle|^2}} = \frac{\langle \bar{q}_i|H|p_a\rangle}{\sqrt{\langle p_a|H\hat{Q}H|p_a\rangle}}. \tag{6.11}$$

We consider the expansion in the parameter

$$\lambda_{i,a} = \frac{E(q_a) - E(\bar{q}_i)}{E - E(q_a)}, \tag{6.12}$$

in order to evaluate the error coming from the approximation by $E(q_a)$. For the second term of Eq.(D.9), we have

$$\begin{aligned}
&\langle p_a|H_{PQ}\frac{1}{E - H_{QQ}}H_{QP}|p_a\rangle \\
&= \sum_i \langle p_a|H|\bar{q}_i\rangle \frac{1}{[E - E(q_a)](1 + \lambda_{i,a})}\langle \bar{q}_i|H|p_a\rangle \\
&= \sum_i \langle p_a|H|\bar{q}_i\rangle \frac{1}{E - E(q_a)}[1 - \lambda_{i,a} + \lambda_{i,a}^2 + O(\lambda^3)]\langle \bar{q}_i|H|p_a\rangle \\
&= \frac{1}{E - E(q_a)}\langle p_a|H\hat{Q}H|p_a\rangle - \frac{1}{E - E(q_a)}\sum_i \langle p_a|H|\bar{q}_i\rangle\lambda_{i,a}\langle \bar{q}_i|H|p_a\rangle \\
&\quad + \frac{1}{E - E(q_a)}\sum_i \langle p_a|H|\bar{q}_i\rangle\lambda_{i,a}^2\langle \bar{q}_i|H|p_a\rangle + O(\lambda^3).
\end{aligned} \tag{6.13}$$

The first term of the above equation is already taken into account in the closure approximation, beside the difference between E and $E(p_a)$. The second term vanishes because, by using Eq.(6.5),

$$\begin{aligned}
&\sum_i \langle p_a|H|\bar{q}_i\rangle\lambda_{i,a}\langle \bar{q}_i|H|p_a\rangle \\
&= \frac{1}{E - E(q_a)}\sum_i \langle p_a|H|\bar{q}_i\rangle[E(q_a) - \langle \bar{q}_i|H|\bar{q}_i\rangle]\langle \bar{q}_i|H|p_a\rangle \\
&= \frac{1}{E - E(q_a)}[E(q_a)\langle p_a|H\hat{Q}H|p_a\rangle - \langle p_a|H\hat{Q}H\hat{Q}H|p_a\rangle] \\
&= 0.
\end{aligned} \tag{6.14}$$

Therefore the main correction is acquired from the third term,

$$\begin{aligned}
&\sum_i \langle p_a|H|\bar{q}_i\rangle \lambda_{i,a}^2 \langle \bar{q}_i|H|p_a\rangle \\
&= \frac{1}{[E-E(q_a)]^2}\sum_i \langle p_a|H|\bar{q}_i\rangle [E(q_a)-\langle \bar{q}_i|H|\bar{q}_i\rangle]^2 \langle \bar{q}_i|H|p_a\rangle \\
&= \frac{1}{[E-E(q_a)]^2}[\langle p_a|H\hat{Q}H\hat{Q}H\hat{Q}H|p_a\rangle - E(q_a)\langle p_a|H\hat{Q}H\hat{Q}H|p_a\rangle] \\
&= \frac{1}{[E-E(q_a)]^2}|\langle p_a|H|q_a\rangle|^2[\sigma_{q_a}(H_{QQ})]^2. \qquad (6.15)
\end{aligned}$$

Here the quantity

$$[\sigma_{q_a}(H_{QQ})]^2 = \langle q_a|H_{QQ}^2|q_a\rangle - [E(q_a)]^2 \qquad (6.16)$$

represents the variance of H_{QQ} in the state $|q_a\rangle$.

Eq.(6.15) gives a correction factor to the first term of Eq.(6.13),

$$1+\left[\frac{\sigma_{q_a}(H_{QQ})}{E-E(q_a)}\right]^2, \qquad (6.17)$$

which always exceeds unity. Eq.(6.13) is rewritten as

$$\begin{aligned}
&\langle p_a|H_{PQ}\frac{1}{E-H_{QQ}}H_{QP}|p_a\rangle \\
&= \frac{1}{E-E(q_a)}\langle p_a|H\hat{Q}H|p_a\rangle\left\{1+\left[\frac{\sigma_{q_a}(H_{QQ})}{E-E(q_a)}\right]^2\right\}+O(\lambda^3). \qquad (6.18)
\end{aligned}$$

Thus the distribution of $|q_a\rangle$ over the eigenstates of H_{QQ} generally enhances the effect of the renormalization.

Eq.(6.13) is rewritten by using the correction factors of Eqs.(6.8) and (6.17) as

$$\begin{aligned}
&\langle p_a|H_{PQ}\frac{1}{E-H_{QQ}}H_{QP}|p_a\rangle \\
&= \frac{1}{E-E(q_a)}\langle p_a|H\hat{Q}H|p_a\rangle\left\{1+\left[\frac{\sigma_{q_a}(H_{QQ})}{E-E(q_a)}\right]^2\right\}+O(\lambda^3) \\
&= \frac{1}{E(p_a)-E(q_a)}\langle p_a|H\hat{Q}H|p_a\rangle\left[\frac{E(p_a)-E(q_a)}{E-E(q_a)}\right]\left\{1+\left[\frac{\sigma_{q_a}(H_{QQ})}{E-E(q_a)}\right]^2\right\}+O(\lambda^3). \qquad (6.19)
\end{aligned}$$

The correction factor of Eq.(6.8) is compensated by the factor of (6.17) to a certain extent, in general.

The extremely good cancellation occurs in the present case, whereas one should not expect it in general cases. In practice, energy corrections due to the factor of Eq.(6.17) are $0.2 \sim 0.7$MeV and not necessarily negligible. In the next subsection we consider another renormalization method which is alternative and explicitly includes the effects relating to Eqs.(6.8) and (6.17).

6.2 Diagonalized-Block Renormalization

We shall incorporate the effects of the non-$\tilde{S}\tilde{D}$-states by the method which is called diagonalized-block renormalization (DBR) in this thesis. In this subsection we formulate the DBR.

We denote the bases in the P-space by

$$|p_\alpha\rangle, \quad (\alpha = 1, \cdots l), \qquad (6.20)$$

where l stands for the number of the bases with a definite spin-parity. In practice, we take for the 0^+ states as

$$|p_1\rangle = |0_S^+(\tilde{S}^2)\rangle, \quad |p_2\rangle = |0_S^+(\tilde{D}^2)\rangle, \qquad (6.21)$$

and for the 2^+ states as

$$|p_1\rangle = |2_S^+(\tilde{S}\tilde{D})\rangle, \quad |p_2\rangle = |2_S^+(\tilde{D}^2)\rangle, \quad |p_3\rangle = |2_M^+(\tilde{S}\tilde{D})\rangle. \qquad (6.22)$$

We use the subscript α or α' as an index of a basis state in the P-space. Take a notice on the difference of $|p_\alpha\rangle$ from $|p_a\rangle$ defined in the preceding subsection. For an appropriate integer n, we prepare the bases

$$
\begin{aligned}
&|p_1\rangle,\ |p_2\rangle,\ \cdots,\ |p_l\rangle,\\
&|q_1^{(1)}\rangle = \mathcal{N} P_{\mathcal{O}} H |p_1\rangle,\ \cdots,\ |q_l^{(1)}\rangle = \mathcal{N} P_{\mathcal{O}} H |p_l\rangle,\\
&|q_1^{(2)}\rangle = \mathcal{N} P_{\mathcal{O}} H |q_1^{(1)}\rangle,\ \cdots,\ |q_l^{(2)}\rangle = \mathcal{N} P_{\mathcal{O}} H |q_l^{(1)}\rangle,\\
&\qquad\cdots\cdots,\\
&|q_1^{(n)}\rangle = \mathcal{N} P_{\mathcal{O}} H |q_1^{(n-1)}\rangle,\ \cdots,\ |q_l^{(n)}\rangle = \mathcal{N} P_{\mathcal{O}} H |q_l^{(n-1)}\rangle. \qquad (6.23)
\end{aligned}
$$

$P_{\mathcal{O}}$ stands for the Schmidt orthogonalization, which is performed for the states according to the order presented in Eq.(6.23). $\mathcal{N}$ represents an appropriate normalization constant for each basis. It is remarked that, in the present case, the orthogonalization among the $|q_\alpha^{(1)}\rangle$ states influences the wavefunctions very little; by 2% at most. This fact implies

$$\langle p_\alpha | H \hat{Q} H | p_{\alpha'} \rangle \simeq 0, \qquad (\text{for } \alpha \neq \alpha') \qquad (6.24)$$

compared with the normalization constant like $\langle p_\alpha | H^2 | p_\alpha \rangle$. Note that $|q_\alpha^{(n)}\rangle$ is obtained from $H^n |p_\alpha\rangle$. Then we pick up a block matrix of the hamiltonian among the bases

$$|p_\alpha\rangle,\ |q_\alpha^{(1)}\rangle,\ \cdots,\ |q_\alpha^{(n)}\rangle, \qquad (6.25)$$

for each α ($\alpha = 1, 2, \cdots, l$). Diagonalizing each block, the state with the largest amplitude of $|p_\alpha\rangle$ is regarded as the renormalized basis $|\tilde{p}_\alpha^{(n)}\rangle$. We call this procedure n-th order renormalization. It should be remarked that each block of the hamiltonian is a tridiagonal matrix with $(n+1)$ dimension. A renormalized operator is obtained by taking the matrix elements of

the operator between the renormalized states. The n-th order renormalized hamiltonian thus obtained is denoted by $H_c^{(n)}$. The $H_c^{(0)}$ represents the unrenormalized hamiltonian, which is nothing but H_{PP}. The n-th order energy levels are given by diagonalizing the hamiltonian $H_c^{(n)}$.

We discuss some general features of the DBR method. Both the diagonalization of the block matrices and that of $H_c^{(n)}$ are unitary transformations. In those processes two types of couplings are neglected. One is the coupling to $|q_\alpha^{(n)}\rangle$ with larger n, which can be incorporated by going to higher order of the DBR. As far as the original bases are properly chosen, the convergence will be fast against enlarging the block. This is because $|q_\alpha^{(n)}\rangle$ ($n \geq 2$) does not couple to $|p_\alpha\rangle$ by H directly. The power of H through which $|q_\alpha^{(n)}\rangle$ couples to $|p_\alpha\rangle$ is at least n. In this sense, the influence of the $|q_\alpha^{(n)}\rangle$ ($n \geq 2$) states is regarded as an effective change of the energy of $|q_\alpha^{(1)}\rangle$. This effective change of the energy can be interpreted as an effect of the distribution of the $|q_\alpha^{(1)}\rangle$ state over the eigenstates of H_{QQ}, as will be illustrated in the following paragraphs.

In the present method we neglect the couplings among the renormalized collective basis and the non-collective states belonging to different blocks, even when we take sufficiently large block for each basis. In the case that the couplings are negligible, the n-th order levels are almost the same as those calculated by the diagonalization in the $l(n+1)$ dimensional space, which is spanned by the bases of Eq.(6.23). Otherwise the correspondence between the truncated bases and the exact states breaks down to some extent.

When there is a fragmentation of a basis which is caused by the coupling to a $|q_\alpha^{(n)}\rangle$ state belonging to the same block, we can pursue it by monitoring their mixing amplitudes. It is noted that, for the yrast states, the DBR

method never leads to energies lower than the diagonalization in the full space.

In the next subsection we shall apply the DBR to ^{56}Fe, and present the renormalized boson hamiltonian obtained by the DBR. Before going to the application, we shall comment, in the rest of this subsection, on the relation between the DBR and the perturbative treatment of the Feshbach's method.

We consider the state

$$|q_\alpha\rangle = \frac{1}{\sqrt{\langle p_\alpha|H\hat{Q}H|p_\alpha\rangle}}\hat{Q}H|p_\alpha\rangle. \tag{6.26}$$

Because of Eq.(6.24), we have

$$\langle p_\alpha|H|q_{\alpha'}\rangle \simeq 0, \quad (\text{for } \alpha \neq \alpha') \tag{6.27}$$

which is equivalent to

$$\langle q_\alpha|q_{\alpha'}\rangle \simeq 0, \quad (\text{for } \alpha \neq \alpha') \tag{6.28}$$

and therefore

$$|q_\alpha\rangle \simeq |q_\alpha^{(1)}\rangle, \tag{6.29}$$

in the actual case of ^{56}Fe. The set $\{|p_\alpha\rangle\}$ is connected with $\{|p_a\rangle\}$, which is an eigenstate of H_{PP} as mentioned in the preceding subsection, by a unitary transformation within the P-space. We distinguish them by the subscripts. If Eq.(6.28) is satisfied, $\{|q_\alpha\rangle\}$ is approximately connected with $\{|q_a\rangle\}$ by a unitary transformation within the Q-space.

Roughly speaking, the first order DBR has similar aspects to the closure approximation in the preceding subsection, since it incorporates the contribution of $\langle q_a|H|q_a\rangle$. The second order DBR takes into account the contribution

of $\sigma_{q_a}(H_{QQ})$, originated from $\langle q_a|H^2|q_a\rangle$. We discuss these correspondences below.

For the diagonal element, the first order DBR gives the energy correction to the energy expectation value of the collective basis as

$$\frac{|\langle p_\alpha|H|q_\alpha^{(1)}\rangle|^2}{E(\tilde{p}_\alpha^{(1)}) - E(q_\alpha^{(1)})} \simeq \frac{|\langle p_\alpha|H|q_\alpha\rangle|^2}{E(\tilde{p}_\alpha^{(1)}) - E(q_\alpha)}. \tag{6.30}$$

Suppose that we start from the $|p_a\rangle$ bases, the $|q_a^{(1)}\rangle$ state is obtained from $H|p_a\rangle$. We can build the $|\tilde{p}_a^{(1)}\rangle$ basis by diagonalizing the block hamiltonian which acts on the space spanned by $|p_a\rangle$ and $|q_a^{(1)}\rangle$, similarly to the procedure discussed so far. By replacing the subscript α by a in Eq.(6.30), we obtain the formula of the energy correction to the $|\tilde{p}_a^{(1)}\rangle$ basis;

$$\frac{|\langle p_a|H|q_a^{(1)}\rangle|^2}{E(\tilde{p}_a^{(1)}) - E(q_a^{(1)})} \simeq \frac{|\langle p_a|H|q_a\rangle|^2}{E(\tilde{p}_a^{(1)}) - E(q_a)}. \tag{6.31}$$

This is the same as the second term on the right-hand side of Eq.(6.7), except for the energy denominator. $[E(\tilde{p}_a^{(1)}) - E(q_a)]$ appears as the energy denominator in this case, while $[E(p_a) - E(q_a)]$ is employed in Eq.(6.7). Since $E(\tilde{p}_a^{(1)})$ is calculated by the diagonalization, Eq.(6.31) gives smaller renormalization effect than Eq.(6.7). As far as the neglected couplings between the different blocks are sufficiently small, namely the DBR works well, the transformation from $|p_\alpha\rangle$ to $|p_a\rangle$ does not influence this relationship.

In the $|p_a\rangle$ bases, the off-diagonal matrix elements of $H_c^{(0)}$ vanish. Similarly to Eq.(6.27), we have $\langle p_a|H|q_{a'}\rangle \simeq 0$ in the actual case of ^{56}Fe. Furthermore, $\langle q_a|H|q_{a'}\rangle$ is also small in the ^{56}Fe case. Then, together with the fact that the mixing amplitudes of $|q_a\rangle$ are small, the off-diagonal terms of $H_c^{(1)}$ are expected to be quite small. This situation leads that the $|\tilde{p}_a^{(n)}\rangle$ states are

kept to be approximate eigenstates of $H_c^{(n)}$, independently of the order of the renormalization n.

In the second order DBR, the mixing amplitude of $|q_\alpha^{(2)}\rangle$ is usually small, since it does not couple to $|p_\alpha\rangle$ via H directly. Indeed the mixing probabilities are less than 10% in all the $|\tilde{p}_\alpha^{(2)}\rangle$ bases of ^{56}Fe, as will be shown in Subsection 6.3. We recall that the first order basis is approximated by

$$|\tilde{p}_\alpha^{(1)}\rangle \simeq \frac{1}{\sqrt{1+\delta_{q_\alpha}^2}}(|p_\alpha\rangle + \delta_{q_\alpha}|q_\alpha\rangle). \tag{6.32}$$

Here the mixing amplitude δ_{q_α} is

$$\delta_{q_\alpha} = \frac{\langle q_\alpha|H|p_\alpha\rangle}{E(\tilde{p}_\alpha^{(1)}) - E(q_\alpha)}. \tag{6.33}$$

As in the first order case, we assume

$$|q_\alpha^{(2)}\rangle \simeq |q'_\alpha\rangle = \frac{1}{\sigma_{q_\alpha}(H_{QQ})}[H_{QQ}|q_\alpha\rangle - E(q_\alpha)|q_\alpha\rangle], \tag{6.34}$$

where $\sigma_{q_\alpha}(H_{QQ})$ appears as the normalization constant.

The energy correction due to the second order renormalization is estimated as

$$\begin{aligned}
&\frac{|\langle q_\alpha^{(2)}|H|\tilde{p}_\alpha^{(1)}\rangle|^2}{E(\tilde{p}_\alpha^{(2)}) - E(q_\alpha^{(2)})} \\
\simeq\ & \frac{|\langle q'_\alpha|H|q_\alpha\rangle|^2}{E(\tilde{p}_\alpha^{(1)}) - E(q'_\alpha)} \cdot \frac{\delta_{q_\alpha}^2}{1+\delta_{q_\alpha}^2} \\
\simeq\ & \frac{[\sigma_{q_\alpha}(H_{QQ})]^2}{E(\tilde{p}_\alpha^{(1)}) - E(q'_\alpha)} \cdot \frac{|\langle q_\alpha|H|p_\alpha\rangle|^2}{[E(\tilde{p}_\alpha^{(1)}) - E(q_\alpha)]^2} \cdot \frac{[E(\tilde{p}_\alpha^{(1)}) - E(q_\alpha)]^2}{[E(\tilde{p}_\alpha^{(1)}) - E(q_\alpha)]^2 + |\langle q_\alpha|H|p_\alpha\rangle|^2} \\
=\ & \frac{1}{E(\tilde{p}_\alpha^{(1)}) - E(q'_\alpha)} \langle p_\alpha|H\hat{Q}H|p_\alpha\rangle \frac{[\sigma_{q_\alpha}(H_{QQ})]^2}{[E(\tilde{p}_\alpha^{(1)}) - E(q_\alpha)]^2 + \langle p_\alpha|H\hat{Q}H|p_\alpha\rangle}.
\end{aligned} \tag{6.35}$$

Thus the second order DBR gives a correction coming from the variance $[\sigma_{q_\alpha}(H_{QQ})]^2$. This correction resembles that in Eq.(6.18). The difference exists only in the energy denominators, aside from the transformation of the bases. The difference of the energy denominators from $[E - E(q_\alpha)]$ becomes higher order terms in the expansion with respect to λ from which Eq.(6.18) is derived.

6.3 Application of DBR to ^{56}Fe

We apply the DBR to the $\tilde{S}\tilde{D}$-space in ^{56}Fe. In the present work we consider up to the second order.

The energy levels obtained from $H_c^{(0)}$ is shown in the left column of Fig.21. They are the same as the unrenormalized levels in Fig.20. The right two columns are also the same as those in Fig.20; the shell model eigenstates and the $\tilde{S}\tilde{D}$-weighted averages of the shell model states. The 0^+ and 2^+ eigenfunctions of $H_c^{(0)}$ is listed in Table 18. We denote the eigenstates as 0_a^+, 0_b^+, and so on, according to the energy sequence. For instance, the lowest 0^+ state in the P-space is expressed as 0_a^+ state, the second 0^+ as 0_b^+.

The first and second order renormalized bases are shown in Tables 19 and 20, in terms of $|p_\alpha\rangle$ and $|q_\alpha^{(n)}\rangle$ states. The second order renormalization effectively lowers the energy of $|q_\alpha^{(1)}\rangle$ and increases the mixing amplitude of the state. Remark that the original $|p_\alpha\rangle$ component keeps at least 84% probability for the first order renormalized bases, 67% for the second order ones. The small amplitude of $|q_\alpha^{(2)}\rangle$ in each basis suggests that the bases will not vary drastically when higher order effects are included.

We can construct the renormalized collective hamiltonian $H_c^{(n)}$ from the n-th order renormalized bases. The n-th order energy levels are obtained

by diagonalizing $H_c^{(n)}$. The eigenenergies of $H_c^{(1)}$ and $H_c^{(2)}$ are shown in the second and the third left column of Fig.21.

The first order renormalization lowers the levels considerably, as well as diminishes energy intervals among the collective states. The lowest 0^+ and 2^+ states approach the shell model 0_1^+ and 2_1^+ states reasonably well. The second order renormalization further lowers the energies of the collective states. Though the lowest 0^+ and 2^+ states change only slightly, the energy decrease in the higher states are not negligible.

By comparing the second order levels with the shell model energies, we establish an excellent correspondence between the $\tilde{S}\tilde{D}$-states and the shell model ones through the renormalization. The 0_1^+ and 2_1^+ states are described very well in the renormalized $\tilde{S}\tilde{D}$-space. It should be remarked that the location in energy of the mixed-symmetry 2^+ and 1^+ states are understood reasonably well, apart from the splits. However, these splits of the mixed-symmetry 2^+ and 1^+ states are very small compared with the energy scale of the level spacing in the renormalized $\tilde{S}\tilde{D}$-space. This suggests that a weak coupling to another degree of freedom gives rise to the splits. No large mixing of the states in the Q-space into the mixed-symmetry states is consistent with this consideration.

The decomposition coefficients of the eigenstates of $H_c^{(1)}$ and $H_c^{(2)}$ are shown in Table 21 and 22. Comparing them with Table 18, we see that the renormalization scarcely affects the $\tilde{S}\tilde{D}$ structure of the eigenstates of the collective hamiltonian. The wavefunctions of the 0_a^+ and 2_a^+ states are also consistent with the $\tilde{S}\tilde{D}$ structure of the 0_1^+ and 2_1^+ states in the shell model.

Indeed, we obtain for the shell model states,

$$\left|\frac{\langle 0_1^+|\tilde{p}^{(2)}_{\alpha=0_{\tilde{S}}^+(\tilde{D}^2)}\rangle}{\langle 0_1^+|\tilde{p}^{(2)}_{\alpha=0_{\tilde{S}}^+(\tilde{S}^2)}\rangle}\right|^2 = 0.49, \quad \left|\frac{\langle 2_1^+|\tilde{p}^{(2)}_{\alpha=2_{\tilde{S}}^+(\tilde{D}^2)}\rangle}{\langle 2_1^+|\tilde{p}^{(2)}_{\alpha=2_{\tilde{S}}^+(\tilde{S}\tilde{D})}\rangle}\right|^2 = 0.21, \tag{6.36}$$

while for the eigenstate of $H_c^{(2)}$,

$$\left|\frac{\langle 0_a^+|\tilde{p}^{(2)}_{\alpha=0_{\tilde{S}}^+(\tilde{D}^2)}\rangle}{\langle 0_a^+|\tilde{p}^{(2)}_{\alpha=0_{\tilde{S}}^+(\tilde{S}^2)}\rangle}\right|^2 = 0.48, \quad \left|\frac{\langle 2_a^+|\tilde{p}^{(2)}_{\alpha=2_{\tilde{S}}^+(\tilde{D}^2)}\rangle}{\langle 2_a^+|\tilde{p}^{(2)}_{\alpha=2_{\tilde{S}}^+(\tilde{S}\tilde{D})}\rangle}\right|^2 = 0.22. \tag{6.37}$$

The mixed-symmetry 2^+ state stays pure, consistently with the consequence in Section 5 that neither the 2_2^+ nor 2_4^+ state includes the symmetric components. In other words, the F-spin-like symmetry conserves within the $\tilde{S}\tilde{D}$-space of ^{56}Fe.

Table 23 shows the overlaps of the $|\tilde{p}_\alpha^{(1)}\rangle$ states with the shell model eigenstates of ^{56}Fe. Similarly Table 24 shows those of the $|\tilde{p}_\alpha^{(2)}\rangle$ states. These overlaps should be compared with those in Table 16. Consistently with the energy levels, the 0_1^+ and 2_1^+ states are excellently described by the renormalized $\tilde{S}\tilde{D}$-states, already in the first order. The $\tilde{S}\tilde{D}$ probability of the 4_1^+ state is remarkably improved, as the order of the DBR goes up. The second order 4^+ state has a probability almost twice as large as the unrenormalized state, in the shell model 4_1^+ state. As for the mixed-symmetry 2^+ state, the 2_2^+ and 2_4^+ states amount to about $\frac{2}{3}$ of the component of the first order state, and $\frac{3}{4}$ of the second order state. No other states acquire such notable enhancement of the mixed-symmetry component. Similarly the mixed-symmetry 1^+ component is shared by the 1_2^+ and 1_3^+ states with enhanced strength; nearly 80% in the first order and 90% in the second order renormalization. Thus the conclusion about the mixed-symmetry states in Section 5 is further established through the renormalization.

Though the main fraction of the mixed-symmetry 2^+ and 1^+ components split into a few shell model states, the mixing amplitudes of the $|q_\alpha^{(1)}\rangle$ states remain small, as shown in Tables 19 and 20. Moreover, we know $\langle p_\alpha|H|q_{\alpha'}\rangle \simeq 0$ for $\alpha \neq \alpha'$, as mentioned in Subsection 6.2. Therefore, there are no states to which the mixed-symmetry components strongly couple via H. A weak coupling to non-collective degrees of freedom brings about the splits of the mixed-symmetry components. In the case that weak coupling is responsible for the splits, the energy difference between $|p_\alpha\rangle$ and a state in the Q-space must be small. In the DBR picture, the state in the Q-space will be a linear combination of the $|q_\alpha^{(n)}\rangle$ states with various n, unless its major component goes to a different block. Since the energy difference comes in the denominator of the mixing amplitude of the state in the Q-space, we would not be able to follow the splits without performing the DBR up to quite high order.

Though the main part of the mixed-symmetry 2^+ component is shared only by the 2_2^+ and 2_4^+ states, the mechanism of this splitting seems rather complicated. A remarkable feature of this split is the cancellation between the mixed-symmetry component and non-collective degrees of freedom in the $E2$ matrix elements. This feature cannot be described by the coupling to a single non-collective state. The cancellation seems to occur by the contribution of a large number of non-collective degrees of freedom.

By assuming the correspondence between the $\tilde{S}\tilde{D}$-states and the sd-boson states, we can evaluate the parameters of the boson hamiltonian,

$$H^B = E_0 + \sum_{\rho=\pi,\nu} \epsilon_{d_\rho} \hat{N}_{d_\rho} - \kappa Q_\pi^B \cdot Q_\nu^B + V_S + V_M. \tag{6.38}$$

The first term provides the zero-point energy. The second and the third

terms are the same as in Eq.(2.18). The Q_π^B and Q_ν^B operators contain the parameters χ_π and χ_ν, respectively (see Eq.(2.19)). We have the additional terms V_S and V_M, where

$$V_S = \sum_{J=0,2,4} c'_J [d_\pi^\dagger d_\nu^\dagger]^{(J)} \cdot [\tilde{d}_\pi \tilde{d}_\nu]^{(J)} \tag{6.39}$$

and

$$V_M = \sum_{J=1,2,3} \xi_J \hat{M}_J. \tag{6.40}$$

In the above expressions, c'_J's and ξ_J's are parameters and

$$\begin{aligned} \hat{M}_J &= [d_\pi^\dagger d_\nu^\dagger]^{(J)} \cdot [\tilde{d}_\nu \tilde{d}_\pi]^{(J)}, \quad (J = 1, 3) \\ \hat{M}_2 &= \frac{1}{2}[d_\pi^\dagger s_\nu^\dagger - s_\pi^\dagger d_\nu^\dagger]^{(2)} \cdot [\tilde{d}_\pi s_\nu - s_\pi \tilde{d}_\nu]^{(2)}. \end{aligned} \tag{6.41}$$

The V_M is called Majorana interaction, which is often employed in the IBM-2 in order to push up mixed-symmetry states. The microscopic origin of the interaction has not been manifested. Though Druce *et al.* showed that a part of the interaction may be accounted for by the renormalization of the effect of g-bosons[76, 77], similar interaction seems necessary also in the sdg-boson model[78]. The matrix elements of the collective hamiltonian

$$\begin{aligned} &\langle 0_S^+(\tilde{S}^2)|H_c^{(n)}|0_S^+(\tilde{S}^2)\rangle, \quad \langle 0_S^+(\tilde{S}^2)|H_c^{(n)}|0_S^+(\tilde{D}^2)\rangle, \\ &\langle 2_S^+(\tilde{S}\tilde{D})|H_c^{(n)}|2_S^+(\tilde{S}\tilde{D})\rangle, \quad \langle 2_S^+(\tilde{S}\tilde{D})|H_c^{(n)}|2_S^+(\tilde{D}^2)\rangle, \\ &\langle 2_M^+(\tilde{S}\tilde{D})|H_c^{(n)}|2_S^+(\tilde{S}\tilde{D})\rangle, \quad \langle 2_M^+(\tilde{S}\tilde{D})|H_c^{(n)}|2_S^+(\tilde{D}^2)\rangle, \end{aligned} \tag{6.42}$$

determines the parameters ϵ_ρ, κ and χ_ρ ($\rho = \pi, \nu$), as well as E_0. Note that the F-spin conservation indicates $\epsilon_{d_\pi} \simeq \epsilon_{d_\nu}$ and $\chi_\pi \simeq \chi_\nu$. The small differences in ϵ_{d_ρ} and χ_ρ are evaluated by the last two matrix elements in

Eq.(6.42). The remaining matrix elements of $H_c^{(n)}$ provide the additional terms V_S and V_M.

The boson parameters obtained from $H_c^{(0)}$, $H_c^{(1)}$ and $H_c^{(2)}$ are shown in Table 25. The additional terms V_S and V_M are negligibly small, compared with κ, in the unrenormalized result obtained from $H_c^{(0)}$. The κ decreases by the renormalization, while some of the terms in V_S and V_M become considerably larger. The V_S and V_M are almost the same between the first and the second order results. Devoting our attention to the Majorana interaction, the repulsive $\hat{M}_1$-force emerges by the renormalization. On the other hand, ξ_2 and ξ_3, the coefficients of the $\hat{M}_2$- and $\hat{M}_3$-term, are negligibly small, compared with the κ-parameter, even after the renormalization. The report by Druce *et al.*[76], who calculated the boson parameters by renormalizing the g-boson effect, gives similar consequence in the point that the $\hat{M}_1$-force is highly repulsive, while $\hat{M}_2$ is negligible. In their report, however, the $\hat{M}_3$-force is considerably repulsive. Note that vanishing $\hat{M}_2$-term has been suggested in Pd region[29] and in some rare-earth nuclei[13, 79], also from phenomenological standpoints.

The n-th order transition probabilities between collective states are calculated by using the $|\tilde{p}_\alpha^{(n)}\rangle$ states. In Table 26 the first and the second order $B(E2)$ and $B(M1)$ values are shown, as well as the unrenormalized ones. The same transition operators are employed as those adopted in the shell model calculation. The corresponding $B(E2)$ and $B(M1)$ values obtained in the shell model calculation are also exhibited in the right column of Table 26. In that column we show the sum of the transition probabilities from the 2_2^+ and 2_4^+ states with respect to the $E2$ and the $M1$ transitions from the 2_b^+ state, which is the almost pure mixed-symmetry state. Similarly the sum of

the $B(M1)$ from the 1_2^+ and 1_3^+ states is used for $B(M1; 1^+ \to 0_a^+)$.

We confirm that the first order renormalization improves these electromagnetic properties considerably. The second order gives slight correction to the first order result. This situation is typically seen in $B(E2; 2_a^+ \to 0_a^+)$. The $B(E2; 2_b^+ \to 0_a^+)$ value is much smaller than the sum of $B(E2; 2_2^+ \to 0_1^+)$ and $B(E2; 2_4^+ \to 0_1^+)$. This is caused by that the $B(E2)$ from the 2_2^+ and 2_4^+ states are contributed very much by non-collective states. The $B(M1)$ values from the mixed-symmetry states to the lowest-lying states, $B(M1; 2_b^+ \to 2_a^+)$ and $B(M1; 1^+ \to 0_a^+)$, agree quite well with the shell model values. Namely, the collective $M1$ transition probabilities are divided into the states having the split mixed-symmetry strengths; the 2_2^+ and 2_4^+ states for $B(M1; 2_b^+ \to 2_a^+)$, the 1_2^+ and 1_3^+ states for $B(M1; 1^+ \to 0_a^+)$. The non-collective degrees of freedom scarcely play a role in this case.

In the IBM, a well-deformed nucleus is described as the $SU(3)$-limit, while a spherical nucleus as the $U(5)$-limit. Eid *et al.* assumed that ^{56}Fe is a spherical nucleus[17]. This nucleus seems, however, far from the $U(5)$-limit, as is realized from the fact that the collective 4^+ state is much lower than the 0_b^+ and 2_c^+ states in the present calculation. The $B(E2; 2_1^+ \to 0_1^+)$ in ^{56}Fe is fairly larger than the value expected in a spherical nucleus in this region. It is pointed out in Ref.[25] that the relative $B(E2)$ values in the quasi-ground band are compatible with a well-developed deformation. The present wavefunctions of the 0^+ and 2^+ states have the $\tilde{S}\tilde{D}$-structure much closer to the $SU(3)$-limit than the $U(5)$-limit. On the other hand, the experimental value of the energy ratio $Ex(4_1^+)/Ex(2_1^+)$ is 2.5, suggesting the transitional character of this nucleus. The lowest mixed-symmetry state is expected to have $J^P = 1^+$ in well-deformed nuclei, while $J^P = 2^+$ in spherical

ones. Fig.21 shows that the mixed-symmetry 2^+ state is slightly lower than the mixed-symmetry 1^+. Note that this is caused by the difference in the strengths of the Majorana interaction. As a whole, ^{56}Fe seems a transitional nucleus, though it has some well-deformed characters to a certain extent.

We summarize this subsection. Through the second order DBR, we obtain a remarkable correspondence between the $\tilde{S}\tilde{D}$-states and the shell model states. This result clarifies the validity of the IBM-2, by the mediation of the renormalized $\tilde{S}\tilde{D}$-states. There appears no contradiction with the present $\tilde{S}\tilde{D}$-truncation. The assumption $N_\pi = N_\nu = 1$ also seems valid, despite the relaxation of the ^{56}Ni core. The energy splits of the mixed-symmetry 2^+ and 1^+ states are not seen in the process of the renormalization, indicating that the mixed-symmetry states are fragmented by a weak coupling to non-collective states. By this renormalization, we can convincingly conclude that the 2_2^+ and 2_4^+ states share the main part of the mixed-symmetry 2^+ component, as well as that the 1_2^+ and 1_3^+ share the mixed-symmetry 1^+ component. The F-spin-like symmetry is conserved remarkably well within the $\tilde{S}\tilde{D}$-space of this nucleus. This nature is kept through the renormalization. The repulsive $\hat{M}_1$-force, which is often used in phenomenological IBM-2 calculations, emerges due to the renormalization, though the $\hat{M}_2$- and $\hat{M}_3$-terms are negligibly small in contrast to most of phenomenological calculations.

7 Mixed-Symmetry States in Other Nuclei

7.1 ^{54}Cr

In ^{54}Cr there are two proton bosons and one neutron boson in the IBM-2, when we assume $Z = 20$ or 28 and $N = 28$ to be magic number. Then we have $F_0 = \frac{1}{2}$ and $F_{max} = \frac{3}{2}$.

It is very complicated to construct the extended SD-space, since there are some bases with the same spin-parity even in the proton space within the IBM-2. For instance, there are two 0^+ proton boson state, $|s_\pi^2\rangle$ and $|d_\pi^2; 0^+\rangle$. Hence it is advantageous to see the qualitative distribution of the mixed-symmetry 2^+ state by using the $(J_\pi - J_\nu)$ operator, as discussed in Section 5.

We consider the following state,

$$|2^+_{MSR}\rangle = \mathcal{N} P_{\mathcal{O}\{2_1^+\}} P_{T=3} P_{J=2} (J_\pi - J_\nu) |2_1^+\rangle. \tag{7.1}$$

This state holds main part of the mixed-symmetry 2^+ state, since the 2_1^+ state is predominantly comprised of totally symmetric components. Among the plural mixed-symmetry 2^+ states, the state defined in Eq.(7.1) is connected with the 2_1^+ state by the collective $M1$ transition. The lowest mixed-symmetry state would mainly consist of the $|2^+_{MSR}\rangle$ component. Table 27 exhibits the overlaps between the shell model eigenstates and the above $|2^+_{MSR}\rangle$ state. It is found that 43% of $|2^+_{MSR}\rangle$ is distributed in the 2_3^+ and 2_4^+ states, with the averaged energy of 3.3MeV and similar amount of the split to the case of ^{56}Fe. This result supports the suggestion in Refs.[18, 19].

We can discuss the nature of some states with respect to the F-spin-like symmetry, from the $E2$ and $M1$ matrix elements shown in Tables 5 and 10.

Table 5 displays the reduced matrix elements of Q_π and Q_ν in ^{54}Cr. Those of L_π, S_π, L_ν and S_ν are shown in Table 10. If the F-spin is conserved, the expectation value of J_π in the 2_1^+ state is twice as large as that of J_ν, as shown in Appendix B. In the shell model result, the expectation value of J_π is fairly larger than that of J_ν in the 2_1^+ state. Here we roughly estimate the mixing amplitude of the mixed-symmetry component in the 2_1^+ state. Assuming that the 2_1^+ state only consists of the components presented in Eqs.(2.16) and (2.17), the mixing amplitude can be evaluated by the ratio of the expectation value of J_π to that of J_ν. According to this estimation, the admixture of the mixed-symmetry component is only 1%, even though the ratio is smaller than 2 : 1. Therefore the 2_1^+ state seems almost totally symmetric.

In the case of $\chi_\pi = \chi_\nu$ in the boson $E2$ transition operator of Eq.(2.19), the ratio of the matrix element of Q_π between the 0_1^+ and 2_1^+ states relative to that of Q_ν should be 2 : 1, if the F-spin is conserved. The shell model result gives the ratio 1 : 1 approximately, which might mislead someone to larger F-spin breaking than is derived from the above comparison between the matrix elements of J_π and J_ν. However, we should notice that, according to the OAI mapping in the $k = 0$ configuration, the χ_π parameter in Eq.(2.19) is expected to be zero because of the particle-hole symmetry, while the χ_ν remains about -1 (see Eq.(2.29)). The approximate equality of the matrix elements of Q_π and Q_ν may be understood due to the difference between χ_π and χ_ν in the $E2$ operator, since even the ground state may include d-bosons to some extent.

As is shown in Table 27, the 2_2^+ state has negligibly small overlap with the $|2_{MSR}^+\rangle$ state. The 2_2^+ state has quite large $B(E2)$ value to the 2_1^+ state

both in the experiments and in the present calculation. Relating to that, the transition matrix element of Q_π from this state to the 2_1^+ has the same sign as that of Q_ν. These facts suggest that the 2_2^+ state is dominated by the $N_d = 2$ component, where N_d means the d-boson number, or includes a component corresponding to the g-boson. In either case this state is almost symmetric with respect to the proton-neutron degrees of freedom.

We remark that in the 2_4^+ state there appears a remarkable cancellation of the $E2$ matrix elements between the mixed-symmetry component and non-collective degrees of freedom, as seen in ^{56}Fe, while the cancellation is not so extreme in the 2_3^+.

We cannot discuss collective features of 2^+ states from the $C2$ form factor, shown in Fig.13, since there are no data points with respect to the 2_3^+ and 2_4^+ states so far. It is found that the experimental form factor is excellently reproduced for the 2_1^+ state. As for the 2_2^+ state, the form factor is overall underestimated by factor of 2. This implies that the r-dependence of the transition density is reproduced fairly well, though the absolute value is underestimated. Since the transition from the 2_2^+ to the 0_1^+ state is not a collective one, this discrepancy would not be a serious disadvantage, as in the case of the 2_3^+ states of ^{56}Fe.

We turn to the mixed-symmetry 1^+ component. In Table 27, we show the distribution of the state,

$$|1_{MSR}^+\rangle = \mathcal{N} P_{T=3}(J_\pi - J_\nu)|0_1^+\rangle, \tag{7.2}$$

over the shell model eigenstates. The 1_3^+ state has large overlap with the $|1_{MSR}^+\rangle$ component, though this state has not been observed yet.

7.2 ^{52}Ti

We can search for the mixed-symmetry 2^+ state by using the $(J_\pi - J_\nu)$ operator introduced in Section 5 again. Consider the following state

$$|2^+_{MSR}\rangle = \mathcal{N} P_{\mathcal{O}\{2^+_1\}} P_{T=4} P_{J=2} (J_\pi - J_\nu)|2^+_1\rangle, \tag{7.3}$$

which holds major part of the mixed-symmetry 2^+ state, as far as the 2^+_1 state is mainly comprised of totally symmetric states. Table 28 exhibits the overlaps between the shell model eigenstates and the above $|2^+_{MSR}\rangle$ state. It is found that about 60% of $|2^+_{MSR}\rangle$ is shared by the 2^+_2, 2^+_3 and 2^+_4 states. This consequence is in agreement with the suggestion in Ref.[19], though the 2^+_4 state was not mentioned in the reference. The 2^+_2 and 2^+_3 states are located with the small difference in energy around $Ex = 2.3$MeV, while the 2^+_4 state has $Ex = 3.5$MeV. The separation in energy of the 2^+_4 state could be explained by the existence of plural mixed-symmetry states, when we accept the larger neutron boson number than unity as discussed below.

Reduced matrix elements of Q_π and Q_ν are displayed in Table 6, as well as those of L_π, S_π, L_ν and S_ν in Table 11, for the ^{52}Ti nucleus. In this nucleus we have $N_\pi = N_\nu = 1$ within the IBM-2, when we assume $Z = 20$ and $N = 28$ to be magic number. We, however, see that the expectation value of J_ν in the 2^+_1 state is about twice as large as that of J_π. Similar ratios are obtained for the matrix elements of Q_π and Q_ν from the 2^+_1 to the 0^+_1 state, as well as for the expectation values of Q_π and Q_ν in the 2^+_1 state. The following two interpretations are possible, when the IBM-2 picture is maintained. One is that the totally symmetric nature is broken in the 2^+_1 state in ^{52}Ti. The other is that the normal boson number consideration is not adequate in this nucleus. In the present calculation, the excitation across

$Z = 20$ is forbidden, while that across $N = 28$ is allowed. We might have to define the boson number by taking this effect into account in this nucleus.

For a qualitative discussion, we adopt the boson hamiltonian of Eq.(2.18) again. Recall the OAI mapping within the $k = 0$ configuration which is adopted in Section 2. We have $\chi_\pi \simeq -\chi_\nu$ in ^{52}Ti, while Eq.(2.29) shows $\chi_\pi \simeq \chi_\nu$ in ^{56}Fe. This is a consequence of the particle-hole conjugation. As is discussed in Appendix A, it follows that the 2^+_1 state is totally symmetric in a good approximation in ^{52}Ti. At least it is hard to accept that there is larger admixture of the mixed-symmetry component into the 2^+_1 state in ^{52}Ti than in ^{54}Cr, although a small F-spin breaking is also seen in ^{54}Cr. Thus we should give up $N_\pi = N_\nu = 1$, leading to the idea of the effective boson number[80]. The matrix elements in the 2^+_1 state suggest $N_\nu = 2$, under the assumption that this state is almost totally symmetric.

One notices that the 2^+_2 and 2^+_3 states have large $B(E2)$ values to the 2^+_1 state, similarly to the 2^+_2 state in ^{54}Cr. These states would be interpreted to share the component with $N_d = 2$. If it is true, we should conclude a large mixing of the F-spin, since these states also have a considerable amount of the $|2^+_{MSR}\rangle$ component. This mixing is reasonably understood by the consideration based on the hamiltonian of Eq.(2.18), if we keep $\chi_\pi \simeq -\chi_\nu$. The low energy of the $N_d = 2$ component is consistent with the introduction of the effective boson number, since otherwise it would be difficult for the collectivity to grow up in $N_d = 2$ component. Note that the discussions in this paragraph concern only the coupling of the mixed-symmetry 2^+ component to other degrees of freedom. The consequence about the mixed-symmetry 2^+ component based on the $|2^+_{MSR}\rangle$ state is not influenced by them.

We also point out that the matrix element of S_ν from the 2^+_3 to the 2^+_1

state is as large as that of L_ν. In comparison with the cases of ^{56}Fe and ^{54}Cr, this is very exceptional. The mixed-symmetry 2^+ mode couples to a neutron spin excitation mode in ^{52}Ti.

We turn to the mixed-symmetry 1^+ component. In Table 27, we show the distribution of the state,

$$|1^+_{MSR}\rangle = \mathcal{N} P_{T=4}(J_\pi - J_\nu)|0^+_1\rangle, \tag{7.4}$$

over the shell model eigenstates. The 1^+_3 state has large overlap with the $|1^+_{MSR}\rangle$ component.

7.3 Systematics of Mixed-Symmetry States in $N = 30$ Isotones

In Section 5 and the preceding subsections in this section, we have shown that in the $N = 30$ isotones, ^{52}Ti, ^{54}Cr and ^{56}Fe, there systematically exist a few states in $2 < Ex < 4$MeV on which the mixed-symmetry 2^+ component concentrate. The mixed-symmetry 1^+ components also seem to concentrate on a few states with a little higher energies than the mixed-symmetry 2^+ components. Actually the 1^+_3 state in each isotone has the largest fraction of the mixed-symmetry 1^+ component. We discuss some systematics of these states in this subsection.

As was discussed in Section 2, the mixed-symmetry 2^+ state should be the lowest mixed-symmetry state in spherical nuclei, while the mixed-symmetry 1^+ state should be the lowest in well-deformed nuclei with the axial symmetry. In Fig.22, $B(E2; 2^+_1 \to 0^+_1)$ and the ratio $Ex(4^+_1)/Ex(2^+_1)$ in the $N = 30$ isotones are displayed. It is well-known that generally $B(E2; 2^+_1 \to 0^+_1)$ increases as the deformation becomes large. The ratio of the excitation energy

of the 4^+_1 state relative to that of the 2^+_1 state is also a probe for the deformation. We have $Ex(4^+_1)/Ex(2^+_1) = 2$ for the vibrational spectra seen in spherical nuclei, while $Ex(4^+_1)/Ex(2^+_1) = 10/3$ for the rotational spectra appearing in well-deformed nuclei. These quantities seem to indicate the tendency that the deformation evolves with atomic number Z in these isotones. On the other hand, Fig.23 shows the excitation energies of the states having the largest fraction of the mixed-symmetry 2^+ or 1^+ component. In comparison with Fig.22, we see the expected correlation between the excitation energies of the mixed-symmetry states and the deformation. As the deformation becomes large, the energy of the mixed-symmetry 2^+ state goes up and that of the mixed-symmetry 1^+ state goes down.

We can qualitatively realize the evolution of deformation and the diminution of the F-spin mixing with the increase of Z, by the $Q^B_\pi \cdot Q^B_\nu$ interaction in Eq.(2.18). This boson interaction is generated from the $Q_\pi \cdot Q_\nu$ interaction for nucleons under a simplest consideration. We recall the OAI mapping in which we assume the inertness of $N = Z = 28$ and the degeneracy of the neutron orbits, adopted in Section 2. According to the seniority reduction formulae[81], the effective boson charge e^B_ρ varies little within a single major shell, while in the χ_ρ parameter even its sign changes at the middle of the shell. This situation is maintained in a microscopic calculation where we take the non-degeneracy of the orbits into account[82]. We have $\chi_\pi \simeq \chi_\nu$ in ^{56}Fe, as is shown in Eq.(2.29). In the OAI mapping the χ_ν value is common for all the $N = 30$ isotones, whereas $\chi_\pi = 0$ in ^{54}Cr and $\chi_\pi \simeq -\chi_\nu$ in ^{52}Ti, as mentioned in Subsections 7.1 and 7.2. Though there is a problem concerning the boson number in ^{52}Ti, the value of χ_ν will not vary so much. Due to the difference of χ_π from χ_ν, the F-spin conservation is destroyed, as well as the

system approaches the spherical phase, as shown in Appendix A. Thus the features of individual nucleus can be explained qualitatively by the behavior of the χ_π parameters.

Now we discuss experimental probes for the mixed-symmetry 2^+ state. We can classify expected experimental probes into two categories. One is the 1^+ transition to the 2_1^+ state. The $M1$ transition probability is the only probe of this kind available at present. The other is the 2^+ transition to the 0_1^+ state; $B(E2)$, electron scattering and proton scattering. The $M1$ transition from the state with a large fraction of the mixed-symmetry 2^+ component must be strong. However, the existence of non-collective state, together with the split of the mixed-symmetry component into a few states, make it complicated to identify the mixed-symmetry state. Especially we should take care for a spin excitation mode, since the mode can acquire a large $M1$ transition strength because of large $g_{s,\rho}$ parameters in Eq.(4.10). It is a reason that a large $M1$ transition probability to the 2_1^+ state is not a decisive probe by itself, though it seems a necessary condition. The expected $E2$ transition probability is not strong enough to identify the mixed-symmetry 2^+ state without obscurity. We cannot relate an enhancement in high q region in the $C2$ form factors to the mixed-symmetry component, even if there exists a pure mixed-symmetry 2^+ state. Furthermore, the form factor of the mixed-symmetry 2^+ state is seriously disturbed by the coupling to non-collective degrees of freedom. We have no characteristic angular distribution in the $(\vec{p}, p')$ cross section, either.

Therefore some combination of observables is required to identify the mixed-symmetry 2^+ state experimentally. Both the 1^+ transition to the 2_1^+ state and the 2^+ transition to the 0_1^+ state should be observed. The $B(M1)$ to the 2_1^+ state would be the initiative probe, while the $B(E2)$ to the 0_1^+ state is

promising to reject non-collective modes like spin excitation. By a split into a few states, the expected $B(M1)$ value estimated in Eq.(2.41) will be divided into the states. On the other hand, the $B(E2)$ value in Eq.(2.31) might not become smaller. This is because the coupled state bringing about the split could have sizable $E2$ transition probability to the 0_1^+ state, though the state would have wholly different proton and neutron constitution from the 2_1^+ state. In the present calculation for the $N = 30$ isotones, both the $B(E2)$ and $B(M1)$ values are the least in the 2_4^+ state of ^{52}Ti, among the states with considerable amplitudes of the mixed-symmetry component; the $B(E2)$ is $0.05[e^2fm^4]$ and the $B(M1)$ is $0.07[\mu_N^2]$. Except for this state, the $B(M1)$ is $0.1[\mu_N^2]$, while the $B(E2)$ is $5[e^2fm^4]$, at least. Thus the combination of $B(M1)$ and $B(E2)$ data would help us in identifying the mixed-symmetry 2^+ state. If the (e, e') and (p, p') experiments are possible, their comparison enables us to discuss the proton and neutron contribution in the 2^+ transition. Therefore the identification will be easier by using those scattering data.

8 Summary and Conclusion

We apply a large-scale shell model calculation to nuclei in $20 < Z \leq 28$, $28 \leq N \leq 30$ region, by using the Kuo-Brown interaction. This interaction is derived from a nucleon-nucleon interaction. Though there are no adjustable parameters, the energy levels are excellently reproduced up to 4MeV, within the accuracy of 0.2MeV. It is found that the inertness of $N = Z = 28$ is broken by about 40% even in the ground state of each nucleus. The $E2$ transition probabilities are systematically reproduced by using the effective charges adjusted at ^{56}Fe, except for the semi-magic nuclei, ^{54}Fe and ^{58}Ni. The calculation with the j-dependent effective charges, which is microscopically evaluated based on the HF+RPA, gives consistent $B(E2)$ values. The $M1$ transition probabilities are reproduced well as a whole, by the same single particle g-factors as in Ref.[41], though there remains some discrepancies in non-collective transitions. It is suggested that additional terms are necessary to describe non-collective $M1$ transitions.

The $C2$ form factors are calculated by combining the shell model density matrices with the renormalized single particle transition densities evaluated by HF+RPA. The satisfactory agreement with the data is attained by this parameter-free calculation, especially for ^{56}Fe. The $(\vec{p}, p')$ differential cross sections are also reproduced by using reasonable normalization factors, for ^{56}Fe and ^{54}Cr.

We search for the mixed-symmetry states in $N = 30$ isotones, ^{56}Fe, ^{54}Cr and ^{52}Ti, by inspecting the shell model wavefunctions thus tested.

In ^{56}Fe, the wavefunctions are investigated by using the extended SD-states, which are collective degrees of freedom extracted from the 0_1^+ and 2_1^+

states, and are called $\tilde{S}\tilde{D}$-states in this thesis. Such an extension is required for precise discussions of higher states like the mixed-symmetry states, since the $k > 0$ configurations are necessary to reproduce the properties of the states. The requirement of the $\tilde{S}\tilde{D}$-states would lead to an extension of boson mapping beyond the simple correspondence between a boson and a pair of nucleons. By the decomposition into the $\tilde{S}\tilde{D}$-states, the 2_2^+ and 2_4^+ states are found to share the mixed-symmetry 2^+ component. The mixed-symmetry 1^+ component is shared by the 1_2^+ and 1_3^+ states. The 1_3^+ state has not been observed. Hence the physical observables with respect to this state, the energy and the $B(M1)$ value to the ground state, are predictions. The search for the mixed-symmetry components by using the $(J_\pi - J_\nu)$ operator is also proposed, and is shown to be qualitatively consistent with the results based on the $\tilde{S}\tilde{D}$-states. The dominance of the orbital angular momentum relative to the spin is pointed out for the collective $M1$ transition matrix elements. It is remarkable that the mixed-symmetry components concentrate on only a few states even in the present realistic and microscopic study. This result has not been trivial, though it is rather natural in a calculation in a restricted space as in Ref.[58].

The diagonalized-block renormalization (DBR) is proposed as a way to incorporate the space outside the $\tilde{S}\tilde{D}$-space. By applying the method, we can realize the correspondence between the $\tilde{S}\tilde{D}$-states and the shell model eigenstates in ^{56}Fe. The energies and electromagnetic properties of the collective states are described quite well by this renormalization without introducing additional degrees of freedom, apart from the splitting of some components. The F-spin-like symmetry conserves very well within the $\tilde{S}\tilde{D}$-space of ^{56}Fe. This is consistent with the overlaps between the $\tilde{S}\tilde{D}$-states and the low-lying

states in ^{56}Fe. The mixed-symmetry 2^+ and 1^+ states split into a few states. Such a split of mixed-symmetry states has already seen in the scissors mode. In the same manner as the scissors mode, the concept of the mixed-symmetry state should be understood as an appropriate superposition of a few states distributed over a small energy range.

The IBM-2 hamiltonian is derived from the DBR wavefunctions. The microscopic origin of the Majorana interaction has not been manifested so far. In the present microscopic study the renormalization originates the $\hat{M}_1$-term of the Majorana interaction, though the $\hat{M}_2$- and $\hat{M}_3$-terms are very small.

It is pointed out that the perturbative renormalization, which is based on the Feshbach's projection method and the closure approximation, also works well. The success, however, seems due to an accidental cancellation between two correction factors, to a certain extent.

The mixed-symmetry states in ^{54}Cr and ^{52}Ti are also investigated by using the $(J_\pi - J_\nu)$ operator. Although a small F-spin mixing is probable in ^{54}Cr and ^{52}Ti, the search based on the $(J_\pi - J_\nu)$ operator will be meaningful, as far as main part of the 2_1^+ state consists of the totally symmetric components. It is suggested that the 2_3^+ and 2_4^+ states share the mixed-symmetry 2^+ component in ^{54}Cr, while the 2_2^+, 2_3^+ and 2_4^+ states do in ^{52}Ti. Both in ^{54}Cr and ^{52}Ti, the 1_3^+ states are predicted to have the largest fraction of the mixed-symmetry 1^+ components, though those states have not been observed yet.

Thus there systematically exist a few states having large fractions of the mixed-symmetry 2^+ and 1^+ components in the $N = 30$ isotones. It should be emphasized that those components seem to concentrate on a few states

in each nucleus, not fragmented so much. It is also noted that the energies of the states sharing the mixed-symmetry components are fairly low, lower than most of non-collective states with the same seniority.

The deformation seem to grow up with the proton number Z in the $N = 30$ isotones. By seeing the systematics, the correlation between the deformation and the energies of the mixed-symmetry 2^+ and 1^+ states is suggested. This is consistent with the expectation in the IBM-2. The deformation and the F-spin mixing in these isotones are realized qualitatively by the schematic $Q_\pi \cdot Q_\nu$ interaction.

Experimental probes for the mixed-symmetry 2^+ state are discussed. Neither the $M1$ transition probabilities nor the $C2$ form factors can be decisive as a single probe. We require some combination of observables including both the 1^+ transition to the 2_1^+ state and the 2^+ transition to the 0_1^+ state.

Appendices

A $Q_\pi^B \cdot Q_\nu^B$ Interaction around the $U(5)$-Limit of the IBM-2

The hamiltonian of Eq.(2.18) is often used in the IBM-2. We discuss the $Q_\pi^B \cdot Q_\nu^B$ interaction, which is the only two-body interaction included in this hamiltonian. The Q_π^B and Q_ν^B are defined in Eq.(2.19). As a general notice, we point out that the coefficient of the $Q_\pi^B \cdot Q_\nu^B$ interaction is negative.

The $Q_\pi^B \cdot Q_\nu^B$ interaction can be rewritten as

$$Q_\pi^B \cdot Q_\nu^B = \frac{1}{4}\{(Q_\pi^B + Q_\nu^B)\cdot(Q_\pi^B + Q_\nu^B) - (Q_\pi^B - Q_\nu^B)\cdot(Q_\pi^B - Q_\nu^B)\}. \quad \text{(A.1)}$$

Note that the first term in the right-handed side of Eq.(A.1) is scalar with respect to the F-spin, if $\chi_\pi = \chi_\nu$. On account of the negative sign of the coefficient of the $Q_\pi^B \cdot Q_\nu^B$ interaction, the first term works as an attractive interaction, while the second term a repulsive interaction. Hence, roughly speaking, the first term pushes down the symmetric state of Eq.(2.16), while the second term pushes up the mixed-symmetry state of Eq.(2.17).

For the purpose of more precise discussion, the $Q_\pi^B \cdot Q_\nu^B$ interaction is rewritten in the normal-ordered form,

$$\begin{aligned} Q_\pi^B \cdot Q_\nu^B &= \{s_\pi^\dagger s_\nu^\dagger \tilde{d}_\pi \cdot \tilde{d}_\nu + \text{h.c.}\} + \{d_\pi^\dagger s_\nu^\dagger \cdot s_\pi \tilde{d}_\nu + \text{h.c.}\} \\ &\quad + \chi_\pi\{d_\pi^\dagger s_\nu^\dagger \cdot [\tilde{d}_\pi \tilde{d}_\nu]^{(2)} + \text{h.c.}\} + \chi_\nu\{s_\pi^\dagger d_\nu^\dagger \cdot [\tilde{d}_\pi \tilde{d}_\nu]^{(2)} + \text{h.c.}\} \\ &\quad + 5\chi_\pi\chi_\nu \sum_{0\le J\le 4} (-)^J W(2,2,2,2;2,J)[d_\pi^\dagger d_\nu^\dagger]^{(J)} \cdot [\tilde{d}_\pi \tilde{d}_\nu]^{(J)}, \end{aligned} \quad \text{(A.2)}$$

where $W(j_1, j_2, j_3, j_4; J, J')$ stands for the Racah coefficient. In the $U(5)$-limit, the ground state is given by Eq.(2.13). This state only mix with the

state $|s_\pi^{N_\pi-1} d_\pi s_\nu^{N_\nu-1} d_\nu; 0^+\rangle$ by the $Q_\pi^B \cdot Q_\nu^B$ interaction. The mixing matrix element is evaluated as

$$\langle 0_S^+(s^{N_B})|Q_\pi^B \cdot Q_\nu^B|s_\pi^{N_\pi-1} d_\pi s_\nu^{N_\nu-1} d_\nu; 0^+\rangle = \sqrt{5N_\pi N_\nu}. \quad \text{(A.3)}$$

The admixture will be very small around the $U(5)$-limit, because of the $\hat{N}_d$ term of the hamiltonian, since those states differ in the d-boson number by two.

As for the 2^+ states of Eqs.(2.16) and (2.17), we obtain

$$\begin{aligned} \langle 2_S^+(s^{N_B-1}d)|Q_\pi^B \cdot Q_\nu^B|2_S^+(s^{N_B-1}d)\rangle &= 2\frac{N_\pi N_\nu}{N_B}, \\ \langle 2_M^+(s^{N_B-1}d)|Q_\pi^B \cdot Q_\nu^B|2_M^+(s^{N_B-1}d)\rangle &= -2\frac{N_\pi N_\nu}{N_B}, \\ \langle 2_M^+(s^{N_B-1}d)|Q_\pi^B \cdot Q_\nu^B|2_S^+(s^{N_B-1}d)\rangle &= -(N_\pi - N_\nu)\frac{\sqrt{N_\pi N_\nu}}{N_B}. \end{aligned} \quad \text{(A.4)}$$

Recalling the sign of the κ parameter, we confirm that the symmetric state of Eq.(2.16) is pushed down by the $Q_\pi^B \cdot Q_\nu^B$ interaction, while the mixed-symmetry state of Eq.(2.17) is pushed up. The mixing matrix element becomes much smaller than the energy difference between the two states, when $(N_\pi - N_\nu)^2 \ll N_\pi N_\nu$.

The state of Eq.(2.16) or (2.17) can couple to the $|s_\pi^{N_\pi-1} d_\pi s_\nu^{N_\nu-1} d_\nu; 2^+\rangle$ state through the $Q_\pi^B \cdot Q_\nu^B$ interaction. Those couplings induce a deformation. It is noted that the $|s_\pi^{N_\pi-1} d_\pi s_\nu^{N_\nu-1} d_\nu; 2^+\rangle$ state is equivalent to the $|2_S^+(s^{N_B-2}d^2)\rangle$ state if $N_\pi = N_\nu = 1$. The mixing matrix elements are evaluated as

$$\begin{aligned} \langle 2_S^+(s^{N_B-1}d)|Q_\pi^B \cdot Q_\nu^B|s_\pi^{N_\pi-1} d_\pi s_\nu^{N_\nu-1} d_\nu; 2^+\rangle &= \frac{1}{\sqrt{N_B}}(\chi_\pi N_\pi + \chi_\nu N_\nu), \\ \langle 2_M^+(s^{N_B-1}d)|Q_\pi^B \cdot Q_\nu^B|s_\pi^{N_\pi-1} d_\pi s_\nu^{N_\nu-1} d_\nu; 2^+\rangle &= \sqrt{\frac{N_\pi N_\nu}{N_B}}(\chi_\pi - \chi_\nu). \end{aligned} \quad \text{(A.5)}$$

Remark that these matrix elements depend on the χ parameters. If $N_\pi \simeq N_\nu$ and $\chi_\pi \simeq \chi_\nu$, the mixed-symmetry 2^+ state scarcely mix with any other states through the $Q^B_\pi \cdot Q^B_\nu$ interaction. Therefore the F-spin will conserve very well. In addition, the $|s_\pi^{N_\pi-1} d_\pi s_\nu^{N_\nu-1} d_\nu; 2^+\rangle$ state may mix into the 2^+_1 state in this case. This implies some deformation of the nucleus under consideration. On the other hand, when $N_\pi \simeq N_\nu$ and $\chi_\pi \simeq -\chi_\nu$, the coupling between the $|2^+_S(s^{N_B-1}d)\rangle$ state and the $|s_\pi^{N_\pi-1} d_\pi s_\nu^{N_\nu-1} d_\nu; 2^+\rangle$ state approaches zero, suggesting the spherical shape of the nucleus. Furthermore, the 2^+_1 state is totally symmetric in quite a good approximation, since the coupling between the $|2^+_S(s^{N_B-1}d)\rangle$ and $|2^+_S(s^{N_B-1}d)\rangle$ states remains small. The $|s_\pi^{N_\pi-1} d_\pi s_\nu^{N_\nu-1} d_\nu; 2^+\rangle$ state, however, can considerably mix with the $|2^+_M(s^{N_B-1}d)\rangle$ state. Hence the F-spin breaking seems inevitable in these higher states.

B Matrix Elements of One-Body Operators between Totally Symmetric States in the IBM-2

We consider an arbitrary one-body operator in the IBM-2, denoted by T. This operator consists of a proton term and a neutron term,

$$T = c_\pi T_\pi + c_\nu T_\nu, \tag{B.1}$$

where T_π and T_ν are proton and neutron operators, respectively, and c_π and c_ν are coefficients of the operators. In the F-spin algebra, the operator is divided into the F-scalar term and the F-vector term,

$$T = c_0 T^{(0)}_0 + c_1 T^{(1)}_0. \tag{B.2}$$

Here c_0 and c_1 are appropriate coefficients, in some cases they are linear combinations of c_π and c_ν. In the expression $T^{(l)}_m$, the l and m represent the rank in the F-spin space and its z-component throughout this Appendix.

Let us consider two states $|F = F_{max}, F_0, \sigma\rangle$ and $|F = F_{max}, F_0, \sigma'\rangle$, where σ and σ' stand for additional quantum number other than F-spin. By using the Wigner-Eckart theorem in the F-spin $SU(2)$ space, we obtain

$$\begin{aligned}
&\langle F = F_{max}, F_0, \sigma' | T^{(0)}_0 | F = F_{max}, F_0, \sigma\rangle \\
&= \frac{1}{\sqrt{2F_{max}+1}} \langle F = F_{max}, \sigma' \| T^{(0)} \| F = F_{max}, \sigma\rangle_F \\
&\quad \times (F_{max}, F_0, 0, 0 | F_{max}, F_0) \\
&= \frac{1}{\sqrt{2F_{max}+1}} \langle F = F_{max}, \sigma' \| T^{(0)} \| F = F_{max}, \sigma\rangle_F,
\end{aligned} \tag{B.3}$$

and

$$\langle F = F_{max}, F_0, \sigma' | T^{(1)}_0 | F = F_{max}, F_0, \sigma\rangle$$

$$= \frac{1}{\sqrt{2F_{max}+1}}\langle F=F_{max},\sigma'\|T^{(1)}\|F=F_{max},\sigma\rangle_F \times(F_{max},F_0,1,0|F_{max},F_0)$$
$$= \frac{1}{\sqrt{2F_{max}+1}}\langle F=F_{max},\sigma'\|T^{(1)}\|F=F_{max},\sigma\rangle_F \times \frac{F_0}{\sqrt{F_{max}+1}}. \quad \text{(B.4)}$$

The subscript F in the reduced matrix elements represents that the reduction is performed in the F-spin space. The factor $(j_1,m_1,j_2,m_2|J,M)$ is the Clebsch-Gordan coefficient.

In order to evaluate the reduced matrix elements, we consider the $F_0 = F_{max}$ nucleus, namely a system consisting only of proton bosons. Substituting the F_0 in Eqs.(B.3) and (B.13) by F_{max}, we have

$$\langle F=F_{max},F_0=F_{max},\sigma'|T_0^{(0)}|F=F_{max},F_0=F_{max},\sigma\rangle = \frac{1}{\sqrt{2F_{max}+1}}\langle F=F_{max},\sigma'\|T^{(0)}\|F=F_{max},\sigma\rangle_F, \quad \text{(B.5)}$$

$$\langle F=F_{max},F_0=F_{max},\sigma'|T_0^{(1)}|F=F_{max},F_0=F_{max},\sigma\rangle = \frac{1}{\sqrt{2F_{max}+1}}\langle F=F_{max},\sigma'\|T^{(1)}\|F=F_{max},\sigma\rangle_F \times \sqrt{\frac{F_{max}}{F_{max}+1}}. \quad \text{(B.6)}$$

Now we assume the following relation holds,

$$T_0^{(0)} = T_\pi + T_\nu, \quad T_0^{(1)} = T_\pi - T_\nu. \quad \text{(B.7)}$$

In this case we have the relation for the coefficients in Eqs.(B.1) and (B.2) as

$$c_0 = \frac{1}{2}(c_\pi + c_\nu), \quad c_1 = \frac{1}{2}(c_\pi - c_\nu). \quad \text{(B.8)}$$

Then we obtain for the left-handed sides of Eqs.(B.5) and (B.6),

$$\langle F=F_{max},F_0=F_{max},\sigma'|T_0^{(0)}|F=F_{max},F_0=F_{max},\sigma\rangle$$

$$= \langle F=F_{max},F_0=F_{max},\sigma'|T_0^{(1)}|F=F_{max},F_0=F_{max},\sigma\rangle$$
$$= \langle F=F_{max},F_0=F_{max},\sigma'|T_\pi|F=F_{max},F_0=F_{max},\sigma\rangle \equiv \langle T\rangle, \quad \text{(B.9)}$$

since we have no neutron bosons in $F_0 = F_{max}$ system. The reduced matrix elements in the F-spin space are evaluated as

$$\langle F=F_{max},\sigma'\|T^{(0)}\|F=F_{max},\sigma\rangle_F = \langle T\rangle\cdot\sqrt{2F_{max}+1}, \quad \text{(B.10)}$$

$$\langle F=F_{max},\sigma'\|T^{(1)}\|F=F_{max},\sigma\rangle_F = \langle T\rangle\cdot\sqrt{\frac{(F_{max}+1)(2F_{max}+1)}{F_{max}}}, \quad \text{(B.11)}$$

Note that $F_{max} \neq 0$ holds except for the boson vacuum, which attracts no physical interest.

By the substitution of Eqs.(B.10) and (B.11) into Eqs.(B.3) and (B.4), we obtain

$$\langle F=F_{max},F_0,\sigma'|T_0^{(0)}|F=F_{max},F_0,\sigma\rangle = \langle T\rangle, \quad \text{(B.12)}$$

$$\langle F=F_{max},F_0,\sigma'|T_0^{(1)}|F=F_{max},F_0,\sigma\rangle = \langle T\rangle\cdot\frac{F_0}{F_{max}}. \quad \text{(B.13)}$$

Therefore the matrix elements of T_π and T_ν are evaluated as

$$\langle F=F_{max},F_0,\sigma'|T_\pi|F=F_{max},F_0,\sigma\rangle = \langle F=F_{max},F_0,\sigma'|\frac{1}{2}(T_0^{(0)}+T_0^{(1)})|F=F_{max},F_0,\sigma\rangle = \frac{1}{2}(1+\frac{F_0}{F_{max}})\langle T\rangle = \frac{N_\pi}{N}\langle T\rangle, \quad \text{(B.14)}$$

$$\langle F=F_{max},F_0,\sigma'|T_\nu|F=F_{max},F_0,\sigma\rangle = \langle F=F_{max},F_0,\sigma'|\frac{1}{2}(T_0^{(0)}-T_0^{(1)})|F=F_{max},F_0,\sigma\rangle = \frac{1}{2}(1-\frac{F_0}{F_{max}})\langle T\rangle = \frac{N_\nu}{N}\langle T\rangle. \quad \text{(B.15)}$$

Namely, the ratio of the matrix element of T_π relative to that of T_ν is $N_\pi : N_\nu$ between the totally symmetric states, as far as the relation (B.7) is satisfied. This fact is pointed out and proved in Ref.[30].

In the usual IBM-2 description, $M1$ transition operator is given by Eq.(2.33). This $M1$ operator can be rewritten as Eq.(2.35). The first term in the right-handed side of Eq.(2.35) is F-scalar, while the second term is F-vector. Namely, Eq.(B.7) is satisfied for J^B_π and J^B_ν. We can easily prove that the $M1$ transition between $F = F_{max}$ states is forbidden[29]. The F-scalar term in the right-handed side of Eq.(2.35) never produces transitions, since it is proportional to the total angular momentum. Hence the $M1$ transition operator is essentially proportional to $J^B_\pi - J^B_\nu$. However, the vanishing F-scalar term for $\sigma \neq \sigma'$ leads to the consequence that the F-vector term also vanishes, since $\langle T \rangle = 0$ is derived from Eq.(B.12). Thus the $M1$ transition is forbidden between two orthogonal $F = F_{max}$ states in the IBM-2. If we introduce other bosons, g-bosons for example, it is not the case since there could be additional one-body terms in $T^B(M1)$.

We can check the F-spin conservation in some lowest-lying states by seeing the ratio of the matrix elements of the J^B_π and J^B_ν, except for 0^+ states. For Q^B_π and Q^B_ν defined in Eq.(2.19), Eq.(B.7) holds when $\chi_\pi = \chi_\nu$. In that case the ratio of the matrix elements of Q^B_π and Q^B_ν reflect the F-spin conservation or mixing. The relation $\chi_\pi = \chi_\nu$, however, is not necessarily satisfied. According to the OAI mapping, the χ parameter varies with the shell-filling. If $\chi_\pi \neq \chi_\nu$, the difference between χ_π and χ_ν leads to an additional F-vector term other than that proportional to $Q^B_\pi - Q^B_\nu$. Therefore, we should be careful in seeing the F-spin conservation from the matrix elements of Q^B_π and Q^B_ν.

C Renormalization of Transition Densities

In this appendix we review the renormalization procedure in the evaluation of the transition densities in the method of Sagawa-Brown[59].

Let the Hartree-Fock (HF) single particle wavefunctions and the transition density between the HF state and the giant resonance (GR) states be given. The basic idea is an incorporation of the core polarization effect into the single particle wavefunctions. If a single particle state is denoted by $|j\rangle$ and the n-th GR state with the angular momentum λ by $|\omega^{(\lambda)}_n\rangle$, the renormalized single particle state is written as

$$|\tilde{j}\rangle = |j\rangle + \sum_{n,j'} a_{n,j'}(j) |\omega^{(\lambda)}_n \times j'; j\rangle. \tag{C.1}$$

Here $a_{n,j'}(j)$ represents the mixing amplitude evaluated by the perturbation. We will discuss this evaluation later. Then the renormalized transition density is calculated in the first-order perturbation as

$$\begin{aligned}
\langle \tilde{j}' \| T^{(\lambda)}(r) \| \tilde{j} \rangle &\simeq \langle j' \| T^{(\lambda)}(r) \| j \rangle + \sum_n \Big\{ a_{n,j'}(j) \langle j' \| T^{(\lambda)}(r) \| \omega^{(\lambda)}_n \times j'; j \rangle \\
&\qquad + a_{n,j}(j') \langle \omega^{(\lambda)}_n \times j; j' \| T^{(\lambda)}(r) \| j \rangle \Big\} \\
&= \langle j' \| T^{(\lambda)}(r) \| j \rangle + \sum_n \left\{ a_{n,j'}(j) \sqrt{\frac{2j+1}{2\lambda+1}} \langle 0 \| T^{(\lambda)}(r) \| \omega^{(\lambda)}_n \rangle \right. \\
&\qquad \left. + (-)^{\lambda+j-j'} a_{n,j}(j') \sqrt{\frac{2j'+1}{2\lambda+1}} \langle \omega^{(\lambda)}_n \| T^{(\lambda)}(r) \| 0 \rangle \right\},
\end{aligned} \tag{C.2}$$

where $|0\rangle$ denotes the HF vacuum and $T^{(\lambda)}$ does the transition operator with the rank λ as the spherical tensor.

Next we discuss the mixing amplitude $a_{n,j'}(j)$. In the derivation of the residual interaction from the Skyrme interaction, we take averages of

momentum-dependent terms of the interaction as an approximation. Then the Skyrme interaction only depends on the isoscalar (IS) nucleon density $\rho_{IS}(\mathbf{r})$ and the isovector (IV) nucleon density $\rho_{IV}(\mathbf{r})$. Therefore the residual interaction is written as

$$\begin{aligned} V_{res} &= \frac{1}{2}\frac{\delta^2 H_{Sk}}{\delta\rho_{IS}^2}\Big|_0 \left[\sum_i \delta(\mathbf{r}-\mathbf{r}_i)\right]\left[\sum_{i'}\delta(\mathbf{r}-\mathbf{r}_{i'})\right] \\ &+\frac{1}{2}\frac{\delta^2 H_{Sk}}{\delta\rho_{IV}^2}\Big|_0 \left[\sum_i \delta(\mathbf{r}-\mathbf{r}_i)\tau_z(i)\right]\left[\sum_{i'}\delta(\mathbf{r}-\mathbf{r}_{i'})\tau_z(i')\right], \quad \text{(C.3)} \end{aligned}$$

where in the expression

$$\frac{\delta^2 H_{Sk}}{\delta\rho_{IS}^2}\Big|_0 \quad \text{(C.4)}$$

the $|_0$ means the evaluation by the IS and IV densities of the HF state. In the above equation i and i' denotes indices of nucleons. The mixing amplitude is calculated in the perturbation theory as

$$a_{n,j'}(j) = \frac{\langle \omega_n^{(\lambda)} \times j'; j|V_{res}|j\rangle}{\epsilon_j - (\epsilon_{j'}+\omega_{\lambda,n})}, \quad \text{(C.5)}$$

where the excitation energy of the GR state measured from the HF state is expressed by $\omega_{\lambda,n}$.

Here we restrict ourselves to the isoscalar transition for the sake of simplicity. In order to evaluate the numerator of the right-handed side of Eq.(C.5), one of the delta functions in the first term of the right-handed side of Eq.(C.3) is taken to correspond the IS-GR mode, and the other to be the single particle transition mode from j to j'. Recalling the relation

$$\delta(\mathbf{r}-\mathbf{r}_i) = \frac{\delta(r-r_i)}{r r_i}\sum_{lm} Y_\mu^{(\lambda)\bullet}(\hat{\mathbf{r}})Y_\mu^{(\lambda)}(\hat{\mathbf{r}}_i), \quad \text{(C.6)}$$

where $\hat{\mathbf{r}}$ denotes the angular variables of $\mathbf{r}$, we obtain

$$\langle \omega_n^{(\lambda)} \times j'; jm|V_{res}|jm\rangle$$

$$\begin{aligned} &= \sum_{\mu,m'}(\lambda,\mu,j',m'|j,m)\int d^3r\,\frac{\delta^2 H_{Sk}}{\delta\rho_{IS}^2}\Big|_0 Y_\mu^{(\lambda)\bullet}(\hat{\mathbf{r}})\langle\omega_{\mu,n}^{(\lambda)}|\sum_i \frac{\delta(r-r_i)}{r r_i}Y^{(\lambda)}(\hat{\mathbf{r}}_i)|0\rangle \\ &\quad\times\sum_{\lambda'\mu'}Y_{\mu'}^{(\lambda')}(\hat{\mathbf{r}})\langle j'm'|\sum_{i'}\frac{\delta(r-r_{i'})}{r r_{i'}}Y^{(\lambda')\bullet}(\hat{\mathbf{r}}_{i'})|jm\rangle \\ &= \sum_{\mu,m'}(\lambda,\mu,j',m'|j,m)\int r^2dr\,\frac{\delta^2 H_{Sk}}{\delta\rho_{IS}^2}\Big|_0 \langle\omega_{\mu,n}^{(\lambda)}|\sum_i\frac{\delta(r-r_i)}{r^2}Y_\mu^{(\lambda)}(\hat{\mathbf{r}}_i)|0\rangle \\ &\quad\times\langle j'm'|\sum_{i'}\frac{\delta(r-r_{i'})}{r^2}Y_\mu^{(\lambda)\bullet}(\hat{\mathbf{r}}_{i'})|jm\rangle \\ &= \int r^2dr\,\frac{\delta^2 H_{Sk}}{\delta\rho_{IS}^2}\Big|_0 \frac{1}{\sqrt{2\lambda+1}}\langle\omega_n^{(\lambda)}\|\sum_i\frac{\delta(r-r_i)}{r^2}Y^{(\lambda)}(\hat{\mathbf{r}}_i)\|0\rangle \\ &\quad\times\frac{(-)^\lambda}{\sqrt{2j+1}}\langle j'\|\sum_{i'}\frac{\delta(r-r_{i'})}{r^2}Y^{(\lambda)}(\hat{\mathbf{r}}_{i'})\|j\rangle. \quad \text{(C.7)} \end{aligned}$$

The GR part of Eq.(C.7) is the sum of proton and neutron transition density to the n-th GR state,

$$\frac{1}{\sqrt{2\lambda+1}}\langle\omega_n^{(\lambda)}\|\sum_i\frac{\delta(r-r_i)}{r^2}Y^{(\lambda)}(\hat{\mathbf{r}}_i)\|0\rangle = \bar{\rho}_{\lambda,n}^{tr}(r). \quad \text{(C.8)}$$

The single particle part of Eq.(C.7) is evaluated as

$$\langle j'\|\sum_{i'}\frac{\delta(r-r_{i'})}{r^2}Y^{(\lambda)}(\hat{\mathbf{r}}_{i'})\|j\rangle = R_{j'}(r)R_j(r)\langle j'\|Y^{(\lambda)}\|j\rangle, \quad \text{(C.9)}$$

where $R_j(r)$ denotes the radial part of the single particle wavefunction of the orbit j. In the expression $\langle j'\|Y^{(\lambda)}\|j\rangle$ the radial integration is not included.

Here we define the following quantity

$$\langle V_{res}\rangle_{jj'} \equiv \int r^2dr\,\frac{\delta^2 H_{Sk}}{\delta\rho_{IS}^2}\Big|_0 \bar{\rho}_{\lambda,n}^{tr}(r)R_{j'}(r)R_j(r). \quad \text{(C.10)}$$

It is easily seen

$$\langle V_{res}\rangle_{jj'} = \langle V_{res}\rangle_{j'j}. \quad \text{(C.11)}$$

Substituting Eqs.(C.8), (C.9) and (C.10) into Eq.(C.7), we have

$$\langle \omega_n^{(\lambda)} \times j'; jm | V_{res} | jm \rangle = \frac{(-)^\lambda}{\sqrt{2j+1}} \langle j' \| Y^{(\lambda)} \| j \rangle \cdot \langle V_{res} \rangle_{jj'}. \tag{C.12}$$

Thus, we obtain for the mixing amplitude of Eq.(C.5),

$$a_{n,j'}(j) = \frac{(-)^\lambda}{\sqrt{2j+1}} \frac{\langle j' \| Y^{(\lambda)} \| j \rangle \cdot \langle V_{res} \rangle_{jj'}}{(\epsilon_j - \epsilon_{j'}) - \omega_{\lambda,n}}. \tag{C.13}$$

The mixing amplitudes for the isovector transitions are evaluated in the same manner, apart from the replacement of ρ_{IS} by ρ_{IV} and the insertion of τ_z into appropriate locations.

We further look into general features of the renormalized single particle transition densities, Eq.(C.2). By using Eq.(C.13), the renormalization terms caused by the n-th GR state is written as

$$\begin{aligned} & a_{n,j'}(j) \langle j' \| T^{(\lambda)}(r) \| \omega_n^{(\lambda)} \times j'; j \rangle + a_{n,j}(j') \langle \omega_n^{(\lambda)} \times j; j' \| T^{(\lambda)}(r) \| j \rangle \\ &= \frac{\langle V_{res} \rangle_{jj'}}{\sqrt{2\lambda+1}} \left\{ (-)^\lambda \frac{\langle j' \| Y^{(\lambda)} \| j \rangle \cdot \langle 0 \| T^{(\lambda)}(r) \| \omega_n^{(\lambda)} \rangle}{(\epsilon_j - \epsilon_{j'}) - \omega_{\lambda,n}} \right. \\ &\quad \left. + (-)^{j-j'} \frac{\langle j \| Y^{(\lambda)} \| j' \rangle \cdot \langle \omega_n^{(\lambda)} \| T^{(\lambda)}(r) \| 0 \rangle}{(\epsilon_{j'} - \epsilon_j) - \omega_{\lambda,n}} \right\}. \end{aligned} \tag{C.14}$$

Because

$$\langle j \| Y^{(\lambda)} \| j' \rangle = (-)^{j-j'} \langle j' \| Y^{(\lambda)} \| j \rangle \tag{C.15}$$

and

$$\langle 0 \| T^{(\lambda)}(r) \| \omega_n^{(\lambda)} \rangle = (-)^\lambda \langle \omega_n^{(\lambda)} \| T^{(\lambda)}(r) \| 0 \rangle, \tag{C.16}$$

which is satisfied when

$$T_\mu^{(\lambda)}(r)^\dagger = (-)^\mu \, T_{-\mu}^{(\lambda)}(r), \tag{C.17}$$

Eq.(C.14) is simplified as

$$\begin{aligned} & a_{n,j'}(j) \langle j' \| T^{(\lambda)}(r) \| \omega_n^{(\lambda)} \times j'; j \rangle + a_{n,j}(j') \langle \omega_n^{(\lambda)} \times j; j' \| T^{(\lambda)}(r) \| j \rangle \\ &= \frac{2\omega_{\lambda,n}}{(\epsilon_j - \epsilon_{j'})^2 - \omega_{\lambda,n}^2} \frac{\langle V_{res} \rangle_{jj'}}{\sqrt{2\lambda+1}} \langle j' \| Y^{(\lambda)} \| j \rangle \cdot \langle \omega_n^{(\lambda)} \| T^{(\lambda)}(r) \| 0 \rangle. \end{aligned} \tag{C.18}$$

In the actual calculation mentioned in Section 4, the HF result is used for the single particle energy ϵ_j. It is noted, however, that $(\epsilon_j - \epsilon_{j'})^2 \ll (\omega_n^{(\lambda)})^2$ in most cases. In fact, $|\epsilon_j - \epsilon_{j'}|$ is only a few MeV and $\omega_{\lambda,n}^{(2)}$ is at least 17MeV in our case. If we neglect $(\epsilon_j - \epsilon_{j'})^2$, Eq.(C.18) becomes

$$\begin{aligned} & a_{n,j'}(j) \langle j' \| T^{(\lambda)}(r) \| \omega_n^{(\lambda)} \times j'; j \rangle + a_{n,j}(j') \langle \omega_n^{(\lambda)} \times j; j' \| T^{(\lambda)}(r) \| j \rangle \\ &\simeq \frac{-2}{\omega_{\lambda,n}} \frac{\langle V_{res} \rangle_{jj'}}{\sqrt{2\lambda+1}} \langle j' \| Y^{(\lambda)} \| j \rangle \cdot \langle \omega_n^{(\lambda)} \| T^{(\lambda)}(r) \| 0 \rangle. \end{aligned} \tag{C.19}$$

When we assume the form

$$T_\mu^{(\lambda)}(r) = f(r) \sum_i e_i \frac{\delta(r - r_i)}{r^2} Y_\mu^{(\lambda)}(\hat{\mathbf{r}}_i), \tag{C.20}$$

where $f(r)$ is an appropriate function of r, and e_i represents the electric charge of the i-th particle, which is valid for the longitudinal transition, we have the relation,

$$\frac{1}{\sqrt{2\lambda+1}} \langle \omega_n^{(\lambda)} \| T^{(\lambda)}(r) \| 0 \rangle = e f(r) \rho_{\lambda,n}^{tr}(r), \tag{C.21}$$

where $\rho_{\lambda,n}^{tr}(r)$ is the transition charge density. On the other hand, the unrenormalized single particle transition density for the proton orbits j and j' can be written in the following way,

$$\langle j' \| T^{(\lambda)}(r) \| j \rangle = e f(r) R_j(r) R_{j'}(r) \langle j' \| Y^{(\lambda)} \| j \rangle. \tag{C.22}$$

$R_j(r)$ is the radial part of the single particle wavefunction of the orbit j, obtained by the HF calculation.

Because of Eqs.(C.18), (C.21) and (C.22), we obtain for the proton single particle transition,

$$\langle \tilde{j}' \| T^{(\lambda)}(r) \| \tilde{j} \rangle \simeq ef(r) \langle j' \| Y^{(\lambda)} \| j \rangle [R_j(r) R_{j'}(r) - \sum_n \frac{2\omega_{\lambda,n}}{(\epsilon_j - \epsilon_{j'})^2 - \omega_{\lambda,n}^2} \langle V_{res} \rangle_{jj'} \rho^{tr}_{\lambda,n}(r)]. \quad \text{(C.23)}$$

Besides the factor $\langle V_{res} \rangle_{jj'}$, this formula is derived in Ref.[83]. Therefore, due to the Siegert's theorem[66], renormalized electric γ-transition matrix element is proportional to

$$\int r^2 dr \langle \tilde{j}' \| T^{(\lambda)}(r) \| \tilde{j} \rangle = \langle j' \| Y^{(\lambda)} \| j \rangle \left[\int r^2 dr f(r) R_j(r) R_{j'}(r) - \sum_n \frac{2\omega_{\lambda,n}}{(\epsilon_j - \epsilon_{j'})^2 - \omega_{\lambda,n}^2} \langle V_{res} \rangle_{jj'} \int r^2 dr f(r) \rho^{tr}_{\lambda,n}(r) \right]. \quad \text{(C.24)}$$

Remark the close relation between the Coulomb form factors and the electric γ-transition probabilities. We can obtain the electric γ-transition probabilities from the Coulomb form factors carrying the same angular momentum by taking the photon-point limit ($q \to 0$). Thus the j-dependent effective charges for protons are defined from the ratio

$$\sum_n \frac{2\omega_{\lambda,n}}{(\epsilon_j - \epsilon_{j'})^2 - \omega_{\lambda,n}^2} \langle V_{res} \rangle_{jj'} \frac{\int r^2 dr f(r) \rho^{tr}_{\lambda,n}(r)}{\int r^2 dr f(r) R_j(r) R_{j'}(r)}. \quad \text{(C.25)}$$

In analogy, the j-dependent effective charges for neutrons are defined by the same formula (C.25). If we use the approximation of Eq.(C.19), the ratio becomes

$$\left[\sum_n \frac{-2}{\omega_{\lambda,n}} \int r^2 dr f(r) \rho^{tr}_{\lambda,n}(r) \right] \frac{\langle V_{res} \rangle_{jj'}}{\int r^2 dr f(r) R_j(r) R_{j'}(r)}. \quad \text{(C.26)}$$

The j-dependence mainly comes from the last factor in Eq.(C.26). Thus the j-dependence is expected to be small when $R_j(r) R_{j'}(r)$ gives dominant

variation with r in both of the integrated functions in the numerator and the denominator of that factor.

D Feshbach's Projection Method

The Feshbach's projection method[75] is surveyed in this appendix.

We consider a proper truncation of a space. The truncated subspace is called P-space, and the projection operator onto the P-space is denoted by $\hat{P}$. The space outside the P-space is called Q-space, and we define

$$\hat{Q} = 1 - \hat{P}. \tag{D.1}$$

We hold the relation as usual,

$$\hat{P}^2 = \hat{P}, \quad \hat{Q}^2 = \hat{Q}. \tag{D.2}$$

If a hamiltonian in the full space, denoted by H, is given, the Schrödinger equation is written as

$$(E - H)|\ \rangle = 0, \tag{D.3}$$

where $|\ \rangle$ represents an arbitrary energy eigenstate and E stands for its eigenvalue. By using Eq.(D.1),

$$(E - H)(\hat{P} + \hat{Q})|\ \rangle = 0. \tag{D.4}$$

Multiplying $\hat{P}$ and $\hat{Q}$ from the left, we obtain

$$(E - H_{PP})\hat{P}|\ \rangle = H_{PQ}|\ \rangle, \tag{D.5}$$

$$(E - H_{QQ})\hat{Q}|\ \rangle = H_{QP}|\ \rangle. \tag{D.6}$$

Here we use the notation

$$H_{PP} = \hat{P}H\hat{P}, \quad H_{PQ} = \hat{P}H\hat{Q}, \quad H_{QP} = \hat{Q}H\hat{P}, \quad H_{QQ} = \hat{Q}H\hat{Q}. \tag{D.7}$$

Therefore we can formally eliminate the influence of the Q-space,

$$(E - \tilde{H}_{PP})\hat{P}|\ \rangle = 0, \tag{D.8}$$

where

$$\tilde{H}_{PP} = H_{PP} + H_{PQ}\frac{1}{E - H_{QQ}}H_{QP}. \tag{D.9}$$

The above equation (D.8) works only in the P space.

References

[1] A. Bohr, Mat. Fys. Medd. Dan. Vid. Selsk. 26, no. 14 (1952);
A. Bohr and B. R. Mottelson, Mat. Fys. Medd. Dan. Vid. Selsk. 27, no. 16 (1953).

[2] F. Iachello and A. Arima, The interacting boson model (Cambridge, 1987).

[3] O. Scholten, F. Iachello and A. Arima, Ann. Phys. 115(1978)325.

[4] A. Arima and F. Iachello, Ann. Phys. 99(1976)253;
A. Arima and F. Iachello, Ann. Phys. 111(1978)201;
A. Arima and F. Iachello, Ann. Phys. 123(1979)468.

[5] T. Otsuka, A. Arima and F. Iachello, Nucl. Phys. A309(1978)1;
A. Arima, T. Otsuka, F. Iachello and I. Talmi, Phys. Lett. B66(1977)205;
T. Otsuka, A. Arima, F. Iachello and I. Talmi, Phys. Lett. B76(1978)139.

[6] T. Otsuka, Ph. D. thesis (University of Tokyo, 1979).

[7] F. Iachello, Nucl. Phys. A358(1981)89c.

[8] A. E. L. Dieperink, Prog. Part. Nucl. Phys. 9(1983)121.

[9] T. Suzuki and D. J. Rowe, Nucl. Phys. A289(1977)461;
N. Lo Iudice and F. Palumbo, Phys. Rev. Lett. 41(1978)1532;
N. Lo Iudice and F. Palumbo, Nucl. Phys. A326(1979)193;
R. R. Hilton, Z. Phys. A316(1984)121;
E. Lipparini and S. Stringari, Phys. Lett. B130(1983)139.

[10] D. Bohle *et al.*, Phys. Lett. B137(1984)27;
D. Bohle, G. Küchler, A. Richter and W. Steffen, Phys. Lett. B148(1984)260;
U. E. P. Berg *et al.*, Phys. Lett. B149(1984)59;
C. Djalali *et al.*, Phys. Lett. B164(1985)269.

[11] A. Richter, Nucl. Phys. A522(1991)139c.

[12] F. Iachello, Phys. Rev. Lett. 53(1984)1427.

[13] T. Otsuka and J. N. Ginocchio, Phys. Rev. Lett. 54(1985)777.

[14] A. Faessler, Nucl. Phys. 85(1966)653;
V. Maruhn-Rezwani, W. Greiner and J. A. Maruhn, Phys. Lett. B57(1975)109.

[15] A. Faessler and R. Nojarov, Phys. Lett. B166(1986)367;
R. Nojarov and A. Faessler, J. Phys. G13(1987)337.

[16] K. Heyde and J. Sau, Phys. Rev. C33(1986)1050.

[17] S. A. A. Eid, W. D. Hamilton and J. P. Elliott, Phys. Lett. B166(1986)267.

[18] S. P. Collins *et al.*, J. Phys. G15(1989)321.

[19] K. P. Lieb *et al.*, Phys. Lett. B215(1988)50.

[20] M. Pignanelli *et al.*, Phys. Lett. B202(1988)470;
R. de Leo *et al.*, Phys. Lett. B226(1989)5.

[21] W. D. Hamilton, A. Irbäck and J. P. Elliott, Phys. Rev. Lett. 53(1984)2469.

[22] L. Zamick, Phys. Rev. C31(1985)1955;
D. C. Zheng, L. Zamick, E. Moya de Guerra and A. Richter, Phys. Rev. C42(1990)1408.

[23] H. Liu and L. Zamick, Nucl. Phys. A467(1987)29;
H. Liu and L. Zamick, Phys. Rev. C36(1987)2064.

[24] D. Bonatsos, Interacting Boson Models of Nuclear Structure, p.86 (Oxford, 1988).

[25] N. Bendjaballah *et al.*, Nucl. Phys. A284(1977)513.

[26] H. Junde *et al.*, Nucl. Data Sheets 51(1987)1.

[27] M. Sambataro, O. Scholten, A. E. L. Dieperink and G. Piccitto, Nucl. Phys. A423(1984)333.

[28] J. P. Elliott, Proc. Roy. Soc. A245(1958)128;
J. P. Elliott, Proc. Roy. Soc. A245(1958)562;
J. P. Elliott and M. Harvey, Proc. Roy. Soc. A272(1963)557.

[29] O. Scholten *et al.*, Nucl. Phys. A438(1985)41.

[30] P. van Isacker, K. Heyde, J. Jolie and A. Sevrin, Ann. Phys. 171(1986)253.

[31] G. Hartung *et al.*, Phys. Lett. B221(1989)109.

[32] J. Takamatsu *et al.*, Colloque de Physique C6(1990)423.

[33] A. Richter, private communication.

[34] S. J. Robinson *et al.*, J. Phys. G12(1986)903.

[35] S. T. Ahmad *et al.*, J. Phys. G15(1989)93.

[36] A. R. H. Subber *et al.*, J. Phys. G12(1986)881.

[37] J. D. McCullen, B. F. Bayman and L. Zamick, Phys. Rev. 134(1964)B515;
J. N. Ginocchio, Phys. Rev. 144(1966)952.

[38] J. Vervier, Nucl. Phys. 78(1966)497.

[39] S. Cohen *et al.*, Phys. Rev. 160(1967)903;
N. Auerbach, Phys. Rev. 163(1967)1203.

[40] J. B. McGrory, Phys. Rev. 160(1967)915.

[41] H. Horie and K. Ogawa, Prog. Theor. Phys. 46(1971)439;
H. Horie and K. Ogawa, Nucl. Phys. A216(1973)407.

[42] B. J. Raz and M. Soga, Phys. Rev. Lett. 15(1965)924;
T. Engeland and E. Osnes, Phys. Lett. 20(1966)424;
N. Auerbach, Phys. Lett. B24(1967)260;
K. Lips and M. T. McEllistrem, Phys. Rev. C1(1970)1009;
T. Oda, K. Muto and H. Horie, Lett. Nuovo Cimento 18(1977)549;
A. Yokoyama, T. Oda and H. Horie, Prog. Theor. Phys. 60(1978)427.

[43] T. Motoba and K. Ogawa, Prog. Theor. Phys. 51(1974)173;
T. Motoba, Prog. Theor. Phys. 54(1975)429;

H. G. Benson and I. P. Johnstone, Can. J. Phys. 53(1975)1715;
R. B. M. Mooy and P. W. M. Glaudemans, Z. Phys. A312(1983)59.

[44] T. T. S. Kuo and G. E. Brown, Nucl. Phys. A114(1968)241.

[45] T. Motoba and K. Itonaga, Suppl. Prog. Theor. Phys. 65(1979)136.

[46] E. Pasquini and A. Zuker, *in* Physics of Medium-Light Nuclei, *ed. by* P. Blasi and R. A. Ricci (Editrice Compositori, 1978).

[47] A. Poves and A. Zuker, Phys. Rep. 70(1981)235;
J. B. McGrory, B. H. Wildenthal and E. C. Halbert, Phys. Rev. C2(1970)186;
J. B. McGrory, Phys. Rev. C8(1973)693.

[48] G. Oberlechner and J. Richert, Nucl. Phys. A191(1972)577.

[49] Z. Enchen *et al.*, Nucl. Data Sheets 44(1985)463.

[50] T. W. Burrows and M. R. Bhat, Nucl. Data Sheets 47(1986)1.

[51] W. Gongqing, Z. Jiabi and Z. Jingen, Nucl. Data Sheets 50(1987)255.

[52] L. K. Peker, Nucl. Data Sheets 61(1990)189.

[53] H. Junde *et al.*, Nucl. Data Sheets 58(1989)677.

[54] K. Shimizu and A. Arima, Nucl. Phys. A227(1974)357.

[55] S. S. Rosenblum and W. A. Steyert, Phys. Lett. B55(1975)450.

[56] I. S. Towner, Phys. Rep. 155(1987)263.

[57] A. Arima, K. Shimizu, W. Bentz and H. Hyuga, *in* Advances in Nuclear Physics, *ed. by* J. W. Negele and E. Vogt, vol.18, p.1 (Plenum, 1988).

[58] P. Halse, Phys. Rev. C41(1990)2340.

[59] H. Sagawa and B. A. Brown, Nucl. Phys. A430(1984)84.

[60] N. van Giai and H. Sagawa, Nucl. Phys. A371(1981)1;
N. van Giai and H. Sagawa, Phys. Lett. B106(1981)379.

[61] G. F. Bertsch and F. S. Tsai, Phys. Rep. 18(1975)125.

[62] L. H. Chan *et al.*, Phys. Rev. 141(1966)1298;
A. Bohr and B. R. Mottelson, Nuclear Structure vol.1, p.386 (Benjamin, 1969).

[63] L. J. Tassie and F. C. Barker, Phys. Rev. 111(1958)940.

[64] R. J. Peterson, H. Theissen and W. J. Alston, Nucl. Phys. A153(1970)610.

[65] J. Heisenberg, J. S. McCarthy and I. Sick, Nucl. Phys. A164(1971)353.

[66] T. de Forest Jr. and J. D. Walecka, Adv. Phys. 15(1966)1.

[67] J. W. Lightbody Jr. *et al.*, Phys. Rev. C27(1983)113.

[68] Phan-Xuan-Ho, J. Bellicard and Ph. Leconte, Nucl. Phys. A210(1973)189.

[69] J. Heisenberg, *in* Advances in Nuclear Physics, *ed. by* J. W. Negele and E. Vogt, vol.12, p.61 (Plenum, 1981).

[70] K. Nakayama and W. G. Love, Phys. Rev. C38(1988)51.

[71] G. Bertsch, J. Borysowicz, H. McManus and W. G. Love, Nucl. Phys. A284(1977)399.

[72] H. V. von Geramb, L. Rikus and N. Nakano, *in* Proceeding of the 1983 RCNP International Conference on Light Ion Reaction Mechanism, *ed. by* H. Ogata *et al.* (Osaka Univ. Press, 1983).

[73] J. Takamatsu, Ph. D. thesis (Tohoku University, 1991).

[74] T. Otsuka, Nucl. Phys. A507(1990)129c;
J. Retamosa, J. M. Udías, A. Poves and E. Moya de Guerra, Nucl. Phys. A511(1990)221.

[75] H. Feshbach, Ann. Phys. 19(1962)287.

[76] P. D. Duval, S. Pittel, B. R. Barrett and C. H. Druce, Phys. Lett. B129(1983)289;
C. H. Druce, S. Pittel, B. R. Barrett and P. D. Duval, Ann. Phys. 176(1987)114.

[77] O. Scholten, Phys. Rev. C28(1983)1783.

[78] T. Mizusaki, T. Otsuka and M. Sugita, to be published.

[79] O. Scholten, K. Heyde, P. van Isacker and T. Otsuka, Phys. Rev. C32(1985)1729;
A. R. H. Subber *et al.*, J. Phys. G1487.

[80] O. Scholten, Phys. Lett. B127(1983)144.

[81] A. Arima and M. Ichimura, Prog. Theor. Phys. 36(1966)296.

[82] S. Pittel, P. D. Duval and B. R. Barrett, Ann. Phys. 144(1982)168.

[83] M. Harvey and F. C. Khanna, Nucl. Phys. A152(1970)588;
M. Harvey and F. C. Khanna, Nucl. Phys. A155(1970)337;
F. Petrovich, H. McManus, J. Borysowicz and G. R. Hammerstein, Phys. Rev. C16(1977)839.

Tables and Figures

Table 1: The largest dimensions in the shell model calculation with $k \leq 2$ configurations, both within the M-scheme and the JT-scheme. In the M-scheme, the number of the $M = 0$ bases is the largest in any even-mass nucleus, while that of the $M = \frac{1}{2}$ bases in any odd-mass nucleus. The spin-parity and isospin in which the dimension within the JT-scheme is the largest are also shown.

nucleus	M-scheme	J^P	T	JT-scheme
^{56}Ni	1,353	3^+	1	103
^{55}Co	4,717	$(\frac{9}{2})^-$	$\frac{1}{2}$	347
^{57}Ni	7,890	$(\frac{7}{2})^-$	$\frac{1}{2}$	619
^{54}Fe	10,620	4^+	1	891
^{58}Ni	29,792	4^+	1	2,780
^{56}Fe	162,358	5^+	2	15,457
^{54}Cr	195,334	5^+	3	20,074
^{52}Ti	52,624	4^+	4	6,207

Table 2: Probabilities of the configuration k in each wavefunction.

nucleus	state	$k = 0$ [%]	$k = 1$ [%]	$k = 2$ [%]
^{56}Ni	0_1^+	63.4	0.0	36.6
^{55}Co	$(\frac{7}{2})_1^-$	62.9	4.5	32.5
^{57}Ni	$(\frac{9}{2})_1^-$	60.9	6.3	32.8
	$(\frac{5}{2})_1^-$	61.4	8.7	29.9
	$(\frac{1}{2})_1^-$	59.4	7.3	33.3
^{54}Fe	0_1^+	62.2	7.0	30.8
	2_1^+	60.7	10.1	29.2
	4_1^+	61.3	9.7	29.0
	6_1^+	61.4	9.5	29.1
^{58}Ni	0_1^+	57.7	9.1	33.1
	0_2^+	5.4	1.4	93.2
	0_3^+	53.6	14.9	31.5
	1_1^+	55.9	16.4	27.7
	1_2^+	55.2	14.4	30.4
	2_1^+	55.2	12.0	32.8
	2_2^+	53.2	13.9	32.9
	2_3^+	7.2	2.2	90.6
	2_4^+	53.4	16.4	30.3
	3_1^+	47.7	24.6	27.6
	4_1^+	55.3	17.5	27.2

(to be continued)

Table 2: (continued)

nucleus	state	$k=0$ [%]	$k=1$ [%]	$k=2$ [%]
^{56}Fe	0_1^+	55.7	17.7	26.6
	0_2^+	50.8	26.8	22.3
	1_1^+	51.4	26.0	22.6
	1_2^+	50.6	25.9	23.5
	1_3^+	52.4	24.2	23.4
	2_1^+	53.6	21.5	25.0
	2_2^+	47.6	28.3	24.1
	2_3^+	52.1	24.2	23.7
	2_4^+	20.8	48.4	30.8
	3_1^+	26.1	47.4	26.5
	4_1^+	50.7	26.0	23.3
	4_2^+	52.7	23.6	23.7
	6_1^+	55.5	20.4	24.1
^{54}Cr	0_1^+	56.5	20.6	22.9
	0_2^+	48.2	30.7	21.1
	1_1^+	52.6	27.5	19.9
	1_2^+	53.3	26.3	20.3
	1_3^+	46.3	33.3	20.4
	2_1^+	53.5	25.4	21.1
	2_2^+	47.8	30.6	21.6
	2_3^+	55.6	22.5	21.9
	2_4^+	45.8	33.2	21.0
	4_1^+	50.2	30.3	19.5
	4_2^+	54.5	24.5	21.1
	6_1^+	53.6	25.7	20.7
^{52}Ti	0_1^+	62.7	14.8	22.5
	1_1^+	57.7	25.9	16.4
	1_2^+	53.7	29.7	16.6
	1_3^+	50.0	31.9	18.1
	2_1^+	60.3	20.2	19.5
	2_2^+	53.5	25.8	20.6
	2_3^+	54.6	27.9	17.4
	2_4^+	25.5	50.3	24.2
	3_1^+	48.8	33.6	17.6
	4_1^+	57.8	25.2	17.0
	6_1^+	65.5	17.6	16.9

Table 3: Experimental and calculated excitation energies of the yrast states in ^{56}Fe.

state	Cal. [MeV]	Exp.*[MeV]
0_1^+	0.0	0.0
1_1^+	3.082	3.120
2_1^+	0.943	0.847
3_1^+	3.549	3.445
4_1^+	2.301	2.085
5_1^+	4.367	—
6_1^+	3.293	3.389
7_1^+	4.745	4.701
8_1^+	5.318	5.256

*) Taken from Ref.[26].

Table 4: Matrix elements of $Q_\rho[fm^2]$ ($\rho = \pi, \nu$), $B(E2)$ values ($[e^2fm^4]$) or $E2$ static moments ($[efm^2]$) in ^{56}Fe. The i (f) denotes initial (final) state. In the 'Cal.(A)' values the j-independent effective charges are employed, together with the harmonic oscillator single particle wavefunctions. The 'Cal.(B)' values are calculated by the method of Sagawa-Brown.

i	f	$\langle f\|\|Q_\pi\|\|i\rangle$	$\langle f\|\|Q_\nu\|\|i\rangle$	Cal.(A)	Cal.(B)	Exp.*
2_1^+	0_1^+	13.76	14.86	213.1	164.8	214 ± 8
2_2^+	0_1^+	−0.58	6.49	5.1	2.7	6 +8 −6
2_3^+	0_1^+	−0.50	−1.14	0.6	0.6	1.0 ± 0.1
2_4^+	0_1^+	6.36	−0.09	15.5	17.2	10 ± 5
2_5^+	0_1^+	1.60	0.72	1.7	1.3	5 ± 4
2_6^+	0_1^+	0.53	1.58	0.9	0.8	—
2_7^+	0_1^+	1.38	−5.37	1.7	0.6	1.8 ± 0.4
2_1^+	2_1^+	−16.03	−17.35	−28.8**	−25.4**	−23 ± 3**
2_2^+	2_1^+	3.45	−0.34	4.1	4.6	31 ± 14
2_3^+	2_1^+	2.90	5.87	17.5	13.7	17 ± 5
2_4^+	2_1^+	3.98	5.80	23.3	18.0	7 ± 5
4_1^+	2_1^+	21.66	23.23	291.6	229.6	305 ± 64

*) Taken from Ref.[26], **) Quadrupole moment.

Table 5: Matrix elements of $Q_\rho[fm^2]$ ($\rho = \pi, \nu$), $B(E2)$ values ($[e^2fm^4]$) or $E2$ static moments ($[efm^2]$) in ^{54}Cr. See the caption of Table 4 for the calculated values.

i	f	$\langle f\|\|Q_\pi\|\|i\rangle$	$\langle f\|\|Q_\nu\|\|i\rangle$	Cal.(A)	Cal.(B)	Exp.*
2_1^+	0_1^+	14.21	15.18	225.1	179.1	174 ± 3
2_2^+	0_1^+	0.61	2.41	1.8	1.2	11 ± 5
2_3^+	0_1^+	4.61	−1.56	5.1	6.8	—
2_4^+	0_1^+	0.24	5.91	6.4	4.4	—
2_1^+	2_1^+	−15.35	−16.31	−27.4**	−24.5**	−21 ± 8**
2_2^+	2_1^+	8.45	10.27	88.8	71.9	109 ± 36
4_1^+	2_1^+	22.55	21.81	291.4	237.6	303 ± 97
6_1^+	4_1^+	24.46	24.36	242.7	196.8	218 ± 61

*) Taken from Ref.[51], **) Quadrupole moment.

Table 6: Matrix elements of $Q_\rho[fm^2]$ ($\rho = \pi, \nu$), $B(E2)$ values ($[e^2fm^4]$) or $E2$ static moments ($[efm^2]$) in ^{52}Ti. See the caption of Table 4 for the calculated values.

i	f	$\langle f\|\|Q_\pi\|\|i\rangle$	$\langle f\|\|Q_\nu\|\|i\rangle$	Cal.(A)	Cal.(B)	Exp.*
2_1^+	0_1^+	8.89	14.98	134.4	100.2	138 + 104 − 92
2_2^+	0_1^+	−5.46	−0.18	12.2	13.7	31 + 23 − 14
2_3^+	0_1^+	−3.91	−0.14	6.3	6.3	—
2_4^+	0_1^+	−3.63	8.08	1.0	0.05	—
2_1^+	2_1^+	−3.56	−7.78	−9.1**	−7.5**	—
2_2^+	2_1^+	−7.27	−13.62	100.7	74.2	—
2_3^+	2_1^+	6.36	10.88	70.0	53.7	—
2_4^+	2_1^+	2.76	2.23	6.9	7.1	—
4_1^+	2_1^+	−16.09	−17.71	164.4	134.0	—

*) Taken from Ref.[53], **) Quadrupole moment.

Table 7: Matrix elements of $Q_\rho[fm^2]$ ($\rho = \pi, \nu$), $B(E2)$ values ($[e^2fm^4]$) or $E2$ static moments ($[efm^2]$) in ^{54}Fe. See the caption of Table 4 for the calculated values.

i	f	$\langle f\|\|Q_\pi\|\|i\rangle$	$\langle f\|\|Q_\nu\|\|i\rangle$	Cal.(A)	Cal.(B)	Exp.*
2_1^+	0_1^+	12.06	3.20	78.1	73.3	128 $\pm$ 5
2_1^+	2_1^+	-13.36	-3.88	-16.8**	-16.4**	-5 ± 14**

*) Taken from Ref.[51], **) Quadrupole moment.

Table 8: Matrix elements of $Q_\rho[fm^2]$ ($\rho = \pi, \nu$), $B(E2)$ values ($[e^2fm^4]$) or $E2$ static moments ($[efm^2]$) in ^{58}Ni. See the caption of Table 4 for the calculated values.

i	f	$\langle f\|\|Q_\pi\|\|i\rangle$	$\langle f\|\|Q_\nu\|\|i\rangle$	Cal.(A)	Cal.(B)	Exp.*
2_1^+	0_1^+	4.73	15.11	81.7	51.6	135.0 $\pm$ 3.2
2_2^+	0_1^+	2.48	4.65	11.7	9.0	0.4 $\pm$ 0.1
2_3^+	0_1^+	-1.87	2.72	0.01	0.1	—
2_1^+	2_1^+	-4.21	-14.63	-14.4**	-11.3**	-10 $\pm$ 6**

*) Taken from Ref.[52], **) Quadrupole moment.

Table 9: Matrix elements of L_ρ and S_ρ ($\rho = \pi, \nu$), $B(M1)$ values ($[\mu_N^2]$) or $M1$ static moments ($[\mu_N]$) in ^{56}Fe.

i	f	$\langle f\|\|L_\pi\|\|i\rangle$	$\langle f\|\|S_\pi\|\|i\rangle$	$\langle f\|\|L_\nu\|\|i\rangle$	$\langle f\|\|S_\nu\|\|i\rangle$	Cal.	Exp.*
2_1^+	2_1^+	2.70	0.24	2.44	0.09	1.17**	1.20 $\pm$ 0.20**
2_2^+	2_1^+	-1.74	-0.19	1.85	0.09	0.28	0.23 $\pm$ 0.07
2_3^+	2_1^+	0.12	0.04	-0.25	0.10	0.00	0.07 $\pm$ 0.01
2_4^+	2_1^+	1.28	0.14	-1.44	0.02	0.13	0.11 $\pm$ 0.05
1_1^+	0_1^+	0.02	0.04	-0.17	0.11	0.00	$< 1. \times 10^{-5}$
1_2^+	0_1^+	0.53	0.07	-0.61	0.01	0.04	0.05 $\pm$ 0.01
1_3^+	0_1^+	-0.83	-0.08	0.88	0.03	0.09	—

*) Taken from Ref.[26], **) Magnetic moment.

Table 10: Matrix elements of L_ρ and S_ρ ($\rho = \pi, \nu$), $B(M1)$ values ($[\mu_N^2]$) or $M1$ static moments ($[\mu_N]$) in ^{54}Cr.

i	f	$\langle f\|\|L_\pi\|\|i\rangle$	$\langle f\|\|S_\pi\|\|i\rangle$	$\langle f\|\|L_\nu\|\|i\rangle$	$\langle f\|\|S_\nu\|\|i\rangle$	Cal.	Exp.*
2_1^+	2_1^+	2.80	0.29	2.28	0.11	1.24**	1.12 $\pm$ 0.20**
2_2^+	2_1^+	0.17	−0.00	−0.04	−0.13	0.01	0.02 $\pm$ 0.01
2_3^+	2_1^+	−1.74	−0.22	1.88	0.07	0.30	$>$ 0.1
2_4^+	2_1^+	−1.37	−0.23	1.55	0.05	0.21	—
1_1^+	0_1^+	−0.37	−0.07	0.52	−0.07	0.02	—
1_2^+	0_1^+	0.07	0.04	−0.22	0.11	0.00	—
1_3^+	0_1^+	−1.13	−0.12	1.12	0.13	0.23	—

*) Taken from Ref.[51], **) Magnetic moment.

Table 11: Matrix elements of L_ρ and S_ρ ($\rho = \pi, \nu$), $B(M1)$ values ($[\mu_N^2]$) or $M1$ static moments ($[\mu_N]$) in ^{52}Ti.

i	f	$\langle f\|\|L_\pi\|\|i\rangle$	$\langle f\|\|S_\pi\|\|i\rangle$	$\langle f\|\|L_\nu\|\|i\rangle$	$\langle f\|\|S_\nu\|\|i\rangle$	Cal.	Exp.*
2_1^+	2_1^+	1.74	0.22	3.21	0.30	0.65**	—
2_2^+	2_1^+	−1.47	−0.25	1.65	0.07	0.25	$0.56 + 0.41 - 0.25$
2_3^+	2_1^+	−1.11	−0.10	0.66	0.55	0.29	$>$ 0.16
2_4^+	2_1^+	−1.21	−0.15	1.57	−0.21	0.07	—
1_1^+	0_1^+	0.33	0.04	−0.19	−0.18	0.05	—
1_2^+	0_1^+	−0.09	0.02	−0.11	0.18	0.01	—
1_3^+	0_1^+	0.75	0.11	−0.90	0.04	0.08	—

*) Taken from Ref.[53], **) Magnetic moment.

Table 12: Matrix elements of L_ρ and S_ρ ($\rho = \pi, \nu$), $B(M1)$ values ($[\mu_N^2]$) or $M1$ static moments ($[\mu_N]$) in ^{55}Co.

i	f	$\langle f\|\|L_\pi\|\|i\rangle$	$\langle f\|\|S_\pi\|\|i\rangle$	$\langle f\|\|L_\nu\|\|i\rangle$	$\langle f\|\|S_\nu\|\|i\rangle$	Cal.	Exp.*
$(\frac{7}{2})_1^-$	$(\frac{7}{2})_1^-$	9.51	1.23	0.38	0.11	3.96**	4.822 ± 0.003**

*) Taken from Ref.[49], **) Magnetic moment.

Table 13: Matrix elements of L_ρ and S_ρ ($\rho = \pi, \nu$), $B(M1)$ values ($[\mu_N^2]$) or $M1$ static moments ($[\mu_N]$) in ^{57}Ni.

i	f	$\langle f\|\|L_\pi\|\|i\rangle$	$\langle f\|\|S_\pi\|\|i\rangle$	$\langle f\|\|L_\nu\|\|i\rangle$	$\langle f\|\|S_\nu\|\|i\rangle$	Cal.	Exp.*
$(\frac{3}{2})_1^-$	$(\frac{3}{2})_1^-$	0.08	0.08	2.70	1.01	−0.63**	-0.88 ± 0.06**
$(\frac{5}{2})_1^-$	$(\frac{3}{2})_1^-$	0.02	−0.05	0.16	−0.13	0.001	0.026 ± 0.003
$(\frac{1}{2})_1^-$	$(\frac{3}{2})_1^-$	0.07	−0.06	0.82	−0.84	0.27	$<$ 0.34

*) Taken from Ref.[50], **) Magnetic moment.

Table 14: Excitation energies and transition strengths of the GQR states adopted for the calculation of the core polarization effect. The shown transition strengths are the sums about the states classified as having the same type of transition density.

Ex[MeV]	$B(E2)[e^2fm^4]$
16.69	800.9
21.83	29.3
24.64	93.4
25.60	38.7
27.19	9.4
27.69	13.2
29.77	35.2
30.21	31.3
30.93	67.5
31.86	284.3

Table 15: j-dependent effective charges evaluated by the method of Sagawa-Brown.

ρ	j	j'	$e_\rho^{eff}(j,j')$
π	$0f_{7/2}$	$0f_{7/2}$	1.354
	$0f_{7/2}$	$0f_{5/2}$	1.482
	$0f_{7/2}$	$1p_{3/2}$	1.488
	$0f_{5/2}$	$0f_{5/2}$	1.336
	$0f_{5/2}$	$1p_{3/2}$	1.436
	$0f_{5/2}$	$1p_{1/2}$	1.411
	$1p_{3/2}$	$1p_{3/2}$	1.341
	$1p_{3/2}$	$1p_{1/2}$	1.343
ν	$0f_{7/2}$	$0f_{7/2}$	0.677
	$0f_{7/2}$	$0f_{5/2}$	0.841
	$0f_{7/2}$	$1p_{3/2}$	0.788
	$0f_{5/2}$	$0f_{5/2}$	0.643
	$0f_{5/2}$	$1p_{3/2}$	0.712
	$0f_{5/2}$	$1p_{1/2}$	0.690
	$1p_{3/2}$	$1p_{3/2}$	0.601
	$1p_{1/2}$	$1p_{3/2}$	0.604

Table 16: Overlaps between the $\tilde{S}\tilde{D}$-states and the eigenstates of ^{56}Fe.

state	$\|J^P_S(\tilde{S}^2)\rangle$	$\|J^P_S(\tilde{S}\tilde{D})\rangle$	$\|J^P_S(\tilde{D}^2)\rangle$	$\|J^P_M(\tilde{S}\tilde{D})\rangle$	$\|J^P_M(\tilde{D}^2)\rangle$	$\tilde{S}\tilde{D}$-prob.
0^+_1	58.0 %		28.8 %			86.8 %
0^+_2	0.0 %		0.3 %			0.4 %
1^+_1					0.0 %	0.0 %
1^+_2					16.5 %	16.5 %
1^+_3					43.6 %	43.6 %
2^+_1		64.4 %	13.9 %	0.0 %		78.3 %
2^+_2		0.0 %	0.9 %	28.4 %		29.3 %
2^+_3		1.0 %	0.9 %	0.2 %		2.1 %
2^+_4		0.0 %	0.9 %	15.1 %		16.0 %
2^+_5		0.1 %	4.1 %	3.5 %		7.8 %
2^+_6		0.2 %	0.1 %	0.1 %		0.5 %
3^+_1					8.0 %	8.0 %
3^+_2					0.1 %	0.1 %
4^+_1			36.9 %			36.9 %
4^+_2			0.3 %			0.3 %

Table 17: Probabilities of $|2^+_{MSR}\rangle$ and $|1^+_{MSR}\rangle$ components in eigenfunctions of ^{56}Fe.

state	Ex[MeV]	$\|2^+_{MSR}\rangle$ [%]
2^+_1	0.943	0.0
2^+_2	2.807	30.8
2^+_3	2.974	0.2
2^+_4	3.287	16.5
2^+_5	3.563	2.4
2^+_6	3.855	0.0

state	Ex[MeV]	$\|1^+_{MSR}\rangle$ [%]
1^+_1	3.082	0.1
1^+_2	3.477	9.1
1^+_3	3.525	21.3

Table 18: Structure of the eigenstates of $H^{(0)}_c$, in terms of the $\tilde{S}\tilde{D}$-bases. The subscripts a, b and c for the states represent the sequence in energy of the states (see the text).

state	$\|J^P_S(\tilde{S}^2)\rangle$	$\|J^P_S(\tilde{S}\tilde{D})\rangle$	$\|J^P_S(\tilde{D}^2)\rangle$	$\|J^P_M(\tilde{S}\tilde{D})\rangle$
0^+_a	0.794		0.608	
0^+_b	−0.608		0.794	
2^+_a		0.900	−0.436	−0.008
2^+_b		0.025	0.034	0.999
2^+_c		0.435	0.899	−0.041

Table 19: Amplitudes of the $|p_\alpha\rangle$ and $|q_\alpha^{(1)}\rangle$ states in the renormalized basis $|\tilde{p}_\alpha^{(1)}\rangle$, obtained in the first order DBR.

α	$\lvert p_\alpha\rangle$	$\lvert q_\alpha^{(1)}\rangle$
$0_S^+(\tilde{S}^2)$	0.939	−0.344
$0_S^+(\tilde{D}^2)$	0.936	−0.352
$1_M^+(\tilde{D}^2)$	0.930	−0.367
$2_S^+(\tilde{S}\tilde{D})$	0.936	−0.352
$2_S^+(\tilde{D}^2)$	0.921	−0.390
$2_M^+(\tilde{S}\tilde{D})$	0.920	−0.393
$3_M^+(\tilde{D}^2)$	0.916	−0.401
$4_S^+(\tilde{D}^2)$	0.914	−0.406

Table 20: Amplitudes of the $|p_\alpha\rangle$, $|q_\alpha^{(1)}\rangle$ and $|q_\alpha^{(2)}\rangle$ states in the renormalized basis $|\tilde{p}_\alpha^{(2)}\rangle$, obtained in the second order DBR.

α	$\lvert p_\alpha\rangle$	$\lvert q_\alpha^{(1)}\rangle$	$\lvert q_\alpha^{(2)}\rangle$
$0_S^+(\tilde{S}^2)$	0.911	−0.386	0.145
$0_S^+(\tilde{D}^2)$	0.897	−0.405	0.174
$1_M^+(\tilde{D}^2)$	0.881	−0.428	0.202
$2_S^+(\tilde{S}\tilde{D})$	0.901	−0.401	0.164
$2_S^+(\tilde{D}^2)$	0.850	−0.466	0.247
$2_M^+(\tilde{S}\tilde{D})$	0.850	−0.466	0.244
$3_M^+(\tilde{D}^2)$	0.833	−0.483	0.271
$4_S^+(\tilde{D}^2)$	0.819	−0.496	0.288

Table 21: $\tilde{S}\tilde{D}$-structure of the eigenstates of $H_c^{(1)}$.

state	$\lvert J_S^P(\tilde{S}^2)\rangle$	$\lvert J_S^P(\tilde{S}\tilde{D})\rangle$	$\lvert J_S^P(\tilde{D}^2)\rangle$	$\lvert J_M^P(\tilde{S}\tilde{D})\rangle$
0_a^+	0.815		0.580	
0_b^+	−0.580		0.815	
2_a^+		0.905	−0.425	0.009
2_b^+		0.004	0.029	1.000
2_c^+		0.425	0.905	−0.028

Table 22: $\tilde{S}\tilde{D}$-structure of the eigenstates of $H_c^{(2)}$.

state	$\lvert J_S^P(\tilde{S}^2)\rangle$	$\lvert J_S^P(\tilde{S}\tilde{D})\rangle$	$\lvert J_S^P(\tilde{D}^2)\rangle$	$\lvert J_M^P(\tilde{S}\tilde{D})\rangle$
0_a^+	0.821		0.571	
0_b^+	−0.571		0.821	
2_a^+		0.906	−0.423	0.025
2_b^+		−0.037	−0.020	0.999
2_c^+		0.423	0.906	0.034

Table 23: Overlaps between the first order renormalized $\tilde{S}\tilde{D}$-states $|\tilde{p}_\alpha^{(1)}\rangle$ and the eigenstates of ^{56}Fe.

state	$\|J_S^P(\tilde{S}^2)\rangle$	$\|J_S^P(\tilde{S}\tilde{D})\rangle$	$\|J_S^P(\tilde{D}^2)\rangle$	$\|J_M^P(\tilde{S}\tilde{D})\rangle$	$\|J_M^P(\tilde{D}^2)\rangle$	$\tilde{S}\tilde{D}$-prob.
0_1^+	65.5 %		32.5 %			98.1 %
0_2^+	0.0 %		0.3 %			0.4 %
1_1^+					0.0 %	0.0 %
1_2^+					21.4 %	21.4 %
1_3^+					56.0 %	56.0 %
2_1^+		77.0 %	16.6 %	0.0 %		93.6 %
2_2^+		0.1 %	1.5 %	40.4 %		42.0 %
2_3^+		1.3 %	1.8 %	0.3 %		3.4 %
2_4^+		0.0 %	1.3 %	20.4 %		21.7 %
2_5^+		0.4 %	6.2 %	4.6 %		11.1 %
2_6^+		0.1 %	0.1 %	0.2 %		0.4 %
3_1^+					12.4 %	12.4 %
3_2^+					0.1 %	0.1 %
4_1^+			55.2 %			55.2 %
4_2^+			0.4 %			0.4 %

Table 24: Overlaps between the second order renormalized $\tilde{S}\tilde{D}$-states $|\tilde{p}_\alpha^{(2)}\rangle$ and the eigenstates of ^{56}Fe.

state	$\|J_S^P(\tilde{S}^2)\rangle$	$\|J_S^P(\tilde{S}\tilde{D})\rangle$	$\|J_S^P(\tilde{D}^2)\rangle$	$\|J_M^P(\tilde{S}\tilde{D})\rangle$	$\|J_M^P(\tilde{D}^2)\rangle$	$\tilde{S}\tilde{D}$-prob.
0_1^+	66.3 %		32.8 %			99.1 %
0_2^+	0.0 %		0.3 %			0.3 %
1_1^+					0.0 %	0.0 %
1_2^+					24.1 %	24.1 %
1_3^+					62.8 %	62.8 %
2_1^+		80.4 %	17.2 %	0.0 %		97.6 %
2_2^+		0.3 %	2.4 %	50.3 %		53.1 %
2_3^+		1.5 %	3.4 %	0.3 %		5.2 %
2_4^+		0.0 %	1.7 %	23.7 %		25.4 %
2_5^+		0.7 %	8.4 %	5.2 %		14.4 %
2_6^+		0.1 %	0.1 %	0.2 %		0.3 %
3_1^+					17.5 %	17.5 %
3_2^+					0.1 %	0.1 %
4_1^+			73.2 %			73.2 %
4_2^+			0.5 %			0.5 %

Table 25: Parameters of the boson hamiltonian. The column labelled 'unren.' displays the parameters obtained from $H_c^{(0)}$, while the column labelled 'ren.(1)' and 'ren.(2)' does those from $H_c^{(1)}$ and $H_c^{(2)}$, respectively.

		unren.	ren.(1)	ren.(2)
ϵ_{d_π}	[MeV]	1.55	1.31	1.16
ϵ_{d_ν}	[MeV]	1.56	1.39	1.22
κ	[MeV]	1.28	1.08	0.98
χ_π		−1.05	−1.15	−1.22
χ_ν		−1.14	−1.19	−1.11
c_0'	[MeV]	−0.02	0.45	0.55
c_2'	[MeV]	−0.02	0.22	0.24
c_4'	[MeV]	−0.19	−0.18	−0.48
ξ_1	[MeV]	0.04	0.42	0.51
ξ_2	[MeV]	−0.11	−0.06	−0.16
ξ_3	[MeV]	−0.06	0.08	0.05

Table 26: Comparison of electromagnetic properties between with and without renormalization in the eigenstates of H_{PP}. The single particle parameters are the same as adopted in the shell model calculation (j-independent values). The corresponding shell model values are also displayed.

		i	f	unren.	ren.(1)	ren.(2)	SM
$B(E2)$	$[e^2fm^4]$	2_a^+	0_a^+	174.1	194.2	198.4	213.1
$B(E2)$	$[e^2fm^4]$	2_b^+	0_a^+	1.1	0.9	0.1	20.6
$B(E2)$	$[e^2fm^4]$	4^+	2_a^+	161.5	218.4	234.7	291.6
Q	$[efm^2]$	2_a^+	2_a^+	−26.6	−28.0	−28.3	−28.8
μ	$[\mu_N]$	2_a^+	2_a^+	1.11	1.11	1.22	1.17
$B(M1)$	$[\mu_N^2]$	2_b^+	2_a^+	0.39	0.39	0.40	0.41
$B(M1)$	$[\mu_N^2]$	1^+	0_a^+	0.25	0.21	0.18	0.13

Table 27: Probabilities of $|2^+_{MSR}\rangle$ and $|1^+_{MSR}\rangle$ components in eigenfunctions of ^{54}Cr.

state	Ex[MeV]	$\|2^+_{MSR}\rangle$ [%]
2_1^+	0.911	0.0
2_2^+	2.787	0.2
2_3^+	3.040	25.6
2_4^+	3.632	17.1
2_5^+	3.840	4.1
state	Ex[MeV]	$\|1^+_{MSR}\rangle$ [%]
1_1^+	3.553	4.2
1_2^+	3.707	0.2
1_3^+	3.955	32.0

Table 28: Probabilities of $|2^+_{MSR}\rangle$ and $|1^+_{MSR}\rangle$ components in eigenfunctions of ^{52}Ti.

state	Ex[MeV]	$\|2^+_{MSR}\rangle$ [%]
2_1^+	1.135	0.0
2_2^+	2.152	28.2
2_3^+	2.495	14.0
2_4^+	3.504	17.7
2_5^+	3.964	0.1
state	Ex[MeV]	$\|1^+_{MSR}\rangle$ [%]
1_1^+	3.127	5.1
1_2^+	3.955	0.2
1_3^+	4.124	27.6

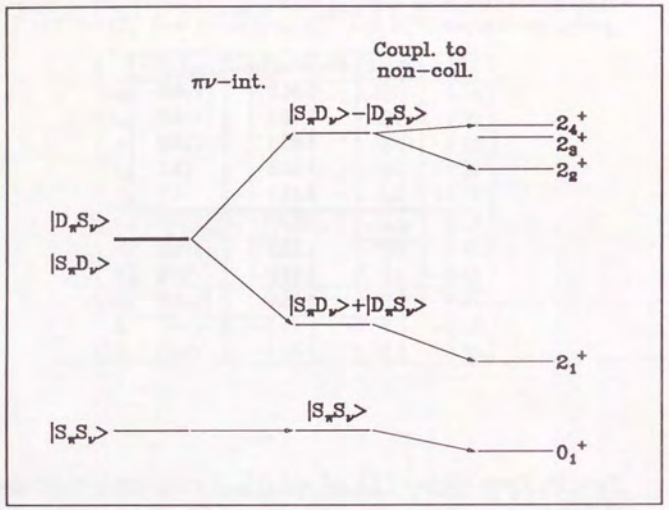

Fig.1: Energy levels in $N_\pi = N_\nu = 1$ system are illustrated. The expected levels in the $U(5)$-limit of the IBM-2 without the proton-neutron interaction are displayed in the left. The levels after the onset of the proton-neutron interaction are displayed in the middle. In the right we show some levels obtained by the shell model calculation in ^{56}Fe.

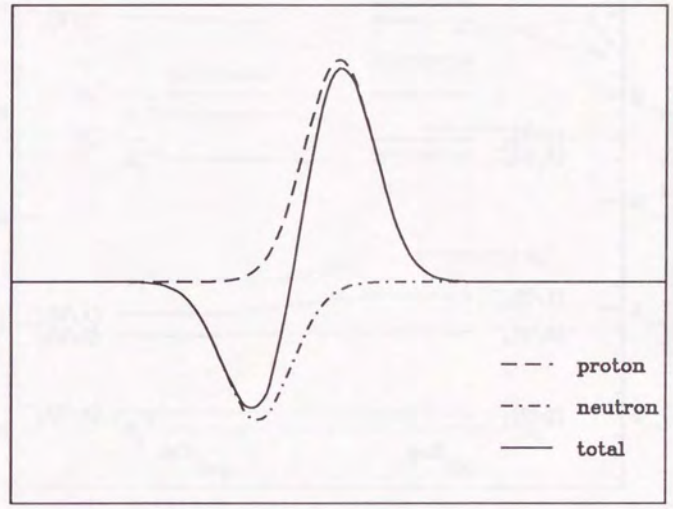

Fig.2: Expected transition densities for mixed-symmetry 2^+ state are schematically illustrated. The dashed line shows the proton transition density with the quadrupole collectivity, the dot-dashed line the neutron one, and the solid line their sum. It is presumed that the displacement between the proton peak and the neutron one is large enough for a node to exist in the total transition density.

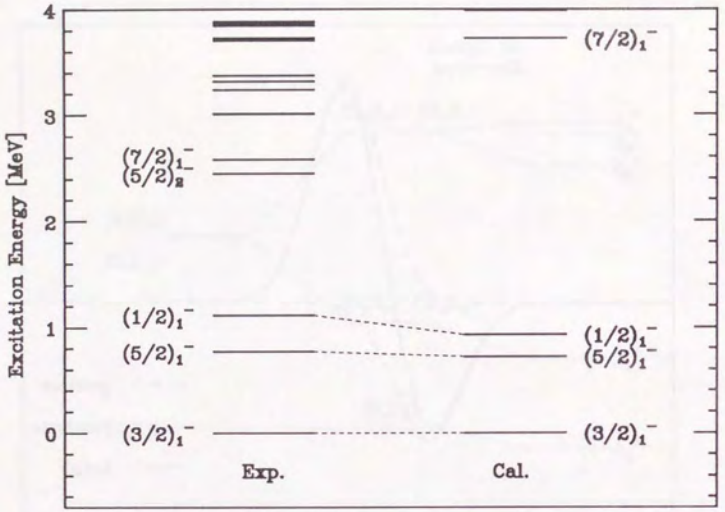

Fig.3: Experimental and calculated energy levels of ^{57}Ni. The experimental data are taken from Ref.[50]. The calculated energy levels are obtained from the shell model calculation with the Kuo-Brown hamiltonian, in the $k \leq 2$ configuration space defined in Eq.(4.1).

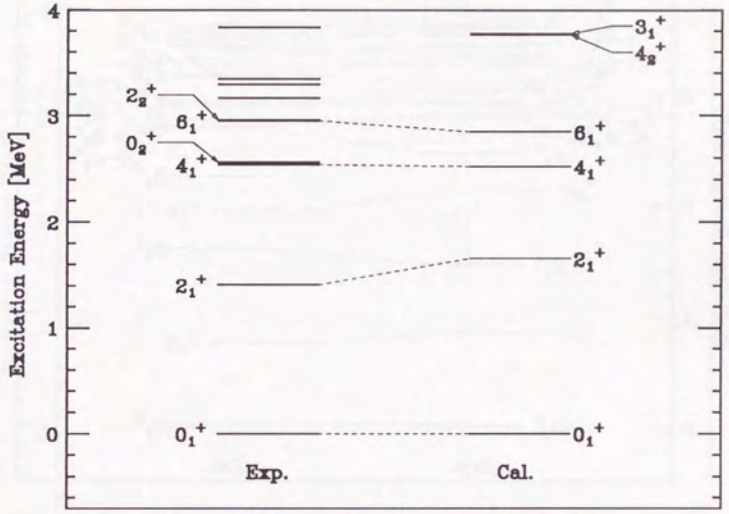

Fig.4: Experimental and calculated energy levels of ^{54}Fe. The experimental data are taken from Ref.[51].

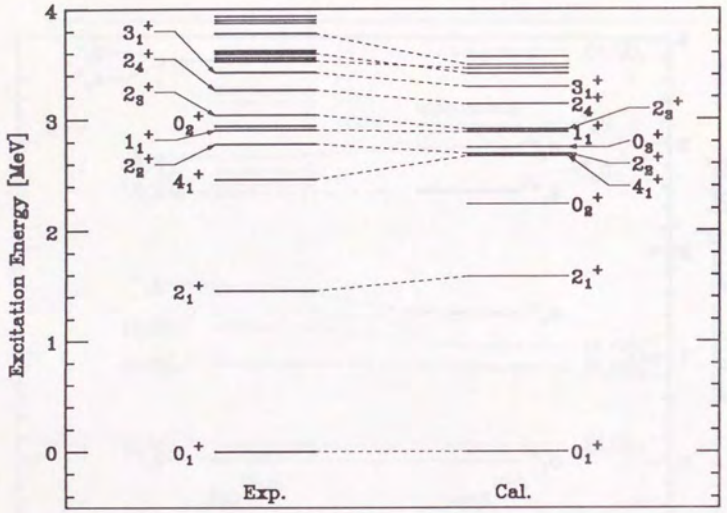

Fig.5: Experimental and calculated energy levels of ^{58}Ni. The experimental data are taken from Ref.[52].

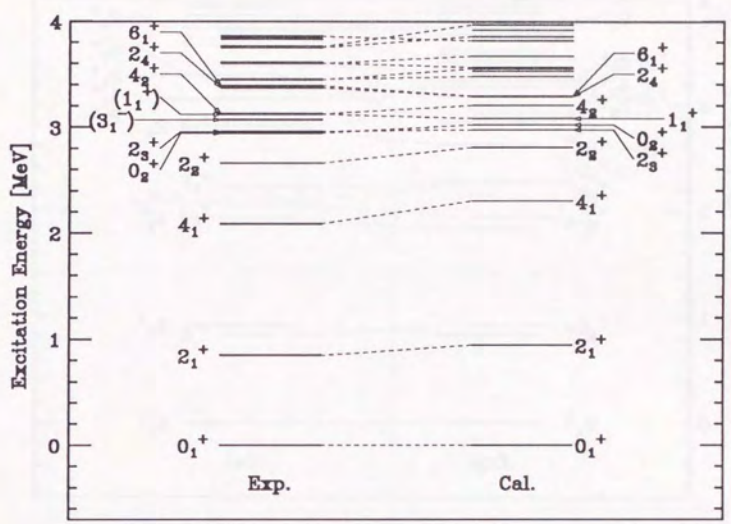

Fig.6: Experimental and calculated energy levels of ^{56}Fe. The experimental data are taken from Ref.[26].

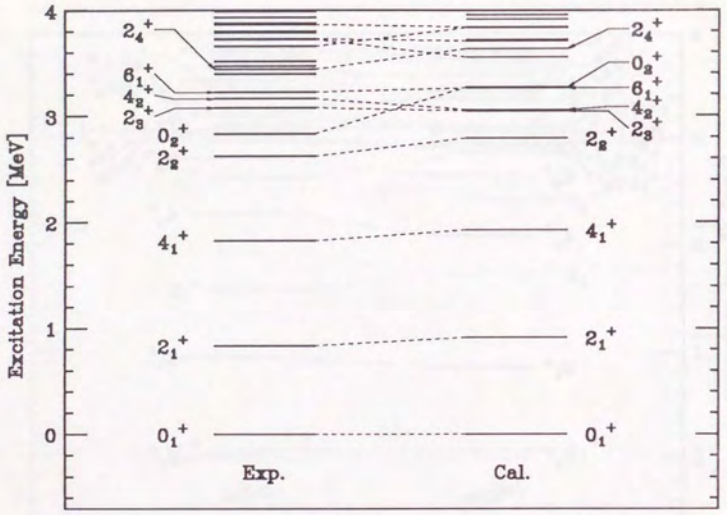

Fig.7: Experimental and calculated energy levels of ^{54}Cr. The experimental data are taken from Ref.[51].

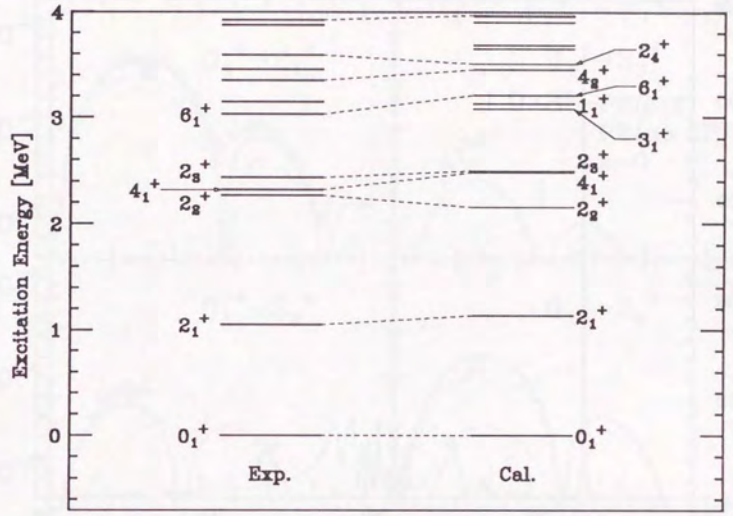

Fig.8: Experimental and calculated energy levels of ^{52}Ti. The experimental data are taken from Ref.[53].

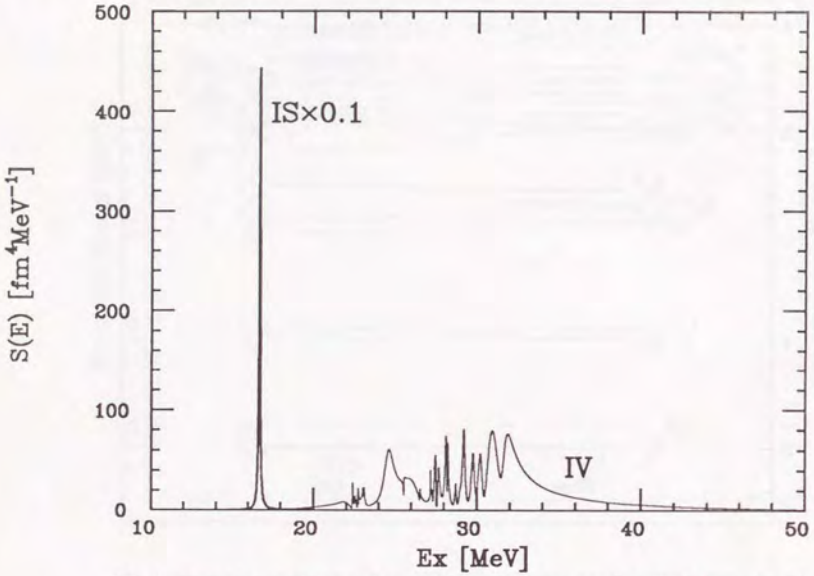

Fig.9: Isoscalar and isovector quadrupole response function from the ^{56}Ni closed core, obtained from the HF+RPA calculation with the SGII Skyrme interaction.

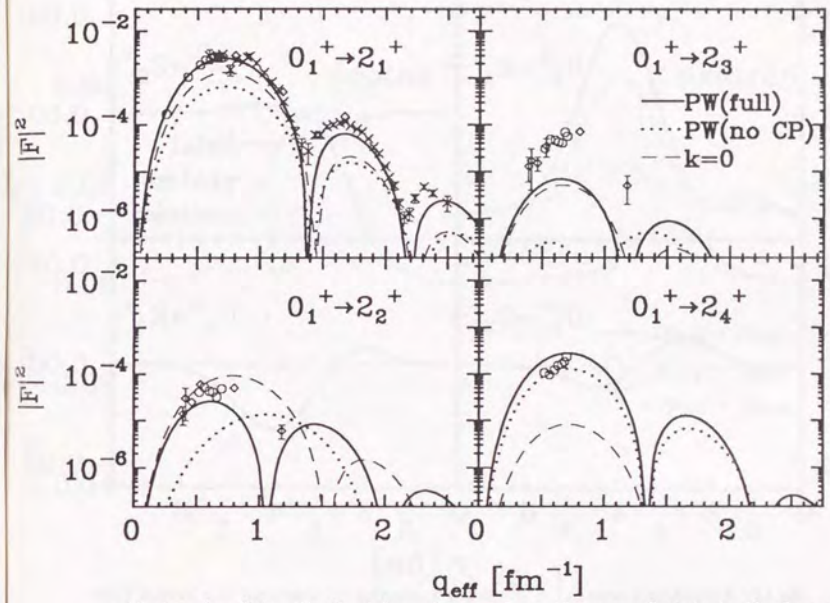

Fig.10: (e, e') longitudinal form factors from the ground state to the lowest four 2^+ states of ^{56}Fe. The solid lines show the shell model results with the core polarization effect evaluated by the HF+RPA. Those without core polarization are shown by dotted lines. The form factors obtained from the shell model calculation in the $k = 0$ space with the Horie-Ogawa interaction are also displayed by the thin dashed lines. Those include the core polarization effect in the same manner. The circles, crosses and diamonds exhibit the experimental data taken from Refs.[64], [65] and [31], respectively. The transverse mode is not separated in the experiment.

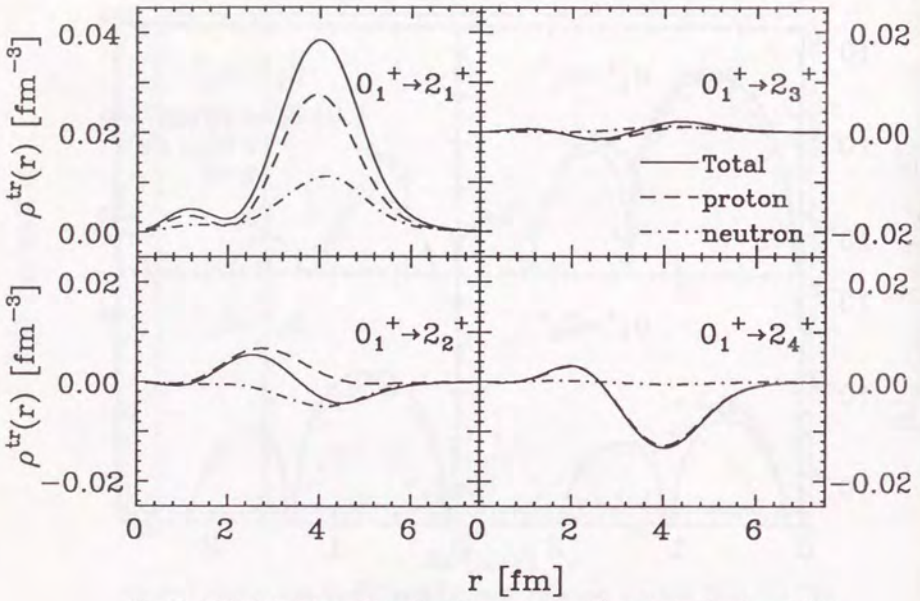

Fig.11: Calculated transition densities from the 0_1^+ state to the lowest four 2^+ states in ^{56}Fe. The dashed lines show the proton transition densities, the dot-dashed lines the neutron ones, and the solid lines the total transition densities.

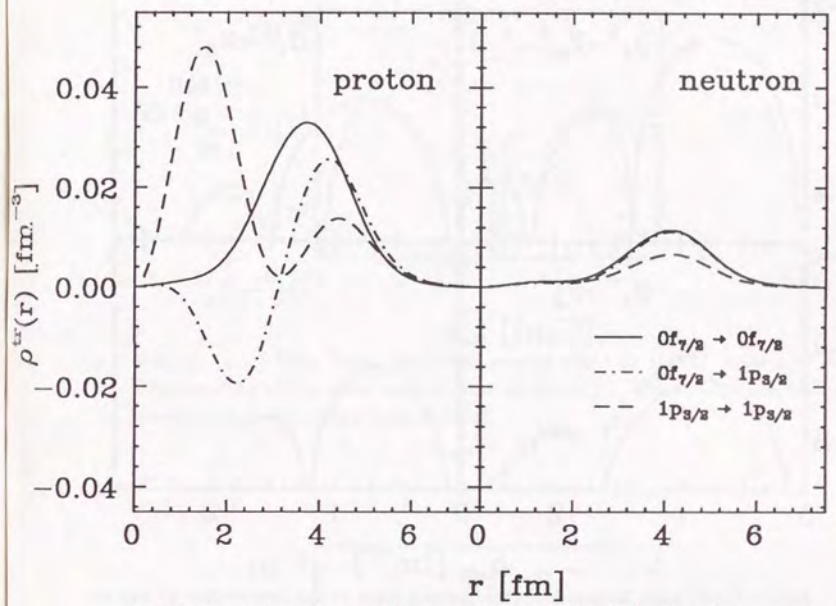

Fig.12: Typical single particle transition densities including the core polarization effect. Those with respect to the proton orbits are shown in the left box, while those with respect to the neutron orbits in the right. They are calculated by replacing the initial and final states by the single particle states in Eq.(4.14). The solid line displays the transition within the $0f_{7/2}$ orbit, the dashed one that within the $1p_{3/2}$ orbit, and the dot-dashed line the transition from the $0f_{7/2}$ orbit to the $1p_{3/2}$ orbit.

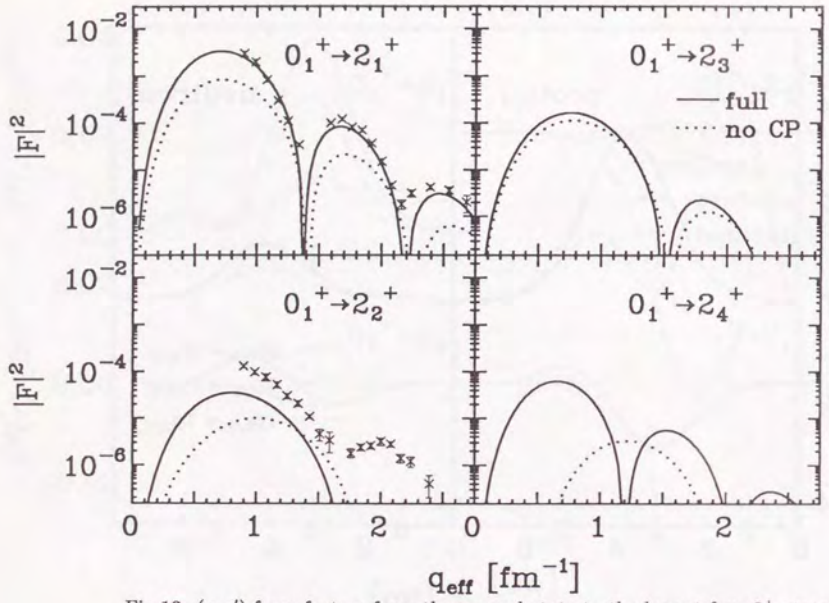

Fig.13: (e,e') form factors from the ground state to the lowest four 2^+ states of ^{54}Cr. The meaning of the lines are the same as in Fig.10. The crosses exhibit the experimental data taken from Ref.[67].

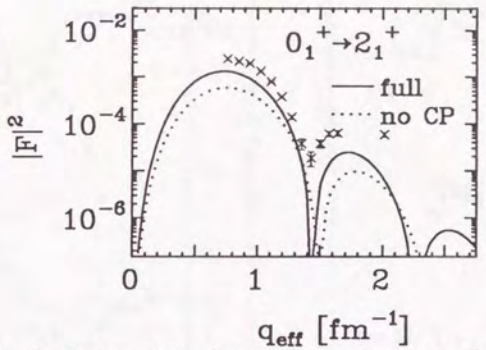

Fig.14: (e,e') form factor from the ground state to the 2_1^+ state of ^{54}Fe. The meaning of the lines are the same as in Fig.10. The crosses exhibit the experimental data taken from Ref.[68].

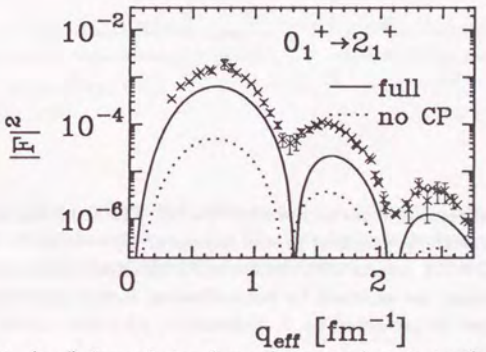

Fig.15: (e,e') form factor from the ground state to the 2_1^+ state of ^{58}Ni. The meaning of the lines are the same as in Fig.10. The crosses exhibit the experimental data taken from Ref.[69].

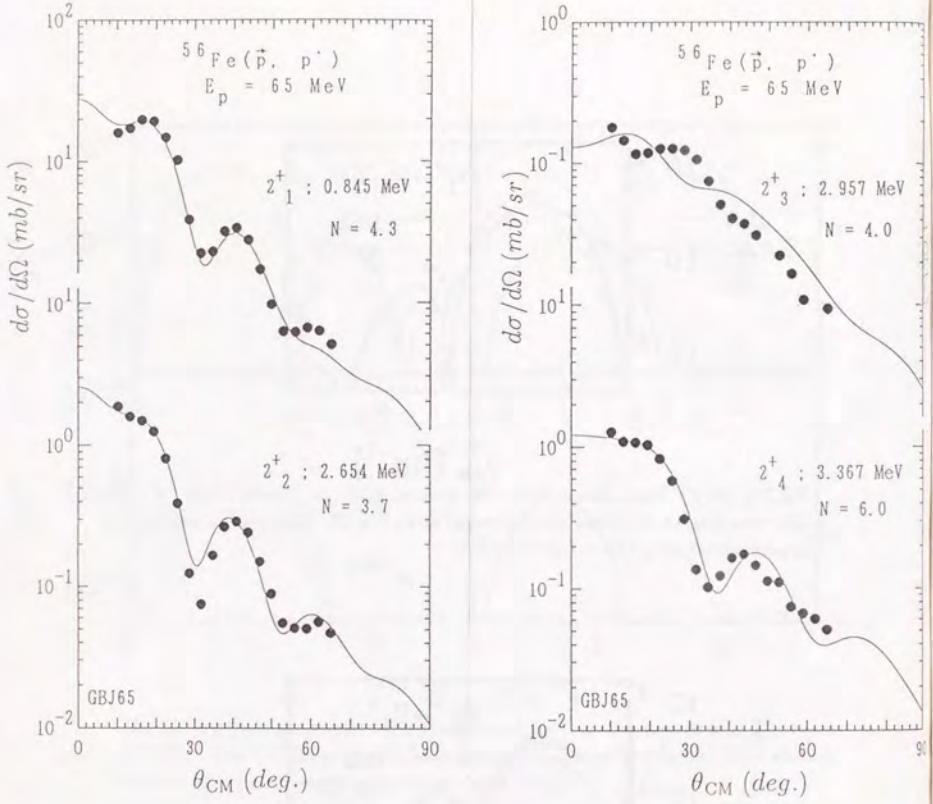

Fig.16: $(\vec{p},p')$ differential cross sections in ^{56}Fe[73]. The dots display the experimental data with the incident proton energy of $E_p = 65$MeV. The solid lines show the DWBA results with the Bonn-Jülich effective interaction[70]. The absolute values are adjusted by normalization factors exhibited in the figure. This figure is presented by J. Takamatsu, who also carried out the DWBA calculation.

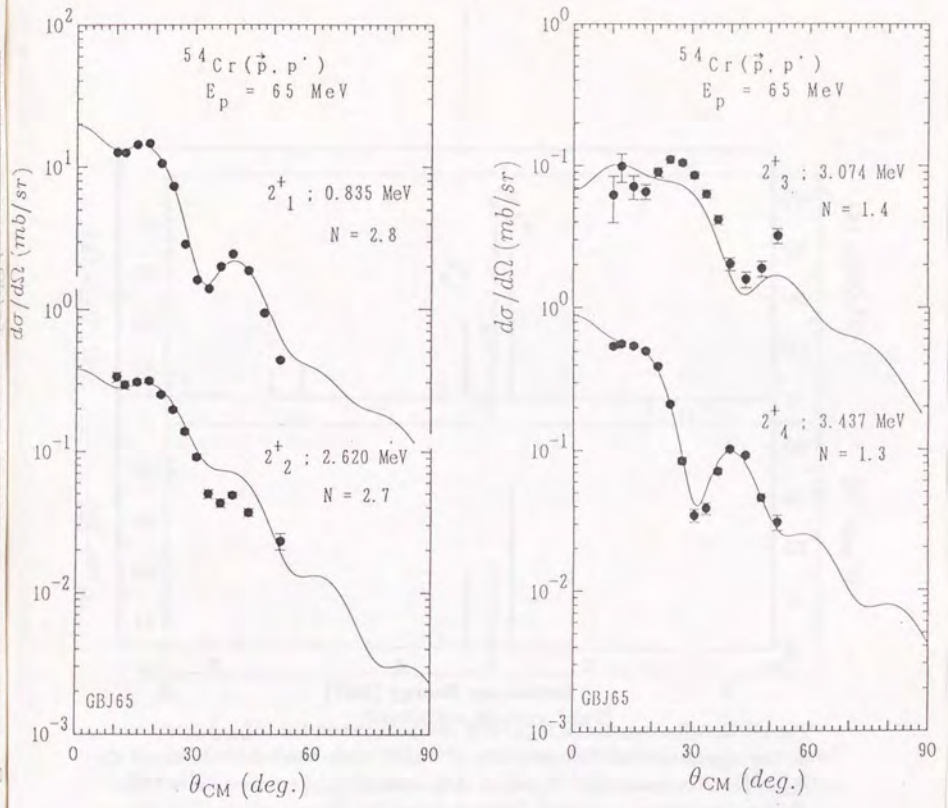

Fig.17: $(\vec{p},p')$ differential cross sections in ^{54}Cr[73]. The meaning of dots and lines are the same as in Fig.16. This figure is presented by J. Takamatsu, who also carried out the DWBA calculation.

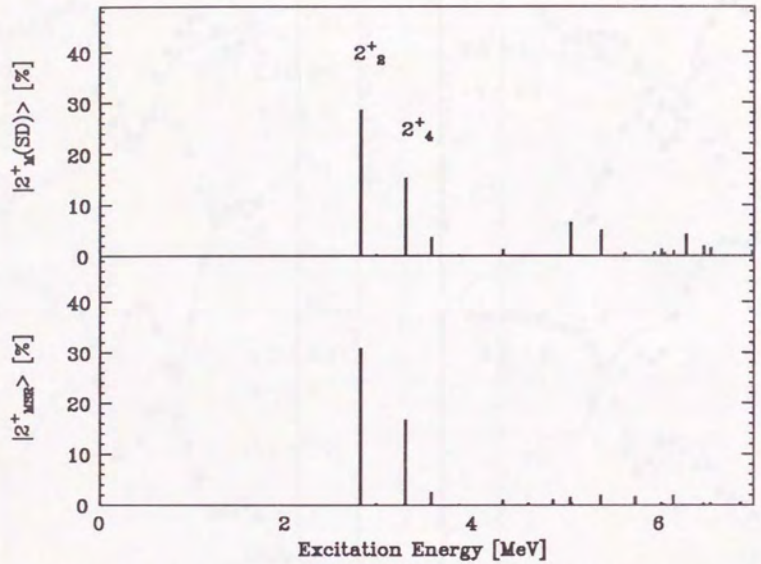

Fig.18: Distribution of the $|2^+_M(\tilde{SD})\rangle$ component and the $|2^+_{MSR}\rangle$ component, in the eigenstates of ^{56}Fe with Ex < 7MeV. The total probability of the $|2^+_M(\tilde{SD})\rangle$ component is 71%, while that of the $|2^+_{MSR}\rangle$ component is 61%.

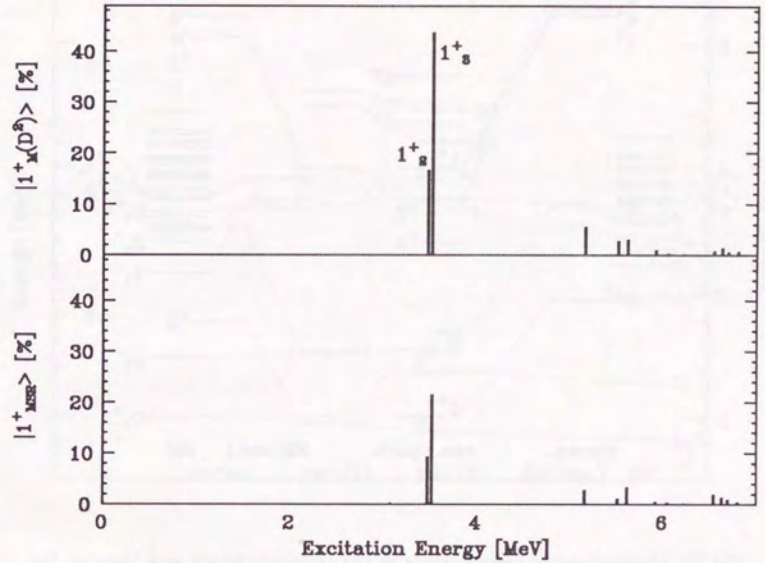

Fig.19: Distribution of the $|1^+_M(\tilde{D}^2)\rangle$ component and the $|1^+_{MSR}\rangle$ component, in the eigenstates of ^{56}Fe with Ex < 7MeV. The total probability of the $|1^+_M(\tilde{D}^2)\rangle$ component is 75%, while that of the $|1^+_{MSR}\rangle$ component is 42%.

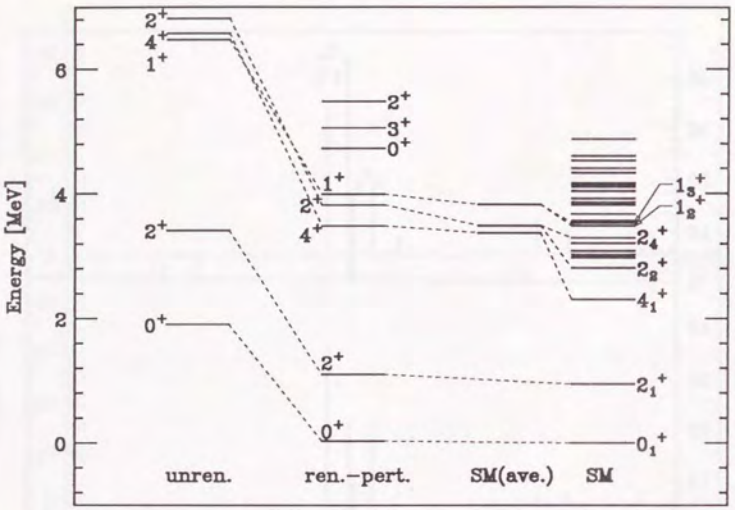

Fig.20: Comparison of energy levels in the collective space and those of the shell model eigenstates. The left most levels are the unrenormalized ones. The second left column shows the levels obtained by the perturbative renormalization with the closure approximation. The right most levels are the shell model states, while the second right ones display their $\tilde{S}\tilde{D}$-weighted averages over $0 < Ex < 6$MeV with respect to the $|4^+_S(\tilde{D}^2)\rangle$, $|2^+_M(\tilde{S}\tilde{D})\rangle$ and $|1^+_M(\tilde{D}^2)\rangle$ components.

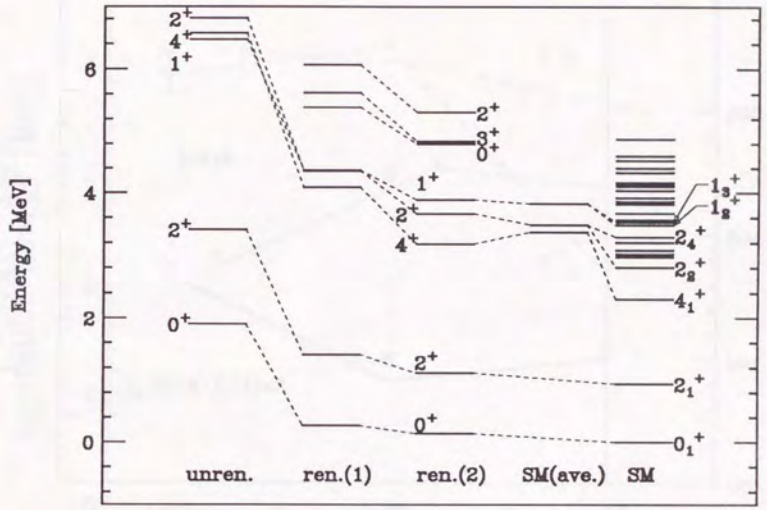

Fig.21: Comparison of energy levels in the collective space and those of the shell model eigenstates. The left most levels as well as the right two ones are the same as those shown in Fig.20. The levels 'ren.(1)' and 'ren(2)' show the first order and the second order DBR results, respectively.

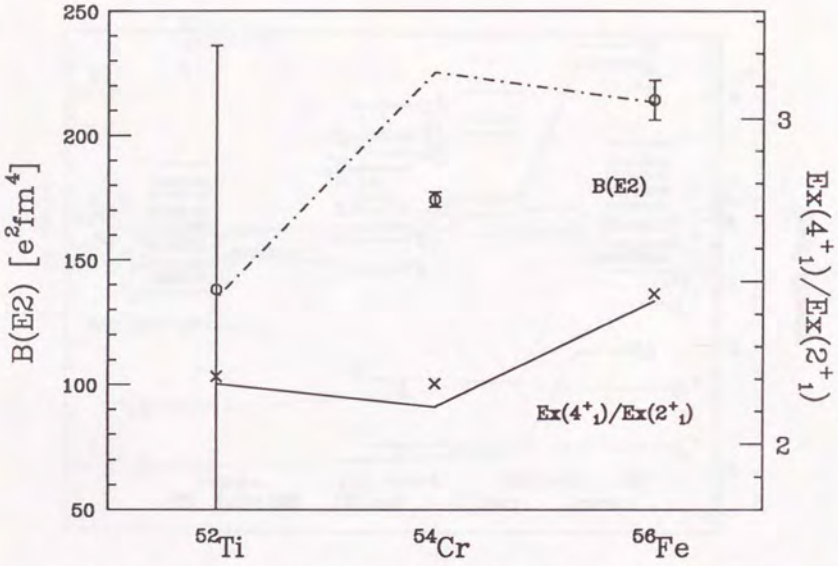

Fig.22: $B(E2;2_1^+ \to 0_1^+)$ and the ratio $Ex(4_1^+)/Ex(2_1^+)$ in the $N = 30$ isotones. The horizontal axis shows the proton number Z. The vertical axis represents the $B(E2)$ values, whose scale is shown at right, as well as the energy ratio scaled at left. The open circles with error bars display the experimental $B(E2)$ values, and the dot-dashed line does the $B(E2)$ values obtained in the present shell model calculation with the effective charges of Eq.(4.4). The cross symbols exhibit the experimental energy ratios, while the solid line the calculated ones. The experimental data are taken from Refs.[26], [51] and [53], both for the $B(E2)$ and the energies.

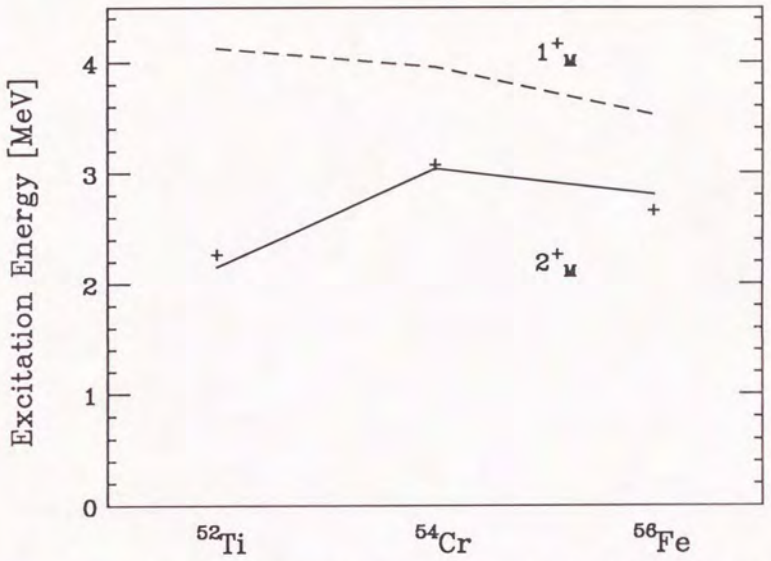

Fig.23: Excitation energies of the mixed-symmetry 2^+ and 1^+ states in the $N = 30$ isotones. Among a few states sharing the mixed-symmetry components, the state with the largest fraction of the mixed-symmetry 2^+ or 1^+ component is displayed in each nucleus. The plus symbols display the experimental energies of the 2^+ state taken from Refs.[26], [51] and [53], while the solid line the corresponding calculated ones. The dashed line shows the calculated 1^+ energies, though the corresponding states have not been observed so far.